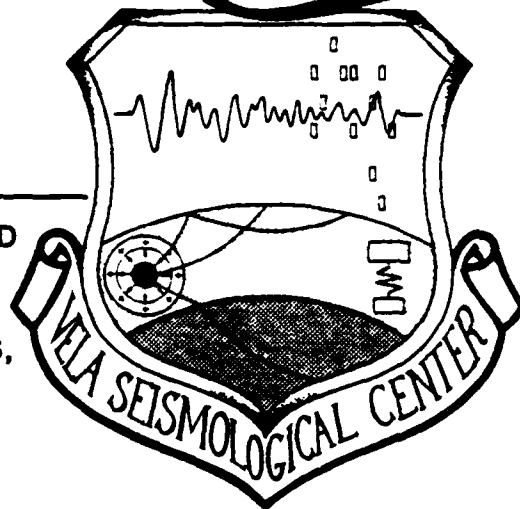


AD A110080

LEVEL

VSC-TR-81-27

REGIONAL DETECTION OF DECOUPLED  
EXPLOSIONS, YIELD ESTIMATION  
FROM SURFACE WAVES,  
TWO-DIMENSIONAL SOURCE EFFECTS,  
THREE-DIMENSIONAL EARTHQUAKE  
MODELING AND AUTOMATED  
MAGNITUDE MEASURES



T. C. Bache  
J. R. Murphy  
S. M. Day  
T. J. Bennett  
B. Shkoller

SYSTEMS, SCIENCE AND SOFTWARE  
P.O. Box 1620  
La Jolla, California 92038

July 1980

SEMIANNUAL TECHNICAL REPORT

APPROVED FOR PUBLIC RELEASE,  
DISTRIBUTION UNLIMITED

Monitored By:

VELA Seismological Center  
312 Montgomery Street  
Alexandria, VA 22314

DTIC  
ELECTE  
JAN 26 1982  
S D D

DTIC FILE COPY

01 26 8205 6

UNCLASSIFIED

SECURITY CLASSIFICATION OF THIS PAGE (When Data Entered)

REPORT DOCUMENTATION PAGE		READ INSTRUCTIONS BEFORE COMPLETING FORM
1. REPORT NUMBER VSC-TR-81-27	2. GOVT ACCESSION NO. AD-A110 080	3. RECIPIENT'S CATALOG NUMBER
4. TITLE (and Subtitle) REGIONAL DETECTION OF DECOUPLED EXPLOSIONS, YIELD ESTIMATION FROM SURFACE WAVES, TWO-DIMENSIONAL SOURCE EFFECTS, THREE-DIMENSIONAL EARTHQUAKE MODELING AND AUTOMATED MAGNITUDE MEASURES		5. TYPE OF REPORT & PERIOD COVERED 1 Semiannual Technical
7. AUTHOR(s) T. C. Bache, J. R. Murphy, S. M. Day T. J. Bennett and B. Shkoller		6. PERFORMING ORG. REPORT NUMBER 14 SSS-R-80-4594
9. PERFORMING ORGANIZATION NAME AND ADDRESS Systems, Science and Software P. O. Box 1620 La Jolla, California 92038		8. CONTRACT OR GRANT NUMBER(s) F08606-79-C-0008
11. CONTROLLING OFFICE NAME AND ADDRESS VELA Seismological Center 312 Montgomery Street Alexandria, Virginia 22314		10. PROGRAM ELEMENT, PROJECT, TASK AREA & WORK UNIT NUMBERS Program Code No. 6H189 ARPA Order No. 2551
14. MONITORING AGENCY NAME & ADDRESS (if different from Controlling Office)		12. REPORT DATE July 1980
		13. NUMBER OF PAGES 145
		15. SECURITY CLASS. (of this report) Unclassified
		15a. DECLASSIFICATION/DOWNGRADING SCHEDULE
16. DISTRIBUTION STATEMENT (of this Report)  Approved for Public Release, Distribution Unlimited.		
17. DISTRIBUTION STATEMENT (of the abstract entered in Block 20, if different from Report)		
18. SUPPLEMENTARY NOTES		
19. KEY WORDS (Continue on reverse side if necessary and identify by block number)		
20. ABSTRACT (Continue on reverse side if necessary and identify by block number) This semiannual technical report includes summaries of five separate technical reports. These are: I. "A Simulation Study of the Detectability of a 5.3 KT Decoupled Explosion at Regional Distances in the Eastern United States;" II. "Yield Estimation from Surface Wave Recordings of Underground Explosions - A Review;" III. "The Contribution of Two-Dimensional Source Effects to the Far-Field Seismic Signatures of Underground Nuclear Explosions;" IV. "Three-Dimensional Earthquake Modeling Including Nonlinear Rupture Dynamics;" V. "Automated Magnitudes <sup>m</sup> and <sub>b</sub> ." <sup>sub b</sup>		

DD FORM 1 JAN 73 1473

EDITION OF 1 NOV 65 IS OBSOLETE

UNCLASSIFIED

SECURITY CLASSIFICATION OF THIS PAGE (When Data Entered)

UNCLASSIFIED

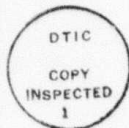
SECURITY CLASSIFICATION OF THIS PAGE(When Data Entered)

20. ABSTRACT (continued)

In Section II regional recordings of SALMON are scaled to simulate the observations of a hypothetical 5.3 KT decoupled explosion. The hypothetical event would probably not be detectable beyond 1000 km, except at quiet stations where the Lg phase would probably be detected. Results from several previous reports concerning the problem of estimating yield from single station surface wave recordings are reviewed in Section III. The main results from a much lengthier report describing a study of the seismic waves from a series of two-dimensional calculations of explosions in granite are summarized in Section IV. The fourth section is a brief summary of results from several three-dimensional finite difference calculations of earthquake faulting done on the ILLIAC computer. Spontaneous rupture is simulated with a displacement-weakening constitutive model in the presence of both uniform and heterogeneous prestress. The final section describes results from algorithms for computing automated spectral body and surface wave magnitudes that promise to give more consistent and convenient measures of signal energy than the currently used time domain magnitudes.

UNCLASSIFIED

Accession For	
NTIS GRA&I	<input checked="" type="checkbox"/>
DTIC TAB	<input type="checkbox"/>
Unannounced	<input type="checkbox"/>
Justification	
By	
Distribution/	
Availability Codes	
Dist	Avail and/or Special
A	



AFTAC Project Authorization No. VT/0712/B/PMP  
 ARPA Order No. 2551, Program Code No. 6H189  
 Effective Date of Contract: November 17, 1978  
 Contract Expiration Date: November 15, 1981  
 Amount of Contract: \$1,816,437  
 Contract No. F08606-79-C-0008  
 Principal Investigator and Phone No.  
 Dr. J. Theodore Cherry, (714) 453-0060  
 Project Scientist and Phone No.  
 Mr. Brian W. Barker, (202) 325-7581

This research was supported by the Advanced Research Projects  
 Agency of the Department of Defense and was monitored by  
 AFTAC/VSC, Patrick Air Force Base, Florida 32925, under Contract No.  
 F08606-79-C-0008.

The views and conclusions contained in this document are those of  
 the authors and should not be interpreted as necessarily representing  
 the official policies, either expressed or implied, of the Advanced  
 Research Projects Agency, the Air Force Technical Applications  
 Center, or the U.S. Government.

DTIC  
 ELECTE  
 JAN 26 1982  
 S D

## TABLE OF CONTENTS

Section	Page
I INTRODUCTION AND SUMMARY . . . . .	1
1.1 INTRODUCTION . . . . .	1
1.2 SUMMARY OF SECTION II: "A SIMULATION STUDY OF THE DETECTABILITY OF A 5.3 KT DECOUPLED EXPLO- SION AT REGIONAL DISTANCES IN THE EASTERN UNITED STATES". . . . .	1
1.3 SUMMARY OF SECTION III: "YIELD ESTIMATION FROM SURFACE WAVE RECORDINGS OF UNDERGROUND EXPLO- SIONS -- A REVIEW". . . . .	1
1.4 SUMMARY OF SECTION IV: "THE CONTRIBUTION OF TWO- DIMENSIONAL SOURCE EFFECTS TO THE FAR-FIELD SEIS- MIC SIGNATURES OF UNDERGROUND NUCLEAR EXPLOSIONS". . . . .	2
1.5 SUMMARY OF SECTION V: "THREE-DIMENSIONAL EARTH- QUAKE MODELING INCLUDING NONLINEAR RUPTURE DYNAMICS". . . . .	3
1.6 SUMMARY OF SECTION VI: "AUTOMATED MAGNITUDES, $\hat{m}_b$ AND $M_s$ ". . . . .	3
II A SIMULATION STUDY OF THE DETECTABILITY OF A 5.3 KT DECOUPLED EXPLOSION AT REGIONAL DISTANCES IN EASTERN UNITED STATES. . . . .	5
III YIELD ESTIMATION FROM SURFACE WAVE RECORDINGS OF UNDERGROUND EXPLOSIONS -- A REVIEW . . . . .	41
3.1 INTRODUCTION. . . . .	41
3.2 EXPERIMENTAL DETERMINATION OF THE DEPENDENCE OF RAYLEIGH WAVE AMPLITUDE ON PROPERTIES OF THE SOURCE MATERIAL . . . . .	42
3.3 EXPLOSION RDP AMPLITUDES FROM RAYLEIGH WAVES. . . . .	48
3.3.1 <u>Introduction</u> . . . . .	48
3.3.2 <u>Path Models Compatible with Surface Wave Observations</u> . . . . .	48
3.3.3 <u>Surface Wave Dependence on Source Material Properties</u> . . . . .	51

# TABLE OF CONTENTS (cont'd)

Section	Page
3.3.4 <u>Inversion for the RDP Source Amplitudes</u> . . . . .	51
3.4 HIGHER ORDER SOURCE EFFECTS. . . . .	55
3.5 SURFACE WAVE RADIATION PATTERNS. . . . .	56
3.5.1 <u>Introduction</u> . . . . .	56
3.5.2 <u>Analysis of Regional Motions from MIGHTY EPIC and DIABLO HAWK</u> . . . . .	57
3.5.3 <u>Discussion of the Radiation Pattern Data</u> .	64
3.6 CONCLUSIONS . . . . .	65
IV. THE CONTRIBUTION OF TWO-DIMENSIONAL SOURCE EFFECTS TO THE FAR-FIELD SEISMIC SIGNATURES OF UNDERGROUND NUCLEAR EXPLOSIONS. . . . .	69
4.1 INTRODUCTION . . . . .	69
4.2 BACKGROUND . . . . .	70
4.3 AXISYMMETRIC CALCULATIONS OF NUCLEAR EXPLOSIONS. .	71
4.4 OUTLINE OF THE ANALYSIS. . . . .	72
4.5 CONCLUSIONS. . . . .	74
V. THREE-DIMENSIONAL EARTHQUAKE MODELING INCLUDING NONLINEAR RUPTURE DYNAMICS. . . . .	79
VI. AUTOMATED MAGNITUDES, $\hat{m}_b$ AND $\hat{m}_s$ . . . . .	86
6.1 INTRODUCTION . . . . .	86
6.2 THE $\hat{m}_b$ ALGORITHM . . . . .	88
6.3 $\hat{m}_b$ TEST CALCULATIONS . . . . .	94
6.4 $\hat{m}_b$ FOR RKN RECORDINGS OF EURASIAN EVENTS. . . . .	113
6.5 THE $\hat{m}_s$ ALGORITHM . . . . .	126
6.6 $\hat{m}_s$ TEST CALCULATIONS . . . . .	129
6.7 CONCLUSIONS. . . . .	129
REFERENCES. . . . .	137

## LIST OF FIGURES

Figure	Page
2.1 Map locations of regional SALMON stations used in the decoupling simulation . . . . .	6
2.2 Theoretical decoupling factor for 5.3 KT in a 39 m radius cavity in SALMON salt . . . . .	7
2.3 Comparison of observed SALMON and simulated decoupled vertical component seismograms, station EUAL . . . . .	9
2.4 Comparison of observed SALMON and simulated decoupled vertical component seismograms, station CPO. . . . .	10
2.5 Comparison of observed SALMON and simulated decoupled vertical component seismograms, station BLWV . . . . .	12
2.6 Comparison of observed SALMON and simulated decoupled vertical component seismograms, station WFMN . . . . .	14
2.7 Comparison of P wave and noise spectral amplitude levels, station EUAL . . . . .	18
2.8 Comparison of $L_g$ and noise spectral amplitude levels, station EUAL . . . . .	19
2.9 Comparison of P wave and noise spectral amplitude levels, station CPO. . . . .	20
2.10 Comparison of $L_g$ and noise spectral amplitude levels, station CPO . . . . .	21
2.11 Comparison of P wave and noise spectral amplitude levels, station BLWV . . . . .	22
2.12 Comparison of $L_g$ and noise spectral amplitude levels, station BLWV . . . . .	23
2.13 Comparison of P wave and noise spectral amplitude levels, station WFMN . . . . .	24
2.14 Comparison of $L_g$ and noise spectral amplitude levels, station WFMN . . . . .	25
2.15 Comparison of uncorrected and corrected instrument response for stations CPO and EUAL. . . . .	26

# LIST OF FIGURES (cont'd)

Figures		Page
2.16	Comparison of uncorrected and corrected instrument response for station BLWV . . . . .	27
2.17	Comparison of uncorrected and corrected instrument response for station WFMN. . . . .	28
2.18	Comparison of instrument-corrected SALMON and simulated decoupled vertical component seismograms, station EUAL. . . . .	29
2.19	Comparison of instrument-corrected SALMON and simulated decoupled vertical component seismograms, station CPO . . . . .	30
2.20	Comparison of instrument-corrected SALMON and simulated decoupled vertical component seismograms, station BLWV . . . . .	32
2.21	Comparison of instrument-corrected SALMON and simulated decoupled vertical component seismograms, station WFMN . . . . .	34
2.22	Comparison of theoretical and instrument-corrected observed P wave spectra, station CPO . . . . .	38
3.1	The $M_S$ values from WWSSN stations ALQ and TUC are plotted versus explosion yield . . . . .	45
3.2	The $M_S$ estimates from ALQ and TUC are compared to those from Eisenhower for eighteen common events. The standard deviation of the mean residual between these two $M_S$ measures is 0.10 $M_S$ units . . . . .	46
3.3	The mean values of $M_S$ -log W for events in a limited yield range in each of the testing areas are depicted by a bar graph. . . . .	47
3.4	Theoretical and observed seismograms are compared at ALQ (left) and TUC for events in three test areas at NTS. In each pair the observed and theoretical records start at the same time with respect to the explosion detonation and this time is indicated as $T_0$ . . . . .	50
3.5	(a) The density, shear and compressional wave velocities are plotted versus depth for the three test area at NTS. (b) The source amplification factor is shown for the three source areas studied. (c) The transmission coefficient is plotted for the six source-path combinations studied. . . . .	52

# LIST OF FIGURES (cont'd)

Figures	Page
3.6 The $\Psi_{\infty}$ values are plotted versus explosion yield for the Yucca Flat and Pahute Mesa events . . . . .	54
3.7 Comparison of theoretical LQ/LR radiation patterns to the observed data with and without path corrections . . . . .	59
3.8 Theoretical Rayleigh wave radiation patterns are compared to the DIABLO HAWK observations normalized to a range of 250 km . . . . .	60
3.9 Theoretical Love wave radiation patterns are compared to DIABLO HAWK observations normalized to 250 km . . . . .	61
3.10 The fit to the MIGHTY EPIC LQ/LR data. We assume vertical strike-slip faulting . . . . .	62
3.11 MIGHTY EPIC LR and LQ data compared to theoretical radiation patterns . . . . .	63
5.2 Stress-concentration fault models considered in this study . . . . .	81
5.3 Rupture mechanism and far-field spectra and pulse shapes for stress concentration earthquake model . . . . .	82
5.4 Peak slip velocity and rupture velocity along the x axis, for multiple stress-concentration model . . . . .	83
5.5 Rupture mechanism and far-field spectra and pulse shapes for multiple stress-concentration earthquake model . . . . .	84
5.6 Short-period P-waves from uniform stress model and stress-concentration model. The two events are plotted as triangles on an $m_b$ -versus $M_s$ diagram . . . . .	85
6.1 Bottom portion is a seismogram recorded at a station in Bluff, Alaska, from an event in the Kurils. The top half is a plot of filter center frequency versus group arrival time . . . . .	89
6.2 Calculation of $\hat{m}_b$ for a seismogram with peak synthetic/peak noise = 100. . . . .	92
6.3 Comparison of the Fourier velocity spectrum to the MARS log spectrum . . . . .	95

# LIST OF FIGURES (cont'd)

Figures		Page
6.4	Test of the $\hat{m}_b$ algorithm with a synthetic seismogram embedded in noise section 62110. . . . .	96
6.5	Test of the $\hat{m}_b$ algorithm with noise section 274110 . . .	.104
6.6	The $tg-f_c$ section for Case F of Figure 6.4 . . . . .	.112
6.7	Map of Eurasia showing locations of 8 presumed explosions for which the $\hat{m}_b$ is determined at RKON. . .	.114
6.8	$\hat{m}_b$ for presumed Soviet explosions recorded at RKON . . .	.115
6.9	$\hat{m}_b$ for earthquakes recorded at RKON . . . . .	.123
6.10	$\hat{m}_b$ for an earthquake recorded at LASA. . . . .	.125
6.11	$\hat{M}_s$ calculations for several noise samples . . . . .	.131

## LIST OF TABLES

Tables		Page
6.1	SUMMARY OF $\hat{m}_b$ TEST CALCULATIONS. . . . .	.110
6.2	SUMMARY OF $\hat{m}_b$ FOR ACTUAL EVENT RECORDINGS . . . . .	.127
6.3	SUMMARY OF $\hat{M}_s$ TEST CALCULATIONS. . . . .	.134

## I. INTRODUCTION AND SUMMARY

### 1.1 INTRODUCTION

The objective of the Systems, Science and Software research program is to extend our present understanding of the excitation of seismic waves by underground explosions and earthquakes in order to improve the United States' ability to monitor compliance with treaties limiting underground nuclear explosions. This report is for the six month period between 1 October, 1979, and 1 April, 1980, and includes five distinct technical sections. These are briefly summarized in the following subsections.

### 1.2 SUMMARY OF SECTION II: "A SIMULATION STUDY OF THE DETECTABILITY OF A 5.3 KT DECOUPLED EXPLOSION AT REGIONAL DISTANCES IN THE EASTERN UNITED STATES"

This section was written by J. R. Murphy and T. J. Bennett of the Reston Geophysics office of Systems, Science and Software. The objective is to extend the regional seismic data base for explosions in the eastern United States by theoretically scaling observed SALMON data to simulate the seismograms expected from a (hypothetical) fully decoupled 5.3 KT explosion at the SALMON site. The vertical SALMON recordings from four stations (EUAL,  $\Delta = 246$  km; CPO,  $\Delta = 623$  km; BLWV,  $\Delta = 1065$  km; WFMN,  $\Delta = 1437$  km) were convolved with an operator which is intended to represent the ratio of the source spectrum for a decoupled 5.3 KT event to the source spectrum for SALMON. Analysis of the resulting seismograms indicates that such a decoupled event would probably be detectable at the two closer stations, but not at the two stations with  $\Delta > 1000$  km. At more quiet stations, the Lg phase would probably be detected at all four stations, but the initial P wave would be difficult to detect.

### 1.3 SUMMARY OF SECTION III: "YIELD ESTIMATION FROM SURFACE WAVE RECORDINGS OF UNDERGROUND EXPLOSIONS -- A REVIEW"

In December, 1979, DARPA solicited contributions from interested scientists to a state-of-the-art assessment of seismic

yield determination. S-Cubed scientists submitted nine separate summaries:

1. Definitions of Body Wave Magnitude  
T. C. Bache
2. Definition of Surface Wave Magnitude  
T. C. Bache
3. Source Theory and Observation for Surface Waves  
T. C. Bache
4. Tectonic Generation of Surface Waves  
T. C. Bache
5. Effects of Source Region Properties on Surface  
Wave Generation  
T. C. Bache
6. Effects of Attenuation on Surface Waves  
T. C. Bache
7. Body Wave Coupling Theory  
J. R. Murphy
8. Experimental Data on Body Wave Coupling  
J. R. Murphy
9. Source Coupling for Body Waves and Surface Waves  
J. T. Cherry

In most cases these summaries are very useful as concise reviews of past work that has appeared in many reports. Those numbered 3, 4, 5 and 6 are concerned with various aspects of the problem of estimating yield from single station recordings of surface waves. The material in these four summaries has been condensed still further into a single review which appears as Section III of this report.

#### 1.4 SUMMARY OF SECTION IV: "THE CONTRIBUTION OF TWO-DIMENSIONAL SOURCE EFFECTS TO THE FAR-FIELD SEISMIC SIGNATURES OF UNDERGROUND NUCLEAR EXPLOSIONS"

In this section we reprint the "Abstract" and "Introduction and Summary" from a report of the same title (Bache, et al., 1980) just submitted to VSC/ARPA.

## 1.5 SUMMARY OF SECTION V: "THREE-DIMENSIONAL EARTHQUAKE MODELING INCLUDING NONLINEAR RUPTURE DYNAMICS"

Presented in this section is a summary of the earthquake modeling work done by Steven M. Day and presented to the AFOSR Program Review in May, 1980.

## 1.6 SUMMARY OF SECTION VI: "AUTOMATED MAGNITUDES, $\hat{m}_b$ AND $\hat{M}_s$ "

This section was written by T. C. Bache and describes algorithms for computing automated spectral body and surface wave magnitudes. These magnitudes are a byproduct of MARS signal processing, which has previously been implemented for signal detection and earthquake/explosion discrimination. They promise to give more consistent and convenient measures of signal energy than currently used time domain magnitudes.

An earlier version of the  $\hat{m}_b$  algorithm was described and tested as an indicator of seismic yield by Bache (1979). The current algorithm essentially follows the recommendations of Masso *et al.* (1979) and Savino, *et al.* (1980), including corrections to account for the presence of seismic noise. The  $\hat{M}_s$  algorithm is much the same, except that the dispersion character of the surface wave signal of interest must be pre-specified so the time series can be processed to make a matching arrival appear to be undispersed.

The  $\hat{m}_b$  and  $\hat{M}_s$  algorithms are tested by applying them to seismograms constructed by adding various levels of seismic noise to a signal of known magnitude. Consistent magnitude estimates are obtained, even when the signal is nearly obscured by the superimposed noise.

Also presented in Section VI are the  $\hat{m}_b$  results for a series of RKON recordings of Eurasian earthquakes and explosions from the AI data set. The magnitude algorithms are ready for application to a much larger data base.

THIS PAGE LEFT BLANK

## II. A SIMULATION STUDY OF THE DETECTABILITY OF A 5.3 KT DECOUPLED EXPLOSION AT REGIONAL DISTANCES IN EASTERN UNITED STATES

We have recently completed a preliminary analysis in which we theoretically scaled several SALMON short-period seismograms observed at regional distances in the eastern United States to produce estimates of the corresponding seismograms which would be expected at these stations from a fully decoupled 5.3 KT explosion at the SALMON shot point. The primary purpose of this investigation has been to extend the existing regional seismic data base for explosions in the eastern United States to support on-going theoretical investigations of regional phase generation, propagation and detection.

Four eastern United States stations were selected for analysis: Eutaw, Alabama (EUAL,  $\Delta = 246$  km), Cumberland Plateau Observatory, Tennessee (CPO,  $\Delta = 623$  km), Beckley, West Virginia (BLWV,  $\Delta = 1065$  km) and Wykoff, Minnesota (WFMN,  $\Delta = 1437$  km). The locations of these four stations are indicated by squares on Figure 2.1, which provides a map view of the North American stations which recorded the SALMON event (Jordan et al., 1966). The observed vertical component SALMON data recorded at these four stations have been theoretically scaled (Murphy, 1966) to the ground motion to be expected from a fully decoupled 5.3 KT explosion at the SALMON shotpoint. The theoretical decoupling factor (with respect to SALMON) corresponding to a simple step in pressure in a 39 m radius cavity is shown in Figure 2.2. It should be noted that the amplitude level in Figure 2.2. has been arbitrarily normalized to give a maximum decoupling factor (at 2.5 Hz) of 100. This reflects the fact that the observations from both the COWBOY and STERLING experiments indicate low frequency decoupling efficiencies which are significantly lower than those predicted theoretically. Thus, the expected magnitude of the decoupling is still not well defined and the levels shown in Figure 2.2 should be regarded as being uncertain within about a factor of two. The frequency dependence of the decoupling factor, on the other hand, depends primarily on the shape



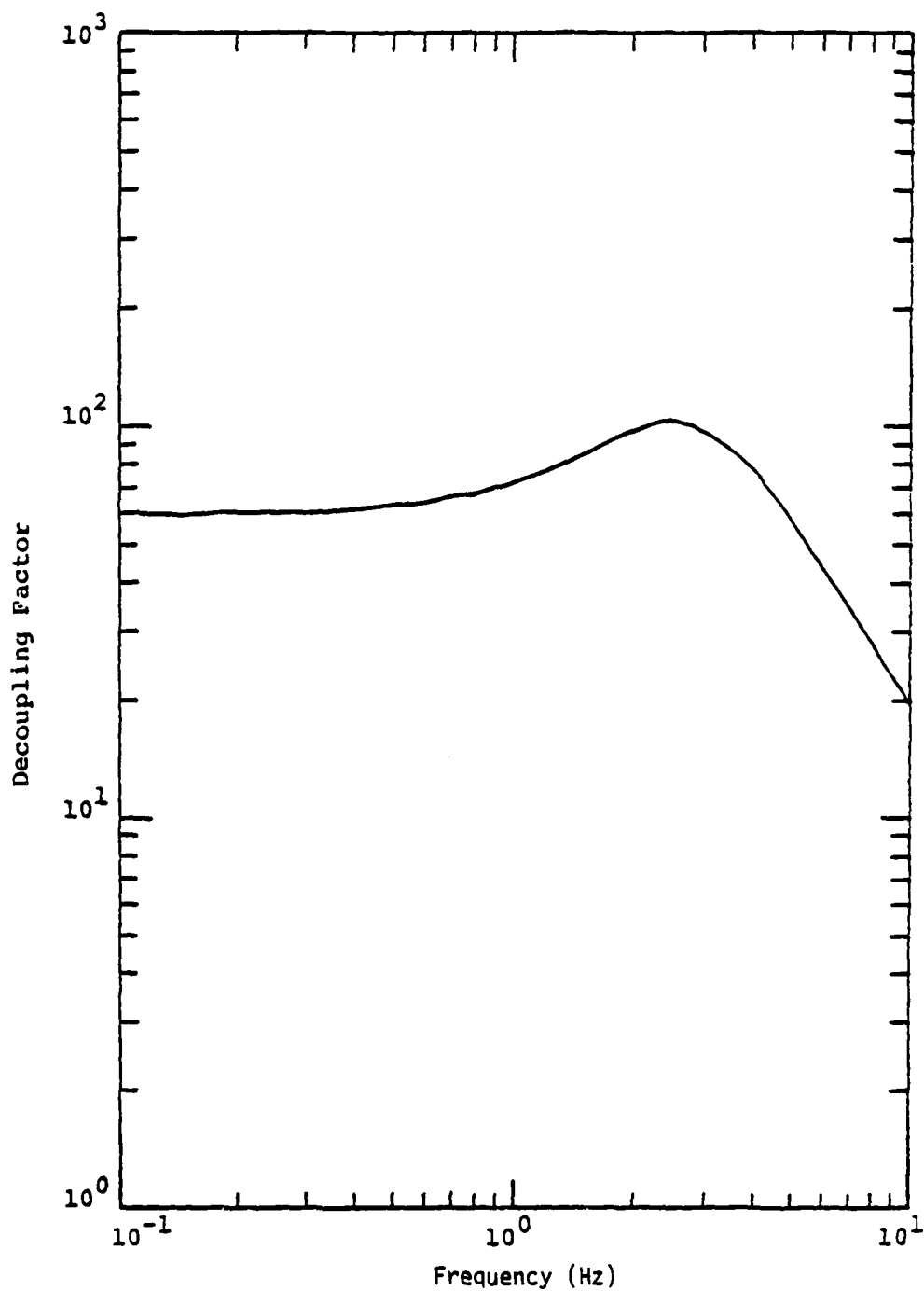


Figure 2.2. Theoretical decoupling factor for 5.3 KT in a 39 m radius cavity in SALMON salt.

of the SALMON source function for frequencies below about 10 Hz, and this seems to be reasonably well constrained by both the free-field and near-regional seismic data.

The observed SALMON vertical component seismograms recorded at the four selected stations are shown in Figures 2.3 to 2.6 (top), where they are compared with the corresponding simulated decoupled seismograms (bottom). The simulated decoupled seismograms were obtained by convolving the observed SALMON seismograms with an operator defined by the ratio of the decoupled to SALMON theoretical source functions. The traces shown to the left of the simulated decoupled seismograms correspond to samples of the noise recorded prior to SALMON at each station, amplified so that they can be compared with the estimated decoupled signal levels. This provides a basis for assessing the detectability of the hypothesized decoupled explosions at these stations under the local noise conditions prevailing at the time of the SALMON experiment. A comparison of the upper and lower traces in these figures reveals that, in each of these cases, the character of the simulated decoupled seismogram is very similar to that of the corresponding SALMON seismogram. This reflects the fact that the decoupling factor is essentially constant over the narrow passband available from the standard short-period systems used to record SALMON. It can be concluded from Figures 2.3 to 2.6 that, relative to these background noise conditions, such a decoupled explosion would probably be detectable at stations EUAL and CPO (assuming some improvement in the signal-to-noise ratio resulting from signal conditioning), but not at BLWV or WFMN. However, it must be noted that the recorded noise levels prior to SALMON (i.e., peak-to-peak values at 1 Hz of about 100  $m\mu$  at EUAL and 30  $m\mu$  at BLWV and WFMN) are significantly higher than those associated with a modern, quiet site (i.e., about 2  $m\mu$  peak-to-peak at 1 Hz). With respect to this ideal noise background, Lg would probably be detectable at all four stations\*, but detection of the

\* Scaling data are not presently available for CPO. However, the signal level can be roughly approximated assuming nominal Lg distance attenuation with respect to the signal level recorded at EUAL.

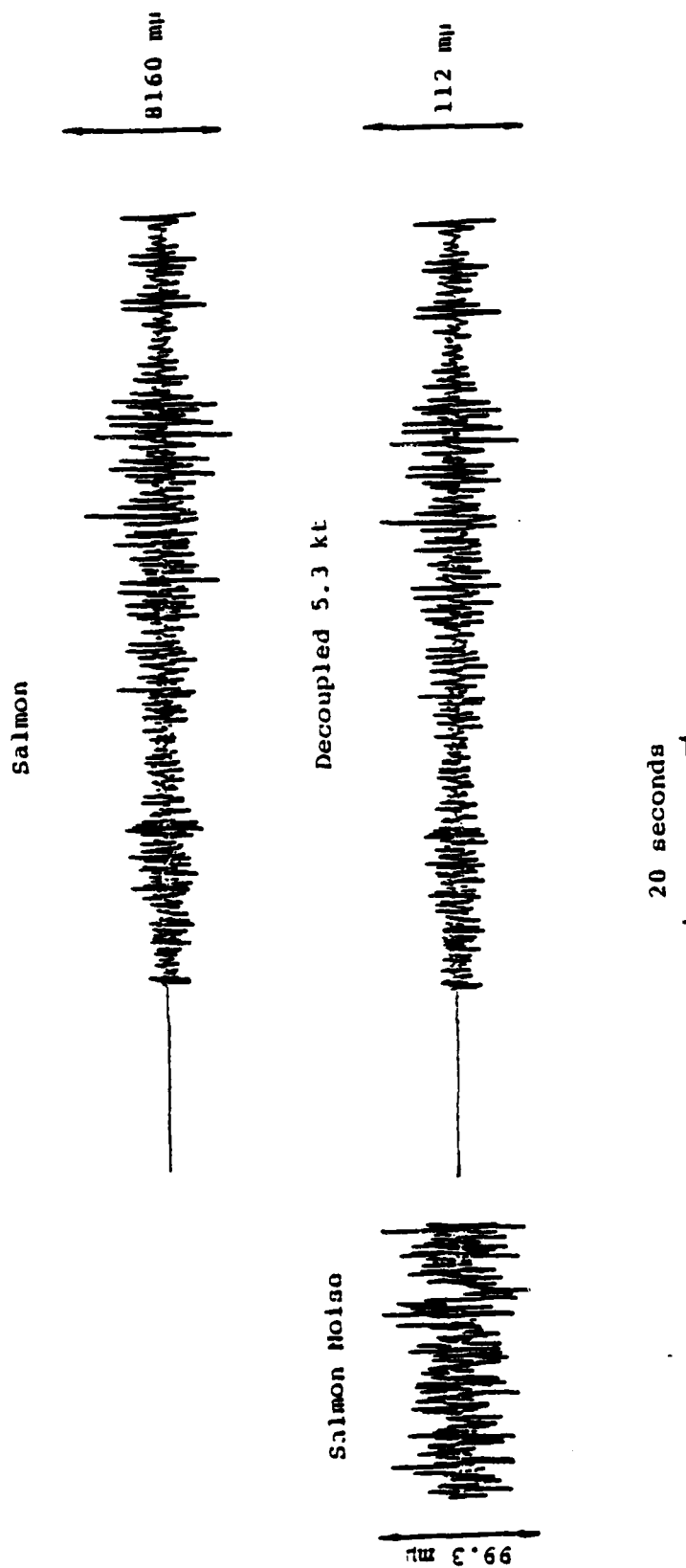


Figure 2.3. Comparison of observed SALMON and simulated decoupled vertical component seismograms, station EUAL.

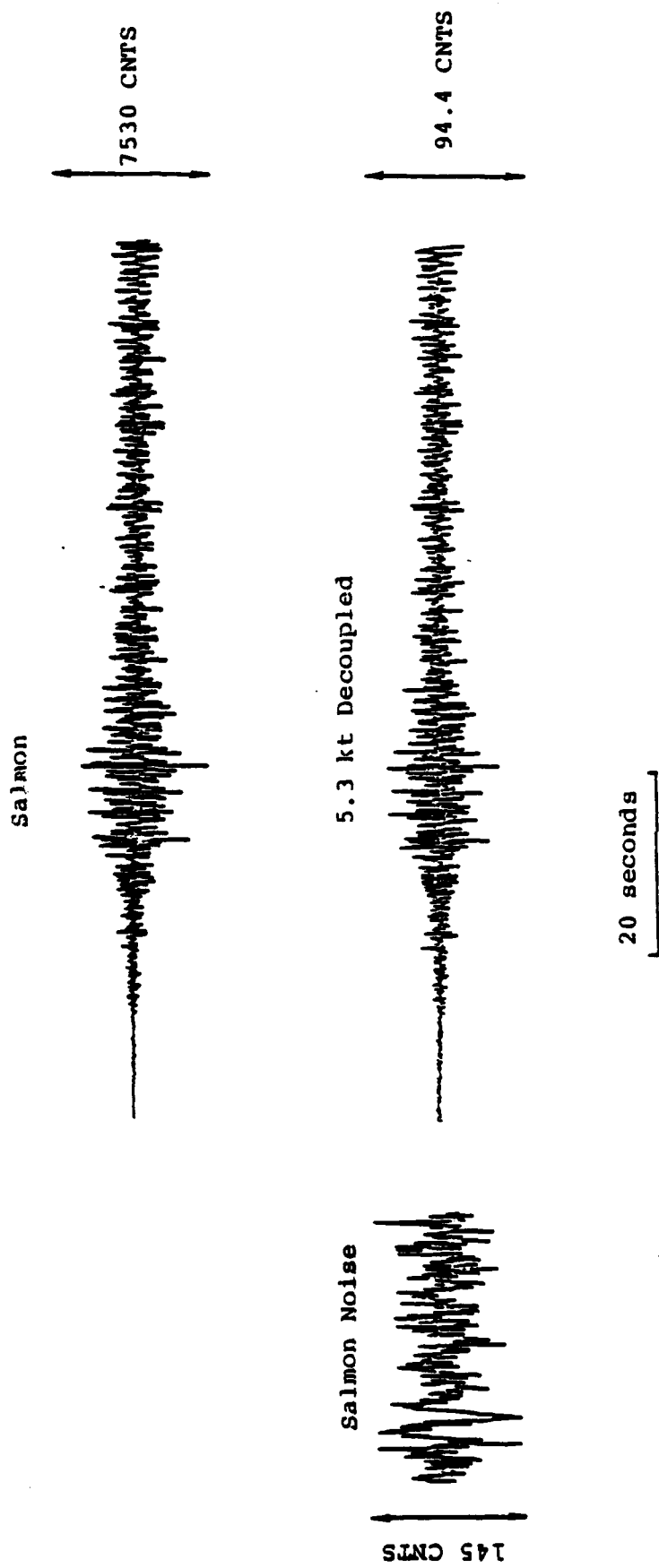
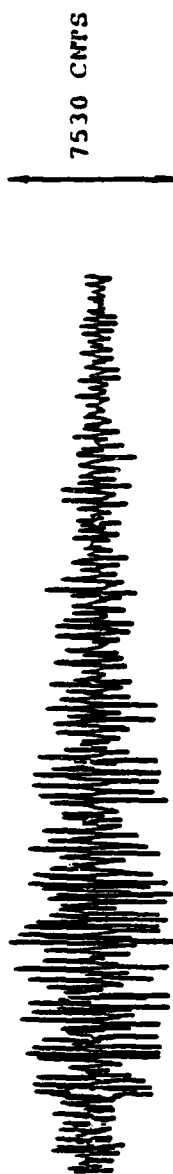
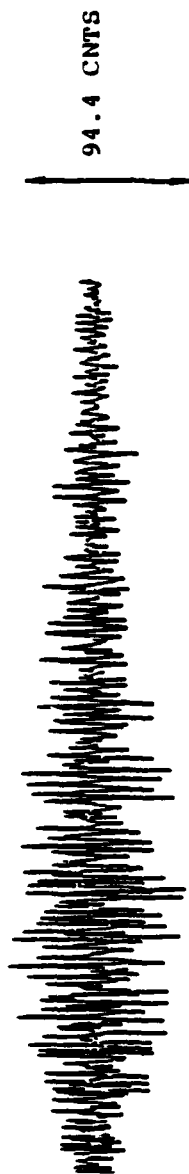


Figure 2.4. Comparison of observed SALMON and simulated decoupled vertical component seismograms, station CPO.

Salmon



5.3 kt Decoupled



20 seconds

Salmon Noise



Figure 2.4. Continued.

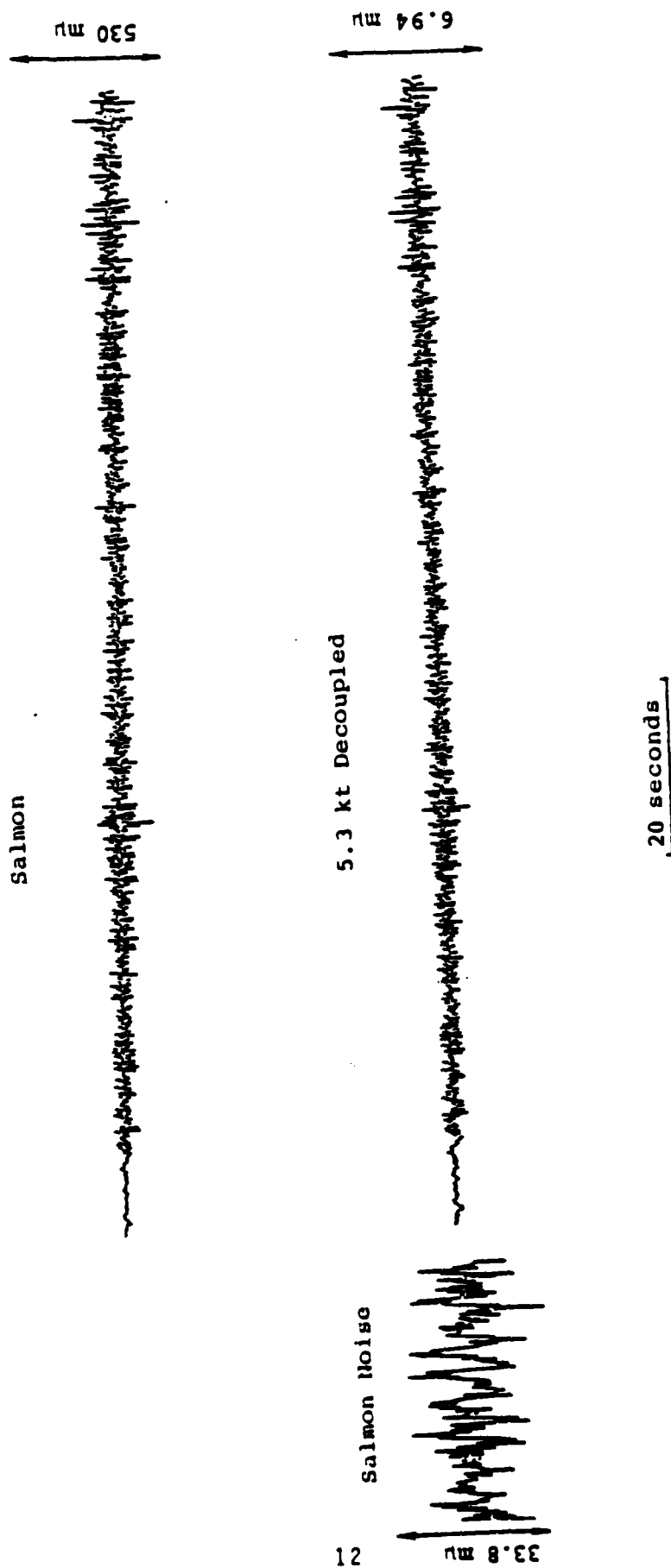


Figure 2.5. Comparison of observed SALMON and simulated decoupled vertical component seismograms, station BLWV.

Salmon



Salmon Noise

5.3 kt Decoupled



20 seconds

Figure 2.5. Continued.

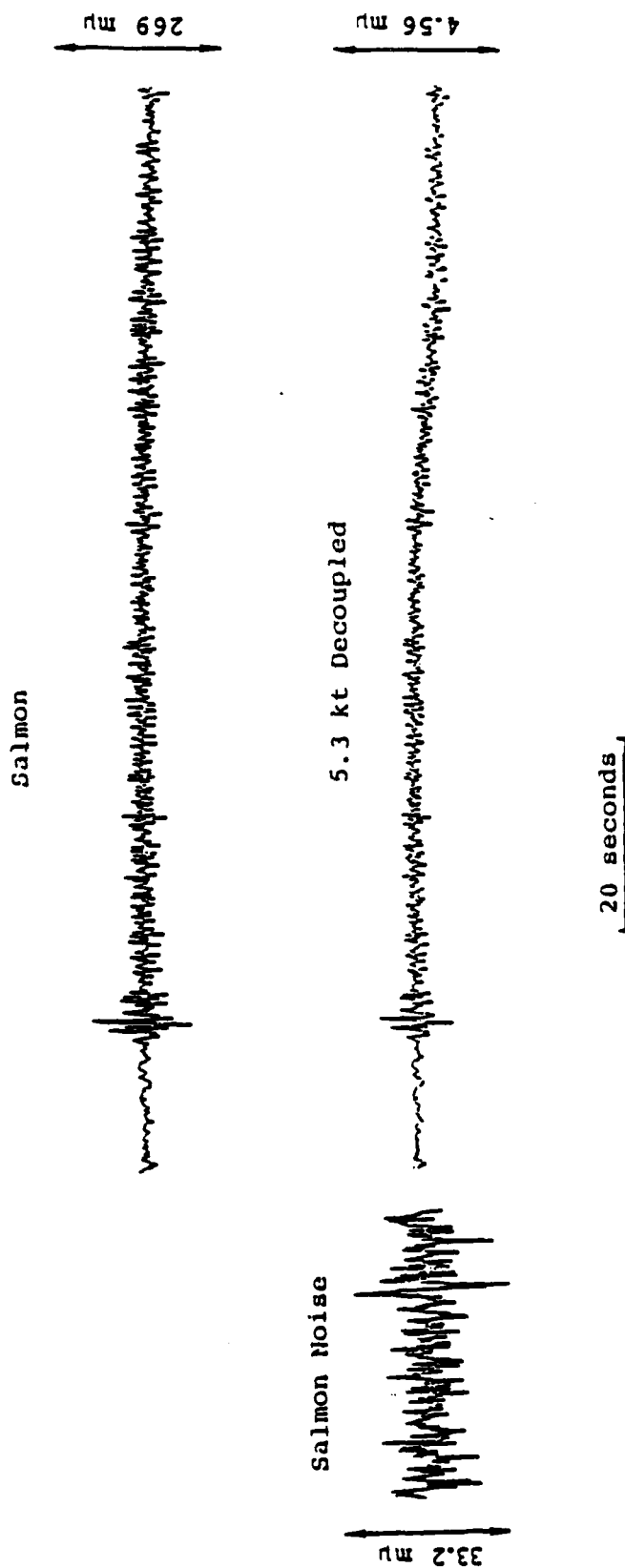


Figure 2.6. Comparison of observed SALMON and simulated decoupled vertical component seismograms, station WFMN.

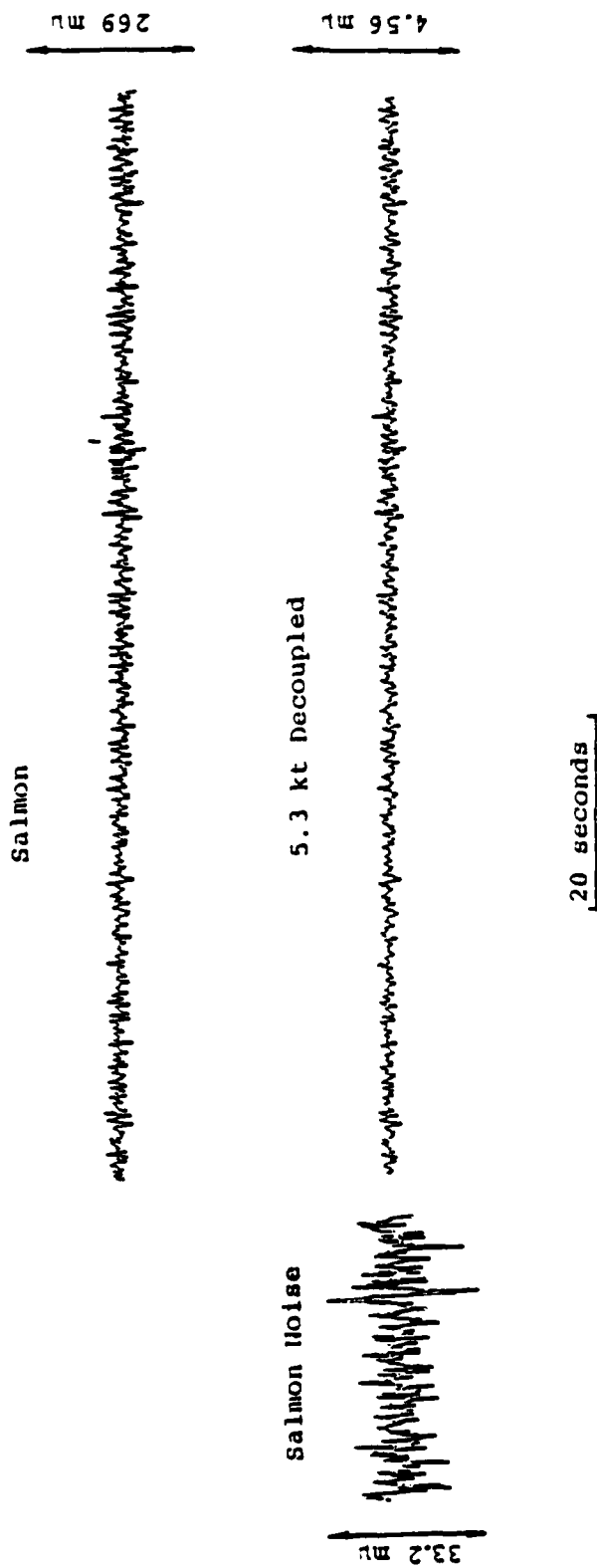


Figure 2.6. Continued

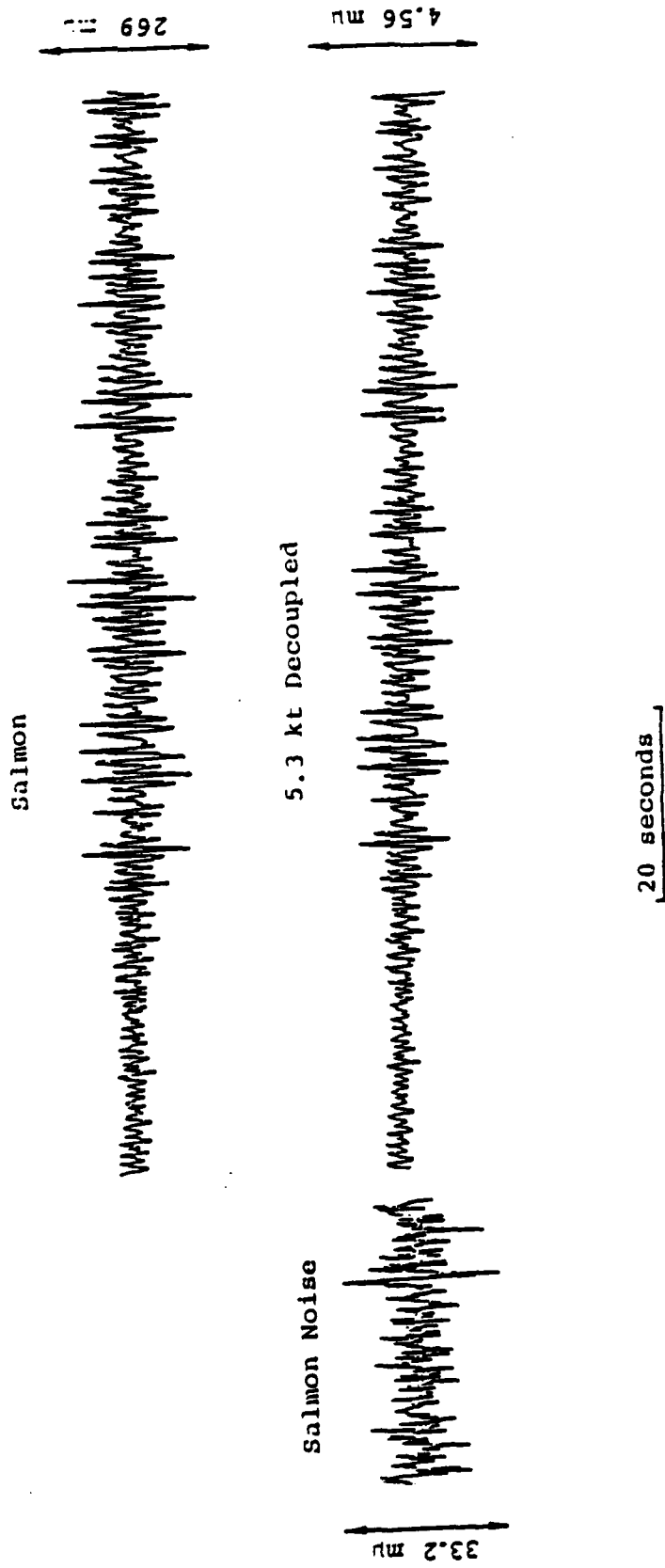


Figure 2.6. Continued.

initial P wave motion would be questionable at the two distant stations (BLWV and WFMN) using the available narrowband data.

The above results apply to data recorded through narrowband instruments and, therefore, tell us little about frequency dependent detectability. We have tried to remedy this by correcting for instrument response. Our ability to accomplish this is limited by two factors; (1) the sampling rate used in digitizing the analog data and, (2) the frequency dependent signal-to-noise ratio. The available data were sampled at a rate of 20 samples/second, which limits us to frequencies below 10 Hz. Estimates of the signal and noise spectra for the four stations are shown in Figures 2.7 to 2.14. For each station, smoothed signal spectra (solid) corresponding to 50 second P and Lg windows are compared with the smoothed noise spectrum (dashed) computed from the 50 second window immediately preceding the first arrival. The dotted lines on these figures correspond to estimates of the decoupled signal spectra obtained by scaling down the corresponding SALMON spectra, using the decoupling factor shown in Figure 2.2. It can be seen that the SALMON signal-to-noise ratios at EUAL, CPO, and BLWV are good over the frequency range from 0.5 to 10 Hz, while those for the most distant station (WFMN) fall below unity at both high and low frequencies. Figures 2.15 to 2.17 compare the uncorrected and selected corrected bandwidths for the four stations, assuming a nominal short-period instrument response for each. (The actual system responses at these stations during SALMON varied somewhat and therefore the derived instrument correction factors are only approximate). The instrument-corrected ground motions for the four stations are shown in Figures 2.18 to 2.21 (center), where they are compared with the original SALMON recordings (top) and the simulated, instrument-corrected ground motions from the 5.3 KT decoupled explosion (bottom). Here the accompanying noise samples correspond to instrument-corrected versions of those shown in Figures 2.3 to 2.6. It can be seen that the instrument correction significantly changes the character of the

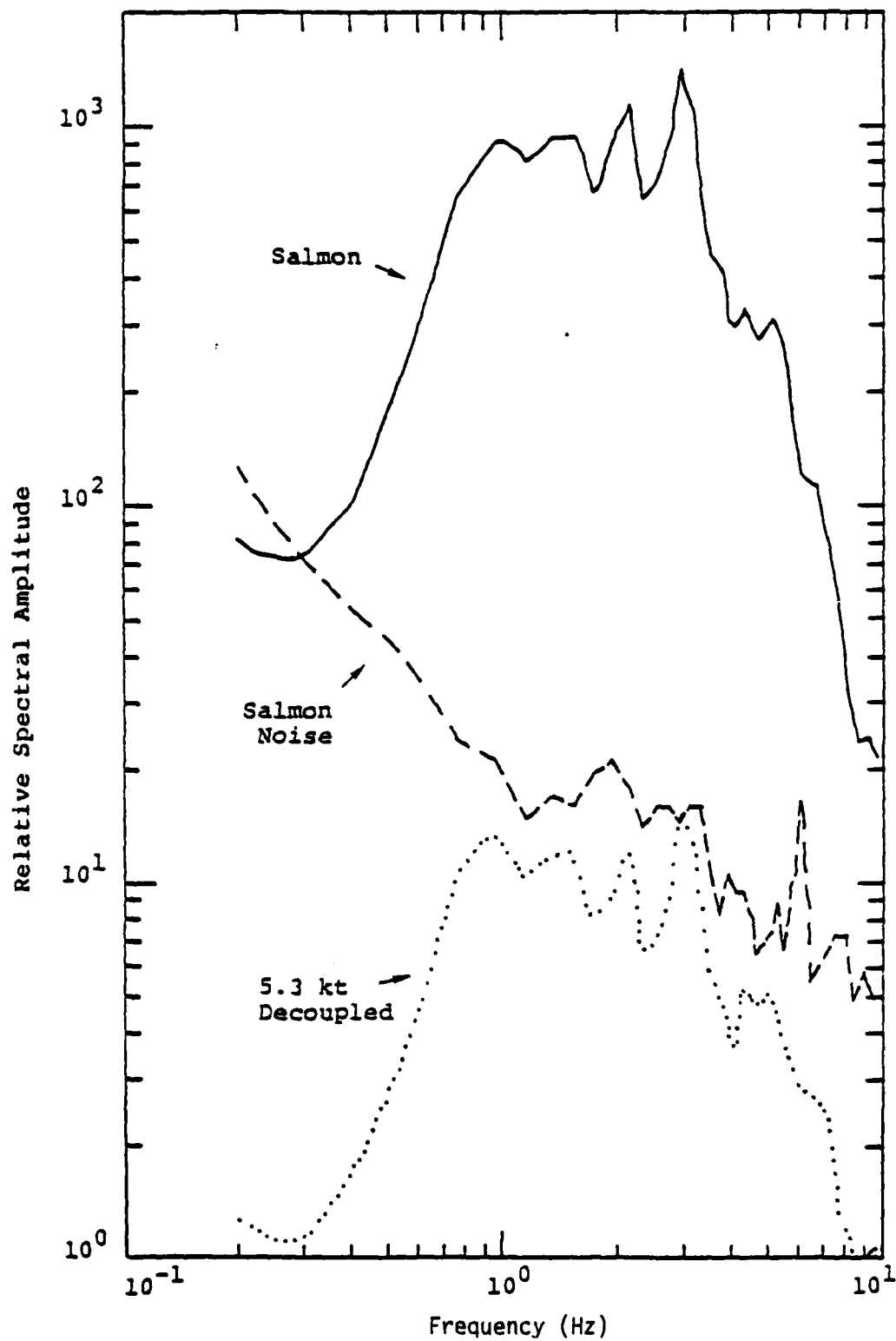


Figure 2.7. Comparison of P wave and noise spectral amplitude levels, station EUAL.

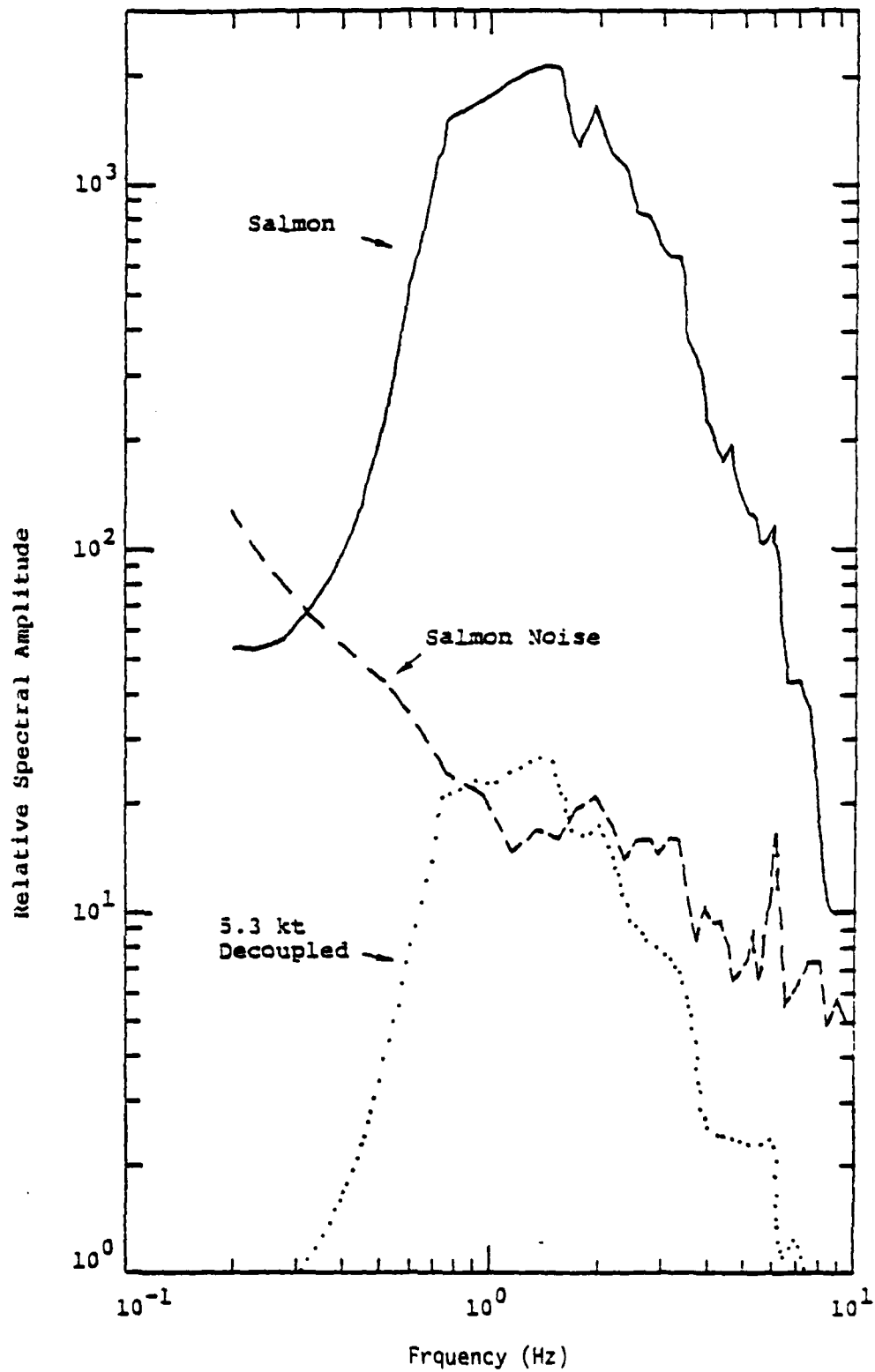


Figure 2.8. Comparison of  $L_g$  and noise spectral amplitude levels, station EUAL.

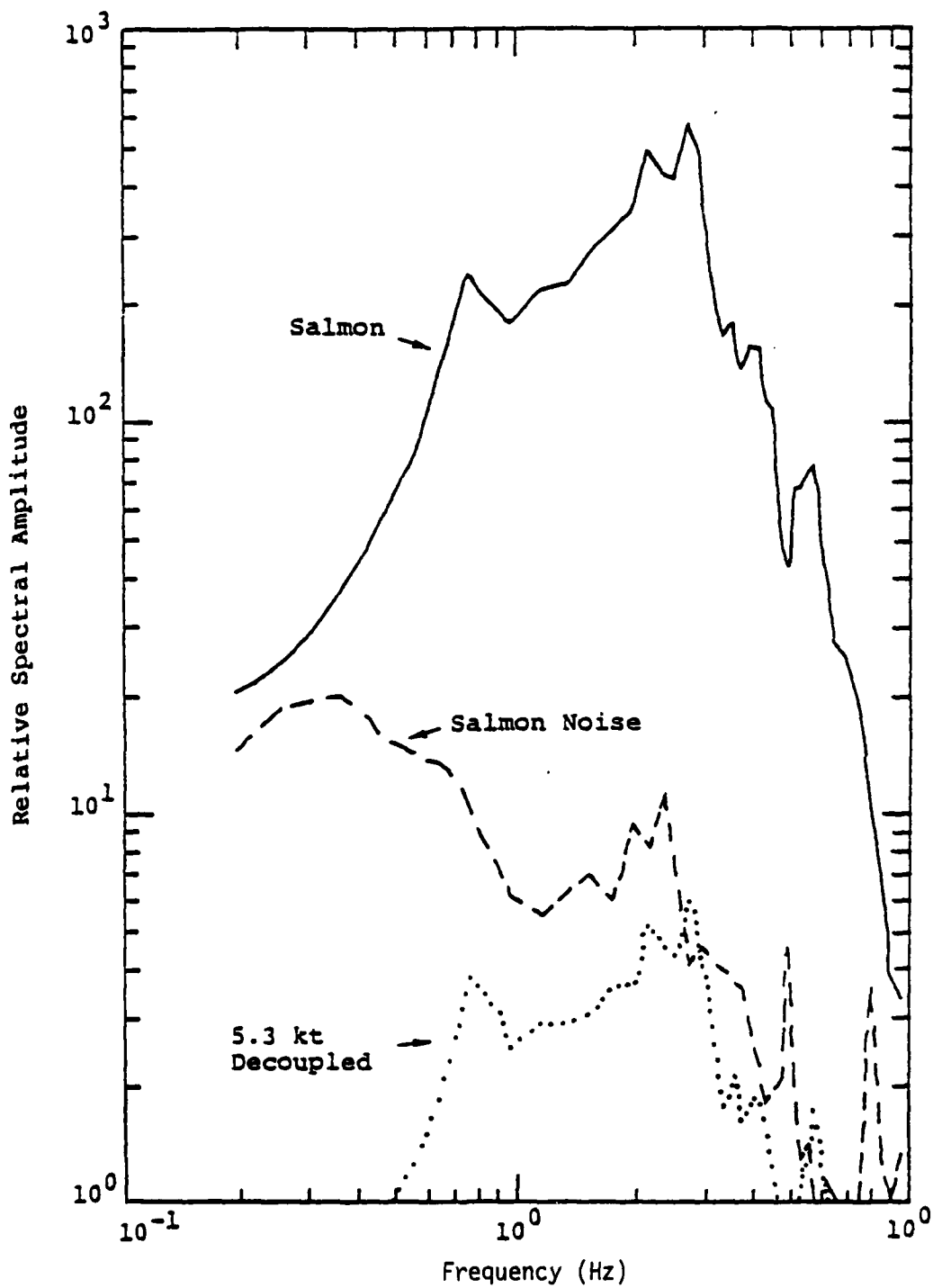


Figure 2.9. Comparison of P wave and noise spectral amplitude levels, station CP0.

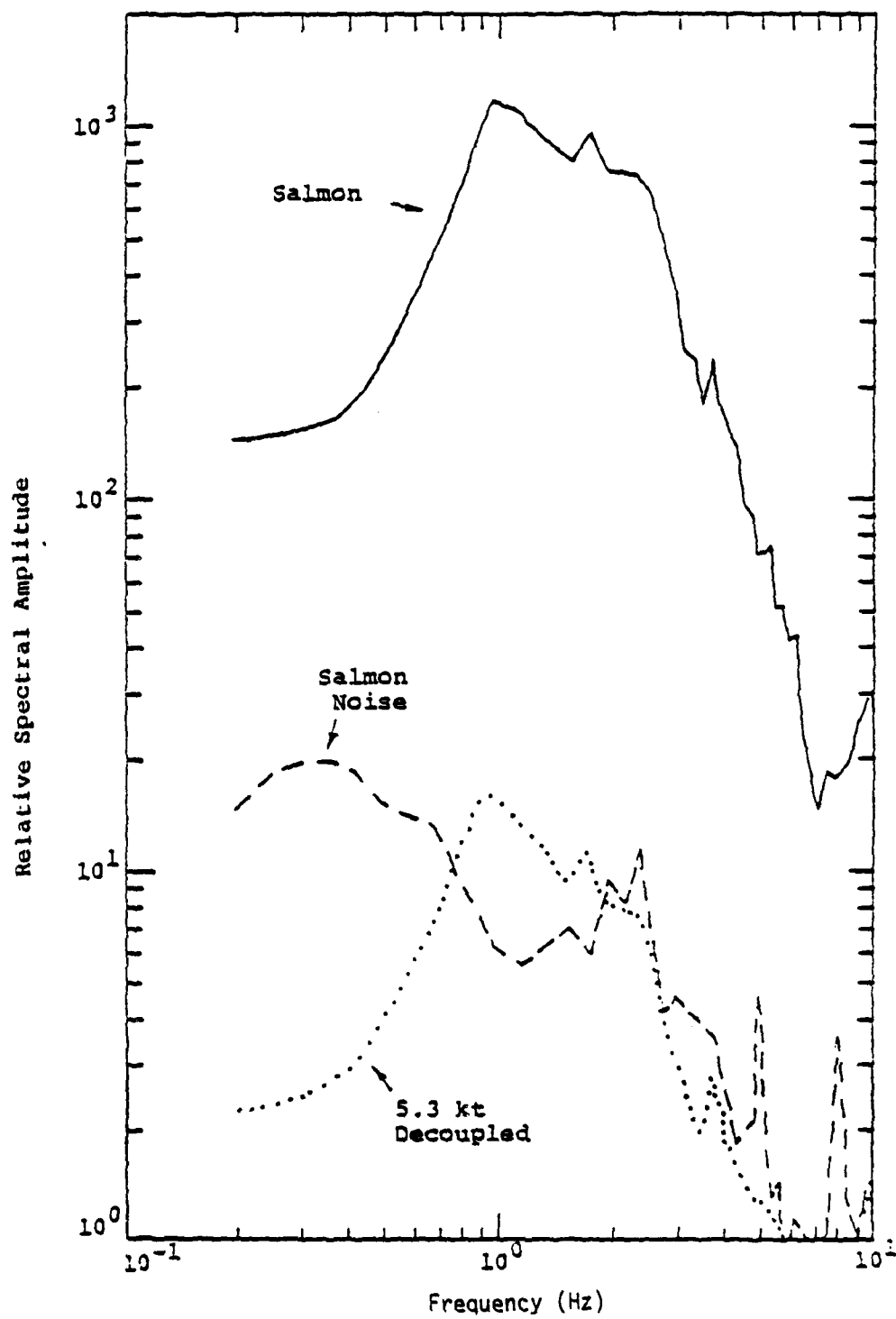


Figure 2.10. Comparison of  $L_g$  and noise spectral amplitude levels, station CPO.

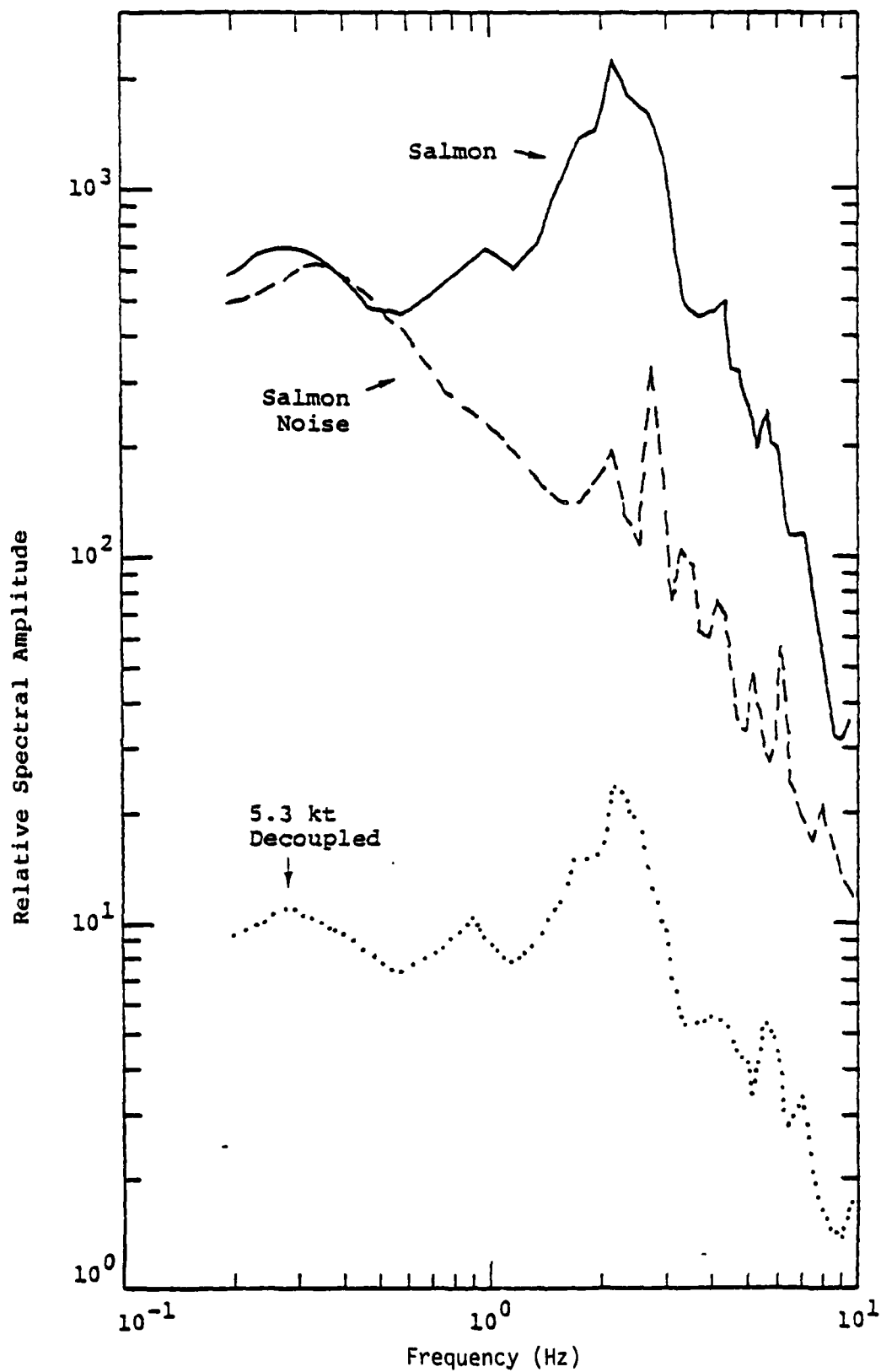


Figure 2.11. Comparison of P wave and noise spectral amplitude levels, station BLWV.

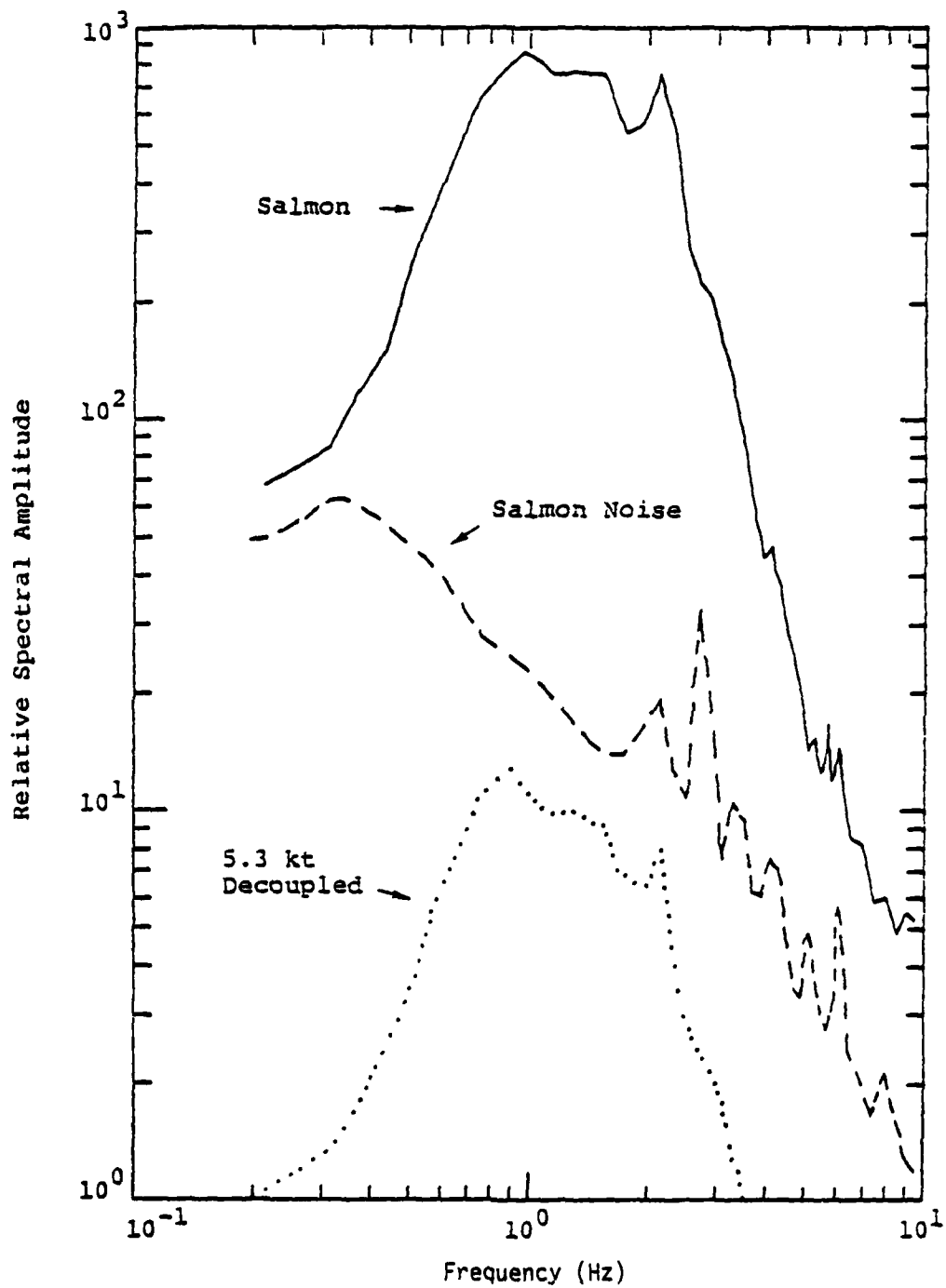


Figure 2.12. Comparison of  $L_g$  and noise spectral amplitude levels, station BLWV.

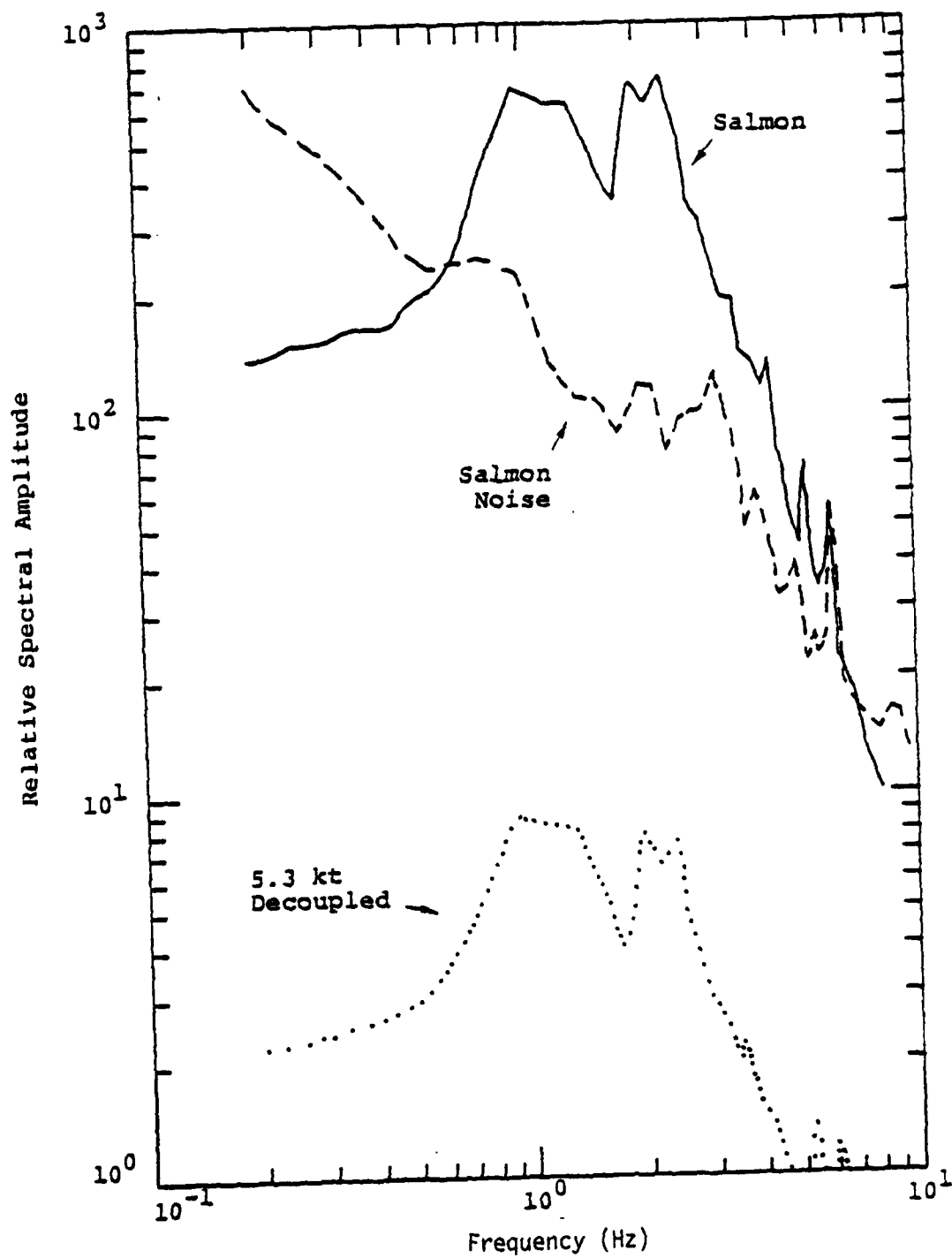


Figure 2.13. Comparison of P wave and noise spectral amplitude levels, station WFMN.

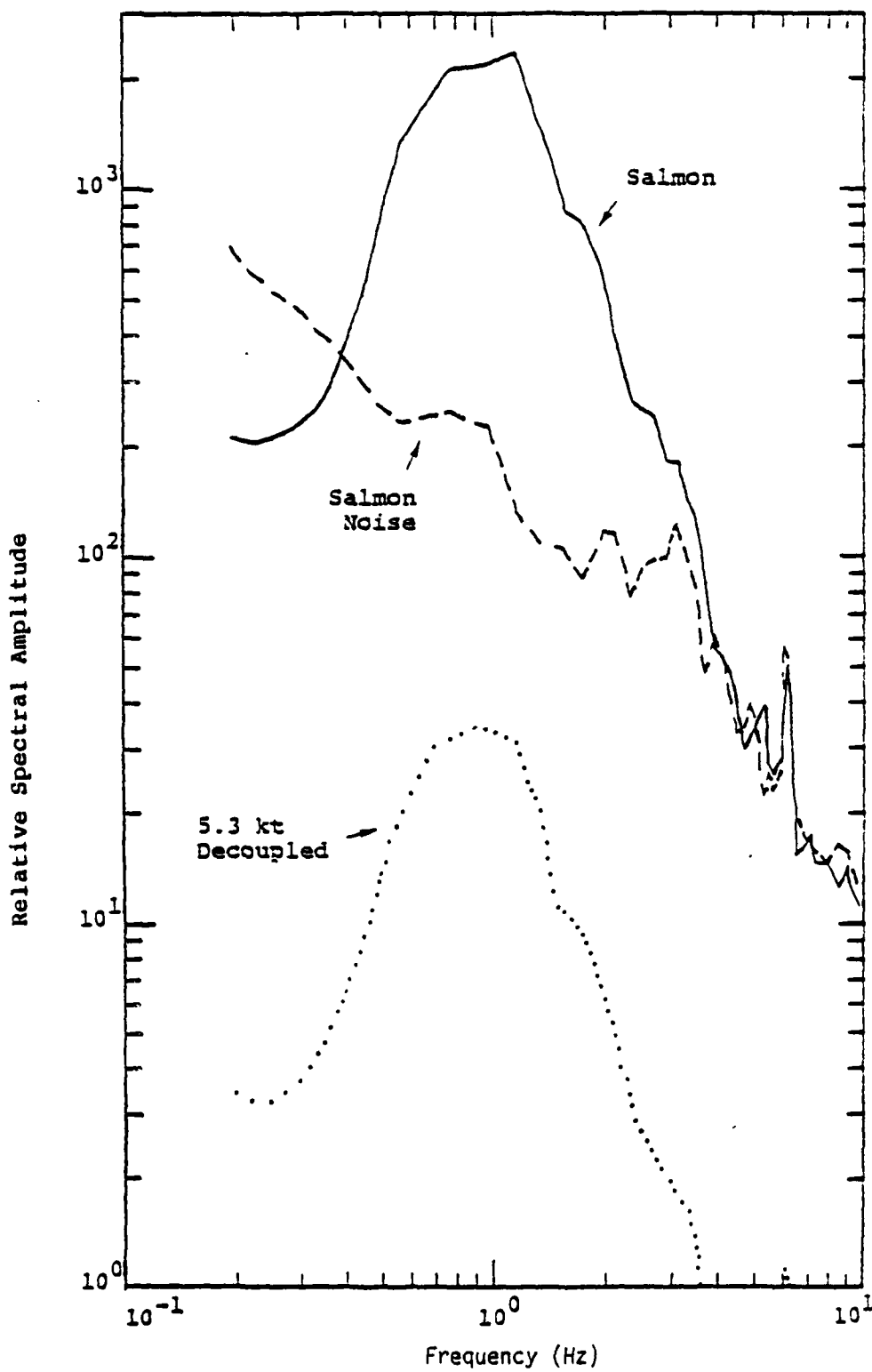


Figure 2.14. Comparison of  $L_g$  and noise spectral amplitude levels, station WFMN.

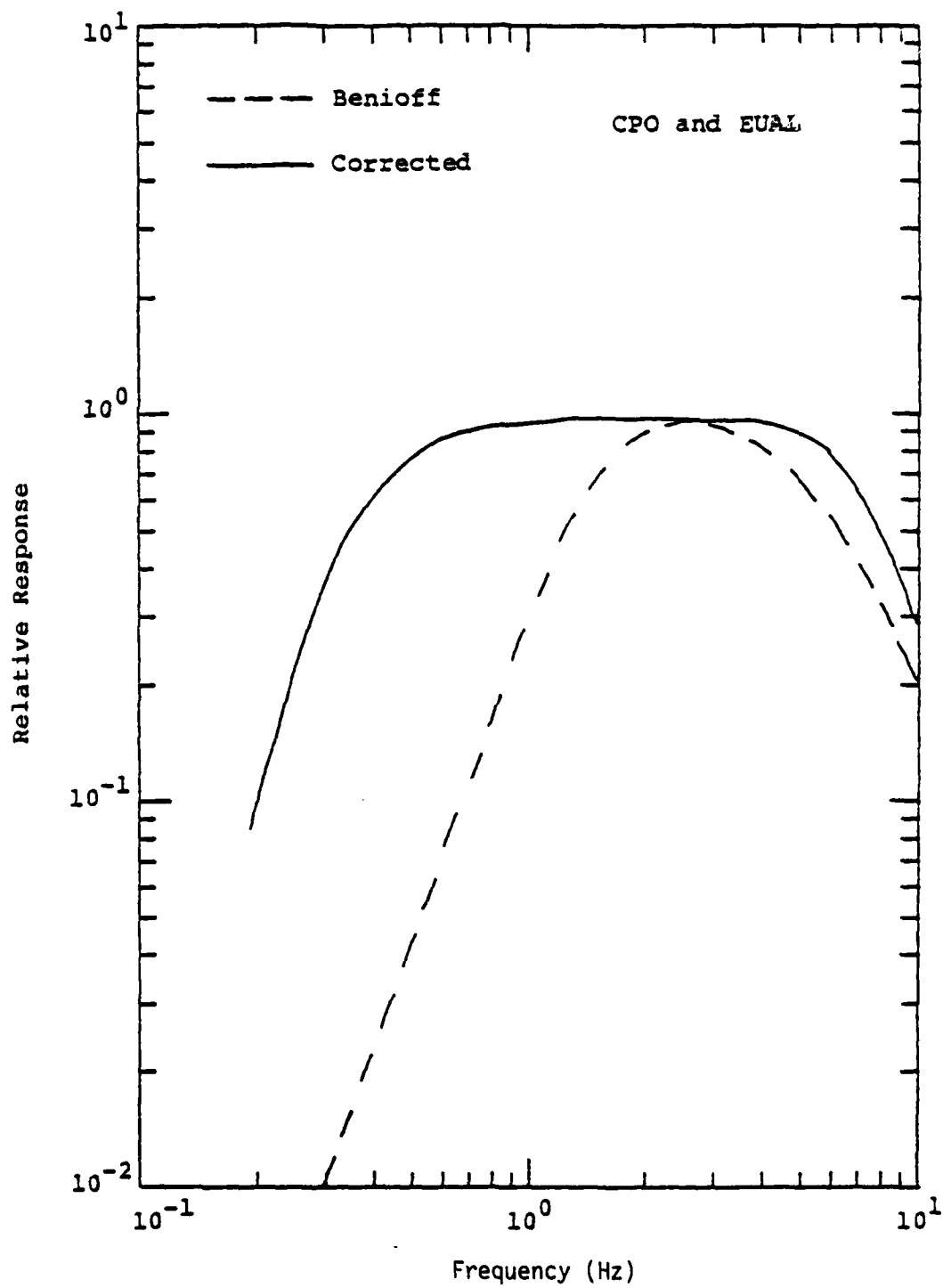


Figure 2.15. Comparison of uncorrected and corrected instrument response for stations CPO and EUAL.

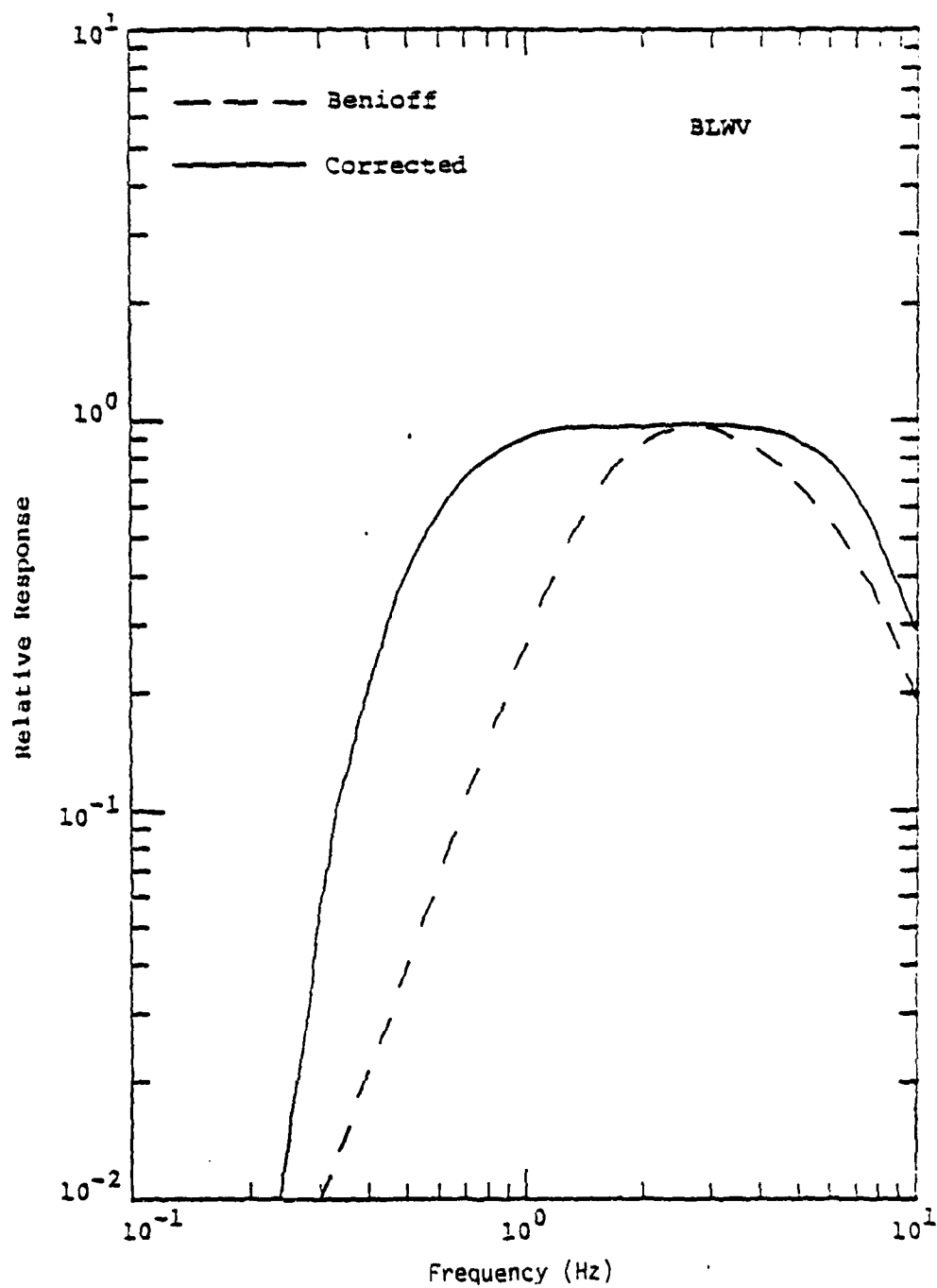


Figure 2.16. Comparison of uncorrected and corrected instrument response for station BLWV.

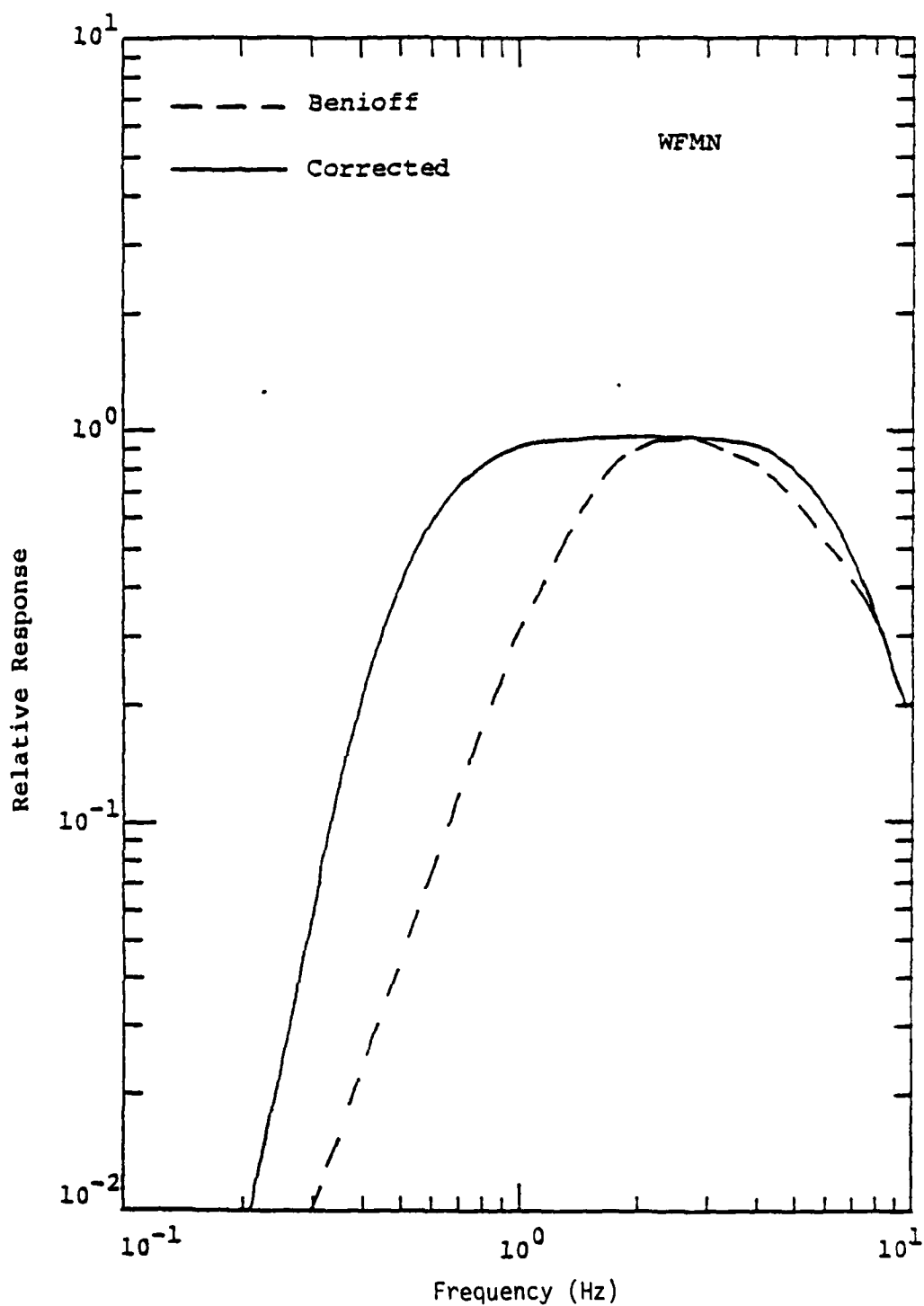


Figure 2.17 . Comparison of uncorrected and corrected instrument response for station WFMN.

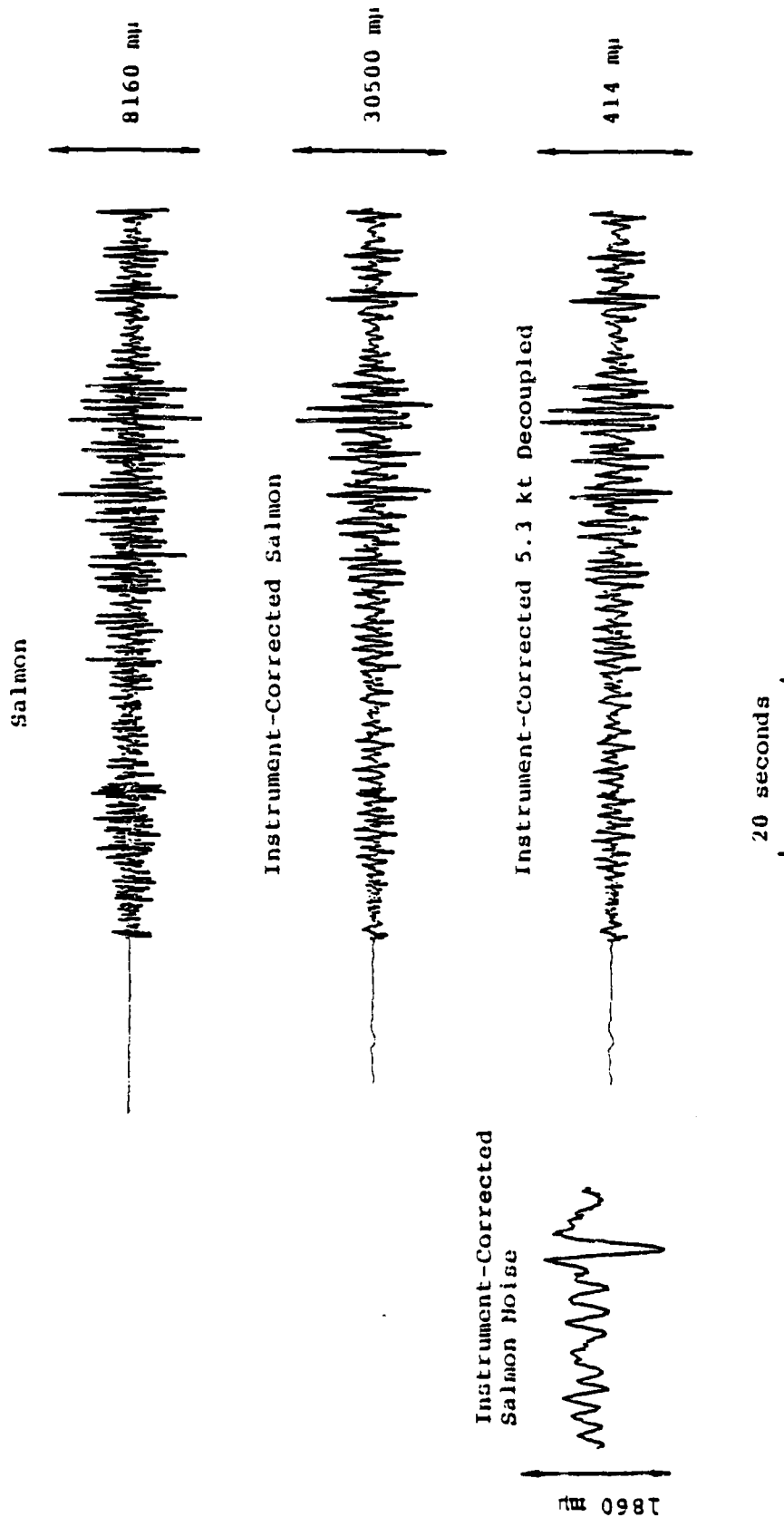


Figure 2.18. Comparison of instrument-corrected SALMON and simulated decoupled vertical component seismograms, station EUAL.

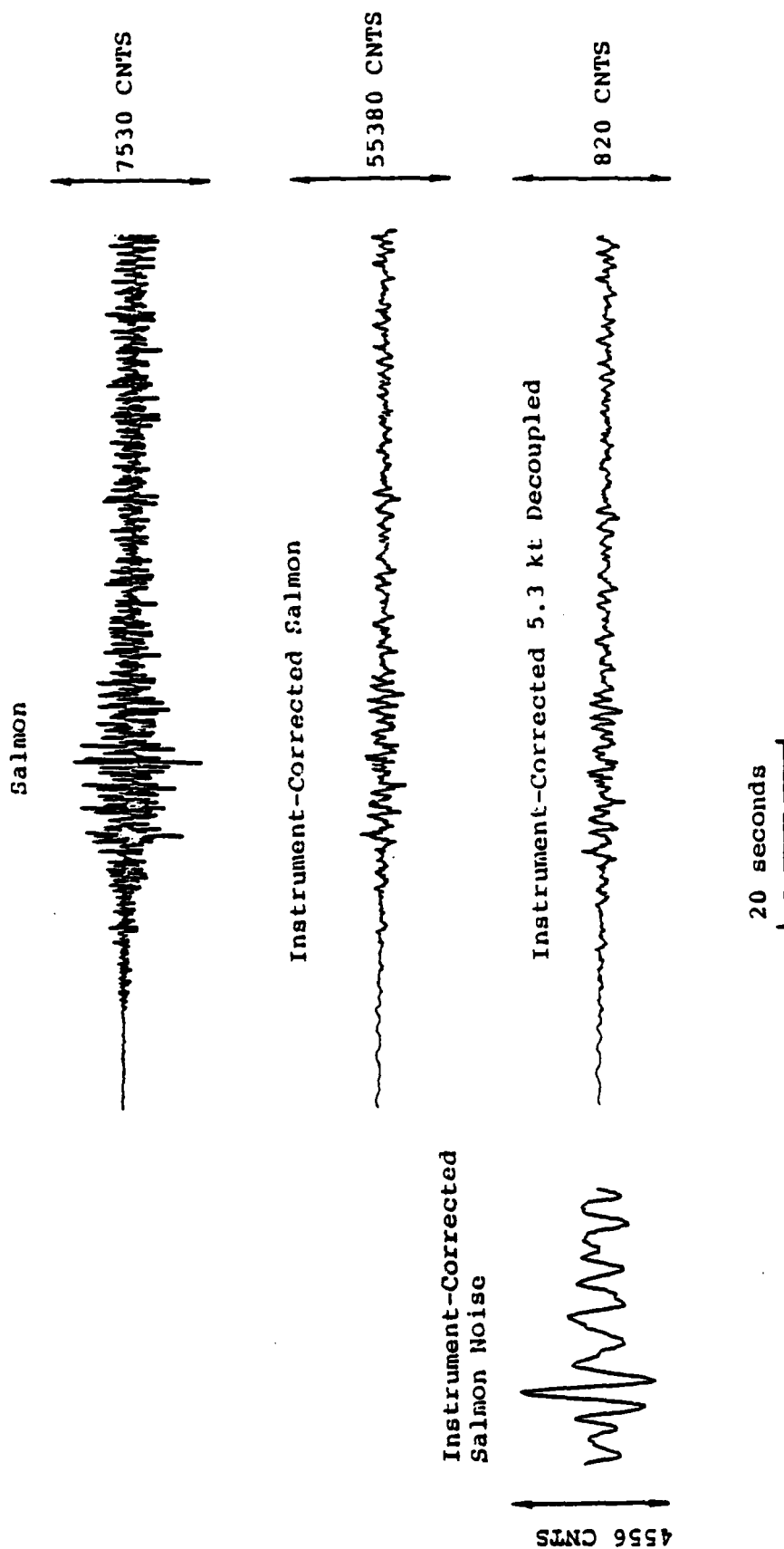


Figure 2.19. Comparison of instrument-corrected SALMON and simulated decoupled vertical component seismograms, station CP0.

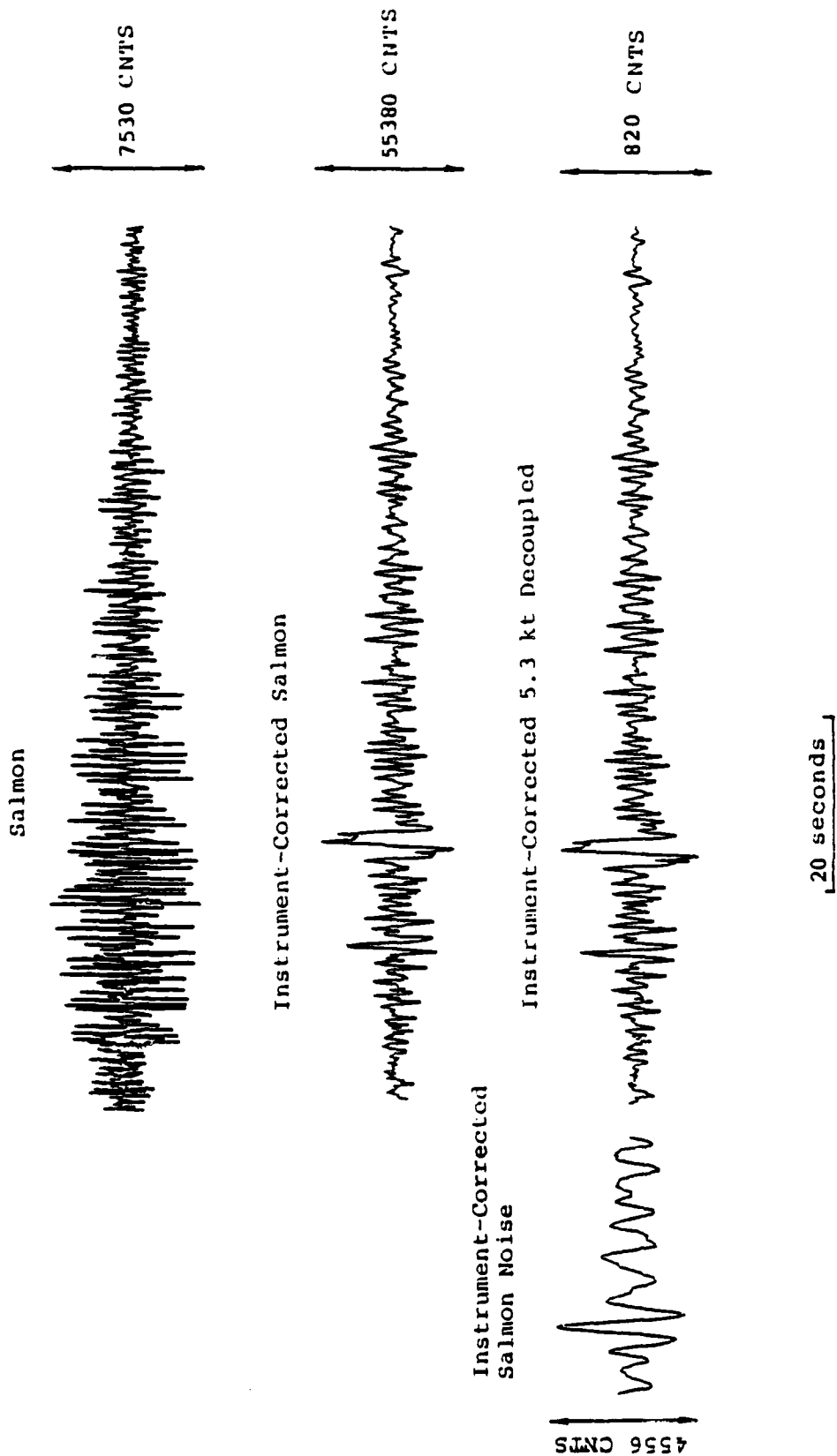
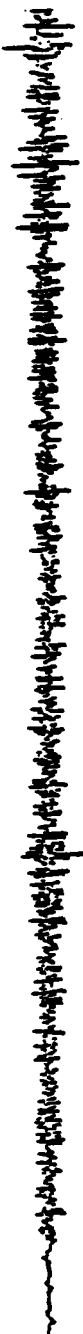


Figure 2.19. Continued.

Salmon

530 mV



Instrument-Corrected Salmon

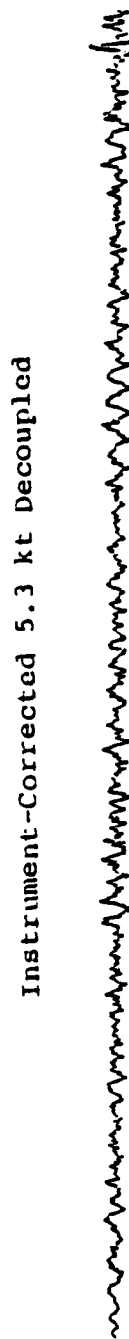
2050 mV



Instrument-Corrected  
Salmon Noise

32

29.4 mV



Instrument-Corrected 5.3 kt Decoupled

20 seconds

Figure 2.20. Comparison of instrument-corrected SALMON and simulated decoupled vertical component seismograms, station BLWV.

Salmon



Instrument-Corrected Salmon



Instrument-Corrected  
Salmon Noise

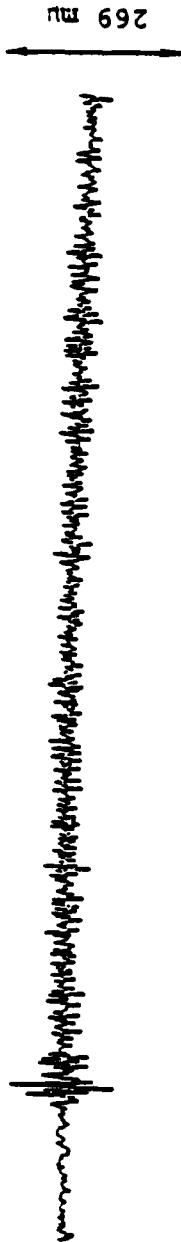
Instrument-Corrected 5.3 kt Decoupled



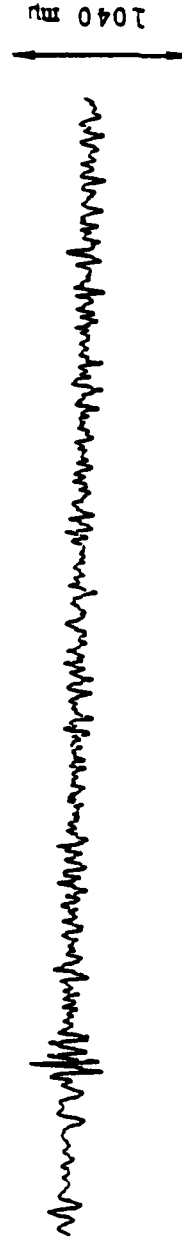
20 seconds

Figure 2.20. Continued.

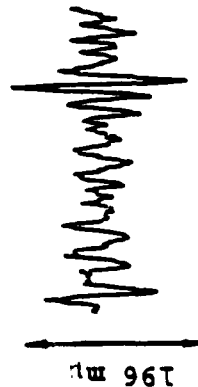
Salmon



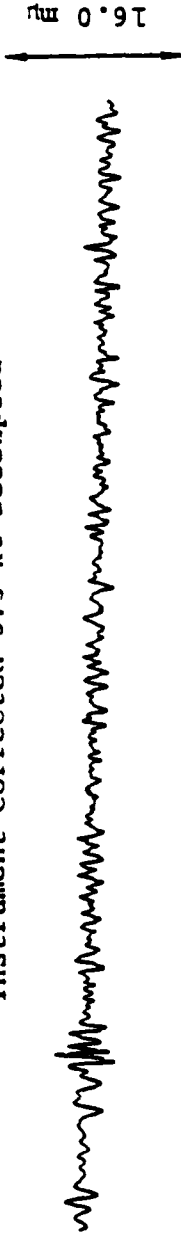
Instrument-Corrected Salmon



Instrument-Corrected  
Salmon Noise



Instrument-Corrected 5.3 kt Decoupled



20 second

Figure 2.21. Comparison of instrument-corrected SALMON and simulated decoupled vertical component seismograms, station WFMN.

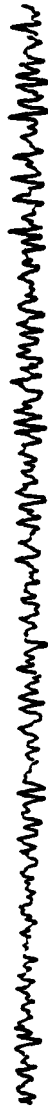
Salmon

269 mμ



Instrument-Corrected Salmon

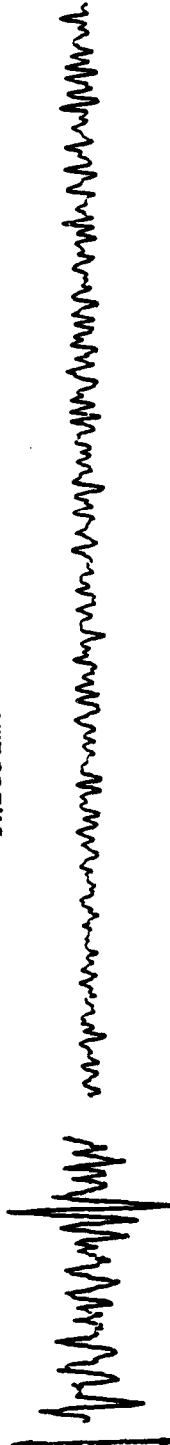
1040 mμ



Instrument-Corrected  
Salmon Noise

Instrument-Corrected 5.3 kt Decoupled

16.0 mμ

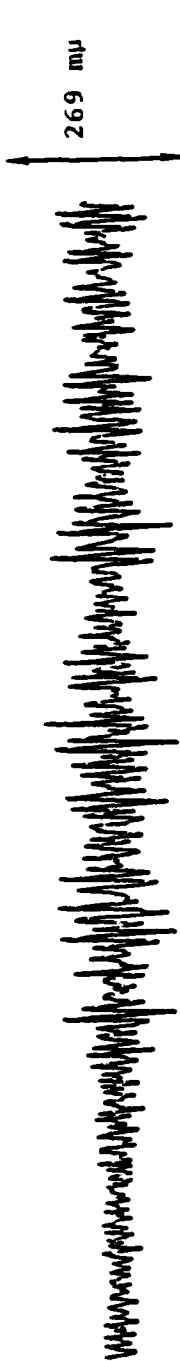


20 seconds



Figure 2.21. Continued.

Salmon



Instrument-Corrected Salmon



Instrument-Corrected  
Salmon Noise

Instrument-Corrected 5.3 kt Decoupled



20 seconds

Figure 2.21. Continued.

recordings, particularly at stations EUAL and CPO. However, comparisons with Figures 2.3 to 2.6 indicate that the effective signal-to-noise ratios predicted by the decoupling simulation actually decrease after correction for instrument response. This reflects the fact that the noise level increases with decreasing frequency while the decoupling factor remains essentially constant. Thus, in this case, it is the high frequency information which is of greatest potential utility and corrections for low frequency instrument response characteristics are not expected to improve detection capability. However, because of the limited sampling rate, it has not been possible to quantitatively evaluate high frequency detectability using these data.

A final question is whether any implications can be drawn from these data concerning either the SALMON source function or anelastic attenuation in the eastern United States. Figure 2.22 shows a comparison of the instrument-corrected (JM) SALMON P wave spectrum from CPO with a theoretical P wave spectrum obtained by multiplying an analytic approximation to the SALMON source function (Murphy, 1969) times an attenuation operator,  $e^{-\pi f t^*}$ , with  $t^* = 0.075$ . It can be seen that the agreement between the two is quite good for frequencies above 1 Hz. Below 1 Hz the two curves diverge, but it seems likely that this is due to the relatively long time window (i.e. 50 seconds) used in computing the P wave spectrum. That is, the selected window includes late-arriving, lower frequency components which attenuate less rapidly than the first arriving P wave phases. The quality of the fit above 1 Hz suggests both that the selected SALMON source function is about right, and that the anelastic attenuation is quite low for this particular eastern United States travel path. In fact, with  $t^* = r/cQ$ , where  $r$  is the travel path length and  $c$  the velocity of the phase under consideration, it follows that  $Q = r/ct^*$ . For  $r \geq \Delta$  and, at this range,  $c < 8$  km/sec, and it follows that a  $t^*$  value of 0.075 corresponds to an average path  $Q$  value of at least 1000.

In summary, regional SALMON data recorded at four eastern United States stations have been theoretically scaled to simulate the seismograms to be expected from a fully decoupled 5.3 KT

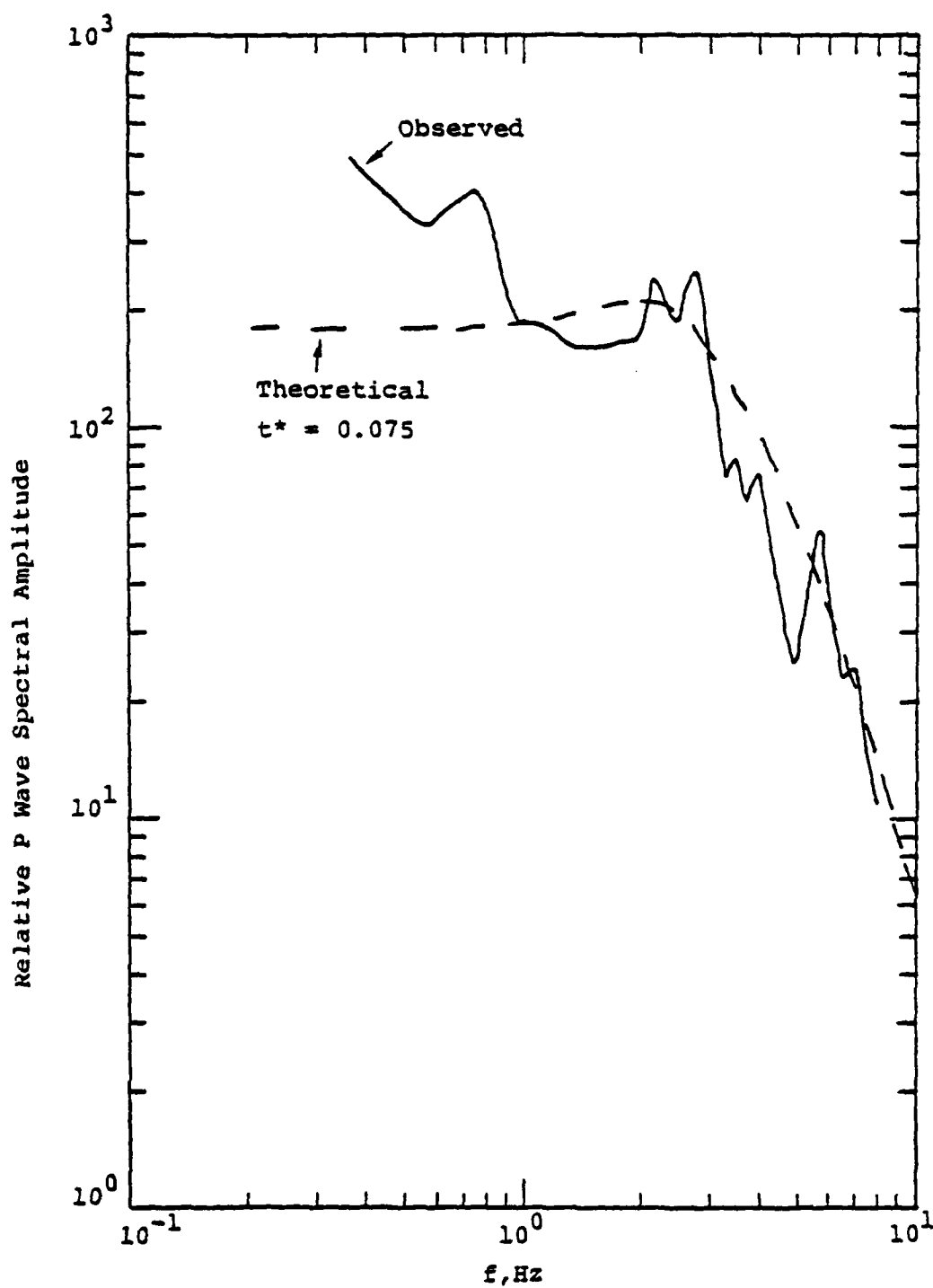


Figure 2.22. Comparison of theoretical and instrument-corrected observed P wave spectra, station CP0.

explosion at the SALMON shotpoint. It has been found that, relative to the noise background prevailing during SALMON, such an explosion would probably have been detectable on the short-period recordings from the two nearer stations (EUAL,  $\Delta = 246$  km and CPO,  $\Delta = 623$  km), but not from those expected at the more distant stations (BLWV,  $\Delta = 1065$  km and WFMN,  $\Delta = 1437$  km). With respect to the lower noise background expected at a modern, quiet site, the Lg phase from such a decoupled explosion would probably be detectable at all four stations, but initial P wave detection would still be questionable at the two distant stations. Furthermore, as might be expected on the basis of previous noise studies, increasing the effective bandwidth of the short-period data to encompass lower frequencies does not improve this detectability due to the fact that the noise level increases with decreasing frequency, while the decoupling factor remains essentially constant. By the same argument, consideration of higher frequency data should improve detectability, at least for high Q paths. However, it has not been possible to quantitatively evaluate this potential improvement, using the available data set, due to the relatively low sampling rate employed in the digitization. Therefore, it is recommended that selected SALMON data be redigitized at a higher rate so that frequency dependent detection thresholds can be assessed for these eastern United States paths.

THIS PAGE LEFT BLANK

### III. YIELD ESTIMATION FROM SURFACE WAVE RECORDINGS OF UNDERGROUND EXPLOSIONS — A REVIEW

#### 3.1 INTRODUCTION

In this section we summarize the results from several studies of surface waves that have been done over the past several years. The main objective in this work has been to understand the parameters that control single station recordings of the surface waves. This is said to contrast our approach from alternatives in which the data are represented by network quantities like  $M_s$ .

This review includes four topics which are discussed in separate sub-sections. First, we summarize a study of Airy phase amplitudes of NTS explosions recorded at the WWSSN stations ALQ and TUC. The purpose of this study was to delineate the amplitude differences among events in different source materials. These differences are compatible with the differences seen in  $M_s$  data, where the two can be compared. The ALQ and TUC observations are the primary data base for subsequent synthetic seismogram studies.

The second topic, discussed in Section 3.3, is the inference of explosion reduced displacement potential (RDP) amplitudes from comparison of synthetic and observed waveforms. The synthetics are computed with an RDP source in plane-layered earth models. The capability to construct synthetic seismograms with such models is widely available, and it is important to see how well it can explain the data. Of course, the connection between explosion yield and RDP amplitude is another area where our understanding is incomplete, but this is not a topic for discussion here.

Attempts to use theoretical models to quantitatively explain the data have not often been made. The study of ALQ and TUC data summarized in Section 3.3 is, perhaps, the most complete. This study demonstrates that the models do give results that are in fairly good agreement with the data. However, the comparison of theoretical and observed seismograms also highlights those features that cannot be explained with simple source and path models. In

Section 3.4 we discuss the most important higher order source contributions and the extent to which their effects can be delineated with elastic point source models. While the seismogram synthesis can handle equivalent elastic point sources of arbitrary complexity, the problem is in specifying the source components. To do so, an improved understanding of the physics of explosions in two- and three-dimensions is required. The capability to move in that direction is now available, as evidenced by the results from two-dimensional, axisymmetric source calculations which are discussed in Section IV of this report.

The final topic of this summary is discussed in Section 3.5. In that section we point out that many underground explosions are characterized by strong radiation patterns, but that a satisfactory explanation for the origin of this phenomenon is not yet available. The conventional idea that a double-couple source is superimposed on the explosion qualitatively explains many of the observations, but quantitative corrections cannot confidently be made and many important features remain unexplained. These points are illustrated by a summary of results from a study of the waves from MIGHTY EPIC and DIABLO HAWK, two nearly identical events at Rainier Mesa.

We conclude this review with a summary of the main conclusions in Section 3.6. The theoretical techniques are available to model most, if not all, of the important parameters controlling surface waves and there are ample data. More systematic modeling studies are needed to clearly define the uncertainty in yield estimation when the most powerful theoretical techniques are employed.

### 3.2 EXPERIMENTAL DETERMINATION OF THE DEPENDENCE OF RAYLEIGH WAVE AMPLITUDE ON PROPERTIES OF THE SOURCE MATERIAL

There have been numerous studies in which Rayleigh wave amplitude, usually indicated by  $M_s$ , is plotted versus explosion yield. Events are often separated according to characteristics of the source materials and some dependence is sought. We have done a similar study using the Airy phase amplitudes measured on recordings

at the WSSN stations ALQ and TUC. These stations are at ranges from 700 to 900 kilometers and record small events not usually present in  $M_S$  data sets. As a disadvantage, they are off-scale for events much larger than 300 KT.

The results of this study were described in a 1977 Systems, Science and Software (S<sup>3</sup>) Quarterly Report by Bache, Goupillaud and Mason. The Airy phase data were compared to  $M_S$  data compiled by Eisenhauer (1976). The Airy phase amplitudes were converted to  $M_S$  values using the formulas:

$$\text{ALQ: } M_S^A = \log A + 2.72,$$

$$\text{TUC: } M_S^T = \log A + 2.17,$$

where the constants were chosen to make  $M_S^A$  and  $M_S^T$  about the same, on the average, as Eisenhauer's  $M_S$ . An  $M_S$  was then taken to be the mean of  $M_S^A$  and  $M_S^T$ .

The data were separated by test area and a linear least square fit was made for each population when plotted versus log yield. The linear best-fit equations, together with the standard deviations, are as follows (the number of events is listed in parentheses and B is an arbitrary constant):

Pahute Mesa below the water table (9):

$$M_S = 0.86 \log W + B, \quad \sigma = 0.09,$$

Yucca Flat below the water table (30):

$$M_S = 1.17 \log W + B - 0.93, \quad \sigma = 0.19,$$

Pahute Mesa above the water table (13):

$$M_S = 1.21 \log W + B - 1.09, \quad \sigma = 0.05,$$

Yucca Flat above the water table (15):

$$M_S = 0.78 \log W + B - 0.82, \quad \sigma = 0.27,$$

Rainier Mesa. tunnel shots only (10)

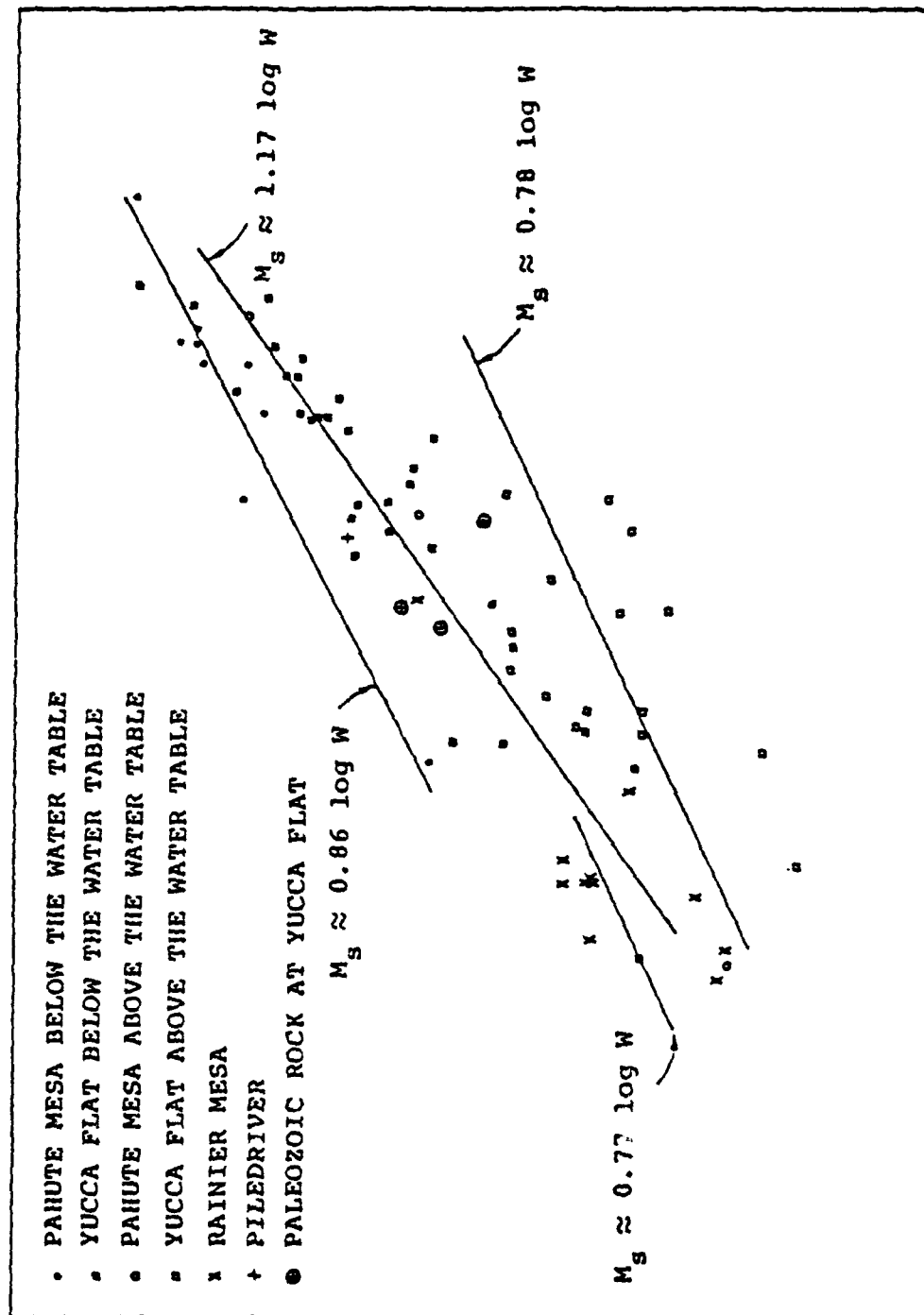
$$M_S = 0.77 \log W + B - 0.41, \quad \sigma = 0.19.$$

The  $M_S$  data together with the best fitting lines are plotted in Figure 3.1. As expected from the large  $\sigma$  values for some populations, there is considerable scatter in the data.

There are seven Pahute Mesa and eleven Yucca Flat events for which the Airy phase  $M_S$  estimates can be compared to the teleseismic  $M_S$  of Eisenhower (1976). These are plotted in Figure 3.2. To give some idea of the scale, the standard deviation of the mean residual between the two  $M_S$  measurements is less than 0.10  $M_S$  units. This indicates that the Airy phase measurements from these two stations give  $M_S$  measurements nearly the same as the teleseismic  $M_S$  from many stations compiled by Eisenhower.

The data plotted in Figure 3.1 indicate that the slope of  $M_S$  versus  $\log W$  is not much different from unity. Then one way to indicate the relative coupling in different areas is to compute  $M_S - \log W$  for each event. The mean values of this quantity are shown in Figure 3.3 for each population.

We see that the  $M_S$  and Airy phase data agree that the  $M_S$  coupling is about 0.1 - 0.3 units higher for events below the water table at Pahute Mesa than for comparable events at Yucca Flat. There are only a few events above the water table at Pahute Mesa, but they clearly couple more weakly into  $M_S$  than those in saturated materials. The lowest  $M_S$  events are those in dry tuffs at Yucca Flat. The scatter is quite large for these low yield events, but  $M_S - \log W$  is 0.57 lower, on the average, than for the saturated events at Yucca Flat. This difference is much larger than the standard deviation of the data. The saturated tuff explosions in the tunnel beds at Rainier Mesa seem to couple about the same as the saturated tuff events identified as being in Paleozoic rock at Yucca Flat. Since these events were detonated close to the tuff-Paleozoic interface, the identification of these events as being in Paleozoic rock is somewhat ambiguous, and we are probably not seeing the true differences between events in the two source media. Finally, the PILEDRIVER event seems to couple like the highest coupling population, the Pahute Mesa events below the static water table.



YIELD, W (kt)

Figure 3.1. The  $M_s$  values from the WSSN stations ALQ and TUC are plotted versus explosion yield. The explosions are divided into different populations according to the gross properties of the emplacement media.

$M_s$



Figure 3.2. The  $M_s$  estimates from ALQ and TUC are compared to those from Eisenhauer (1976) for eighteen common events. A line of unit slope is shown for convenience. The standard deviation of the mean residual between these two  $M_s$  measures is 0.10  $M_s$  units.

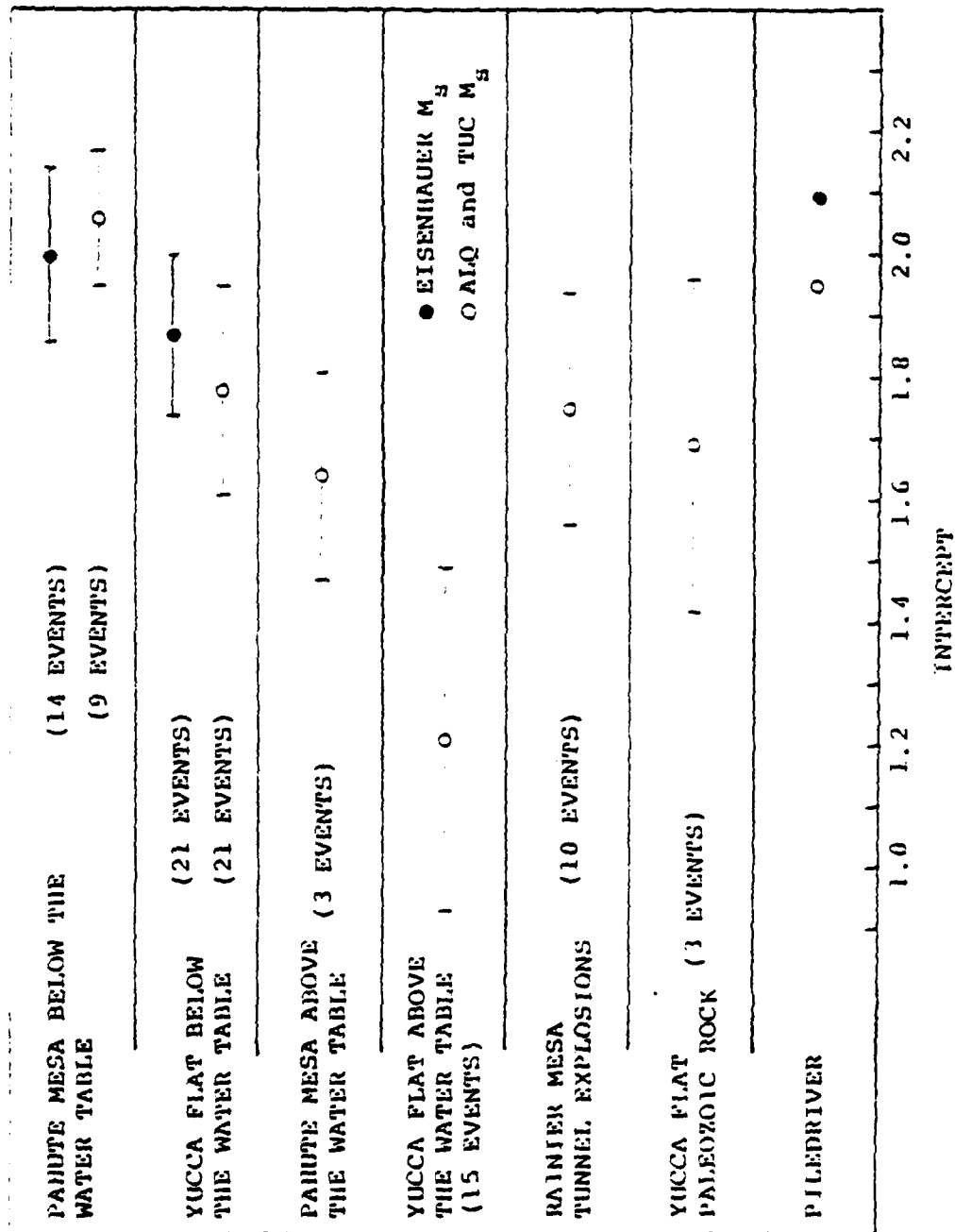


Figure 3.3. The mean values of  $M - \log W$  for events in a limited yield range in each of the testing areas are depicted by a bar graph. For each data set the lines represent the mean  $\pm$  one standard deviation.

In summary, we have delineated the coupling differences between events in different areas at NTS. The Airy phase amplitudes at ALQ and TUC show about the same variation with yield and source material as the  $M_s$  from a much larger data base. The question is, do we understand why the surface wave amplitudes vary from one test area to another? This question motivates the work discussed in the next several sections.

### 3.3 EXPLOSION RDP AMPLITUDES FROM RAYLEIGH WAVES

#### 3.3.1 Introduction

The most obvious way to think about using surface waves to determine explosion yields is in terms of the  $M_s$ -yield relationship. But  $M_s$  is an average of values from many single station recordings, so a close look at the single station behavior of the Rayleigh wave amplitude should enhance our understanding of what is controlling the  $M_s$ . In two reports (Bache, Rodi and Harkrider, (1978), and Bache, Rodi and Masso, (1978), we looked closely at the ALQ and TUC recordings of NTS explosions that we discussed in the last section.

The simplest model for the explosion source is the reduced displacement potential (RDP) and a great deal of work has been done to interpret the data in terms of this spherically symmetric source representation. If the RDP is viewed as a first-order model for the source, plane-layered structures provide comparable first-order models for the travel path. In the work described in the two 1978 reports, the observed seismograms were interpreted using these fairly simple models. In this section we will summarize that work.

#### 3.3.2 Path Models Compatible with Surface Wave Observations

To deduce the source amplitude from far-field seismic recordings, it is necessary to correct for the effect of the path. Bache, Rodi and Harkrider (1978) constructed path models for the NTS-ALQ and NTS-TUC paths from observed surface waves at the two stations. The main elements of that study were:

- Rayleigh wave recordings of NTS explosions were collected from the WWSSN stations ALQ and TUC. The data were divided according to test site. It was observed that recordings from a single test site (e.g., Pahute Mesa) had very similar waveforms.
- Representative recordings were digitized from three sites; Climax Stock, Yucca Flat and Pahute Mesa.
- The digitized data were processed by the S<sup>3</sup> MARS program and phase and group velocity curves were derived for the two paths, NTS-TUC and NTS-ALQ.
- Using generalized linear inversion techniques, plane layered earth models were found that fit the data. These models are compatible with other geophysical information about these paths.
- A Q model was constructed from western United States attenuation data collected by Mitchell (1975).
- Synthetic seismograms were computed with a simple reduced displacement potential (RDP) source. These seismograms are shown compared to typical observations in Figure 3.4.

This procedure ensures that the dispersion of the synthetic and observed seismograms be the same. However, the excellent waveform agreement indicates that the amplitude spectra are fit as well.

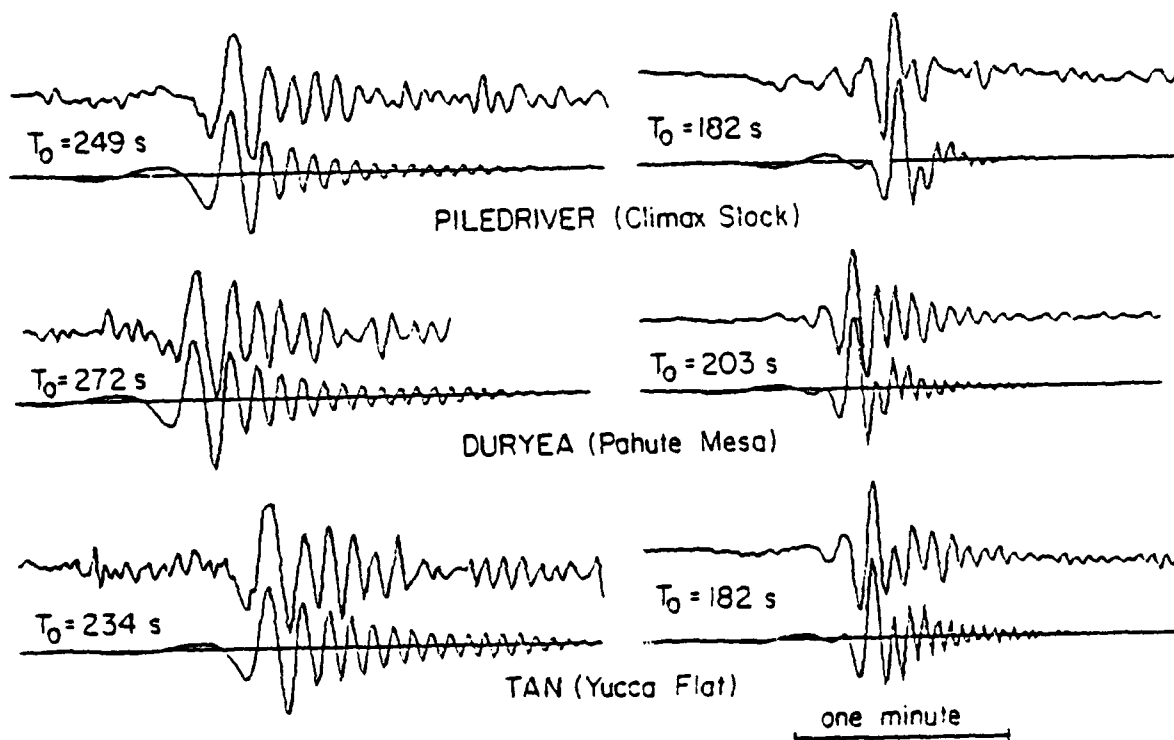


Figure 3.4. Theoretical and observed seismograms are compared at ALQ (left) and TUC for events in three test areas at NTS. A bar indicating one minute is shown. In each pair the observed (top) and theoretical records start at the same time with respect to the explosion detonation and this time is indicated as  $T_0$ .

### 3.3.3 Surface Wave Dependence on Source Material Properties

In computing the seismograms of Figure 3.4 there is one path model for NTS-TUC and one for NTS-ALO, but we must deal with the fact that the local material properties are different for the three test areas. This was handled by using a two path model with the local differences accounted for in the top two kilometers of the source region model. Transition between the two is accounted for by an approximate transmission coefficient,  $T(\omega)$ , based on results of McGarr (1969). The vertical Rayleigh wave is computed from

$$\hat{w}(r, \omega) = -4\pi\mu_s \hat{\psi}(\omega) \frac{K_{s1}}{c_1} A_{R1} T(\omega) H_0^{(2)}\left(\frac{\omega R}{c_2}\right) e^{-\gamma r} \frac{r}{a_e \sin \Delta}^{1/2},$$

where subscripts 1 and 2 indicate the source and path models.

An important question is, keeping all other factors fixed, how does Rayleigh wave amplitude scale with the source material properties? The  $\hat{\psi}(\omega)$  is the RDP source and is  $\psi_\infty$  at long period,  $\mu_s$  is the shear modulus at the source,  $K_s$  is the depth dependent eigenfunction for an explosion,  $c$  is phase velocity and  $A_R$  is depth-independent amplification.

The answer to the question is shown in a direct way in Figure 3.5. For source regions that are not too different (e.g., Pahute Mesa and Yucca Flat) we have

$$M_s \approx \log(\mu_s \psi_\infty).$$

However, if we compare the Climax Stock to the others, we see that the relationship has a strong frequency dependence and takes no simple form.

### 3.3.4 Inversion for the RDP Source Amplitude

We have pointed out that plane-layered earth models and an RDP source are adequate to give synthetic seismograms with waveforms

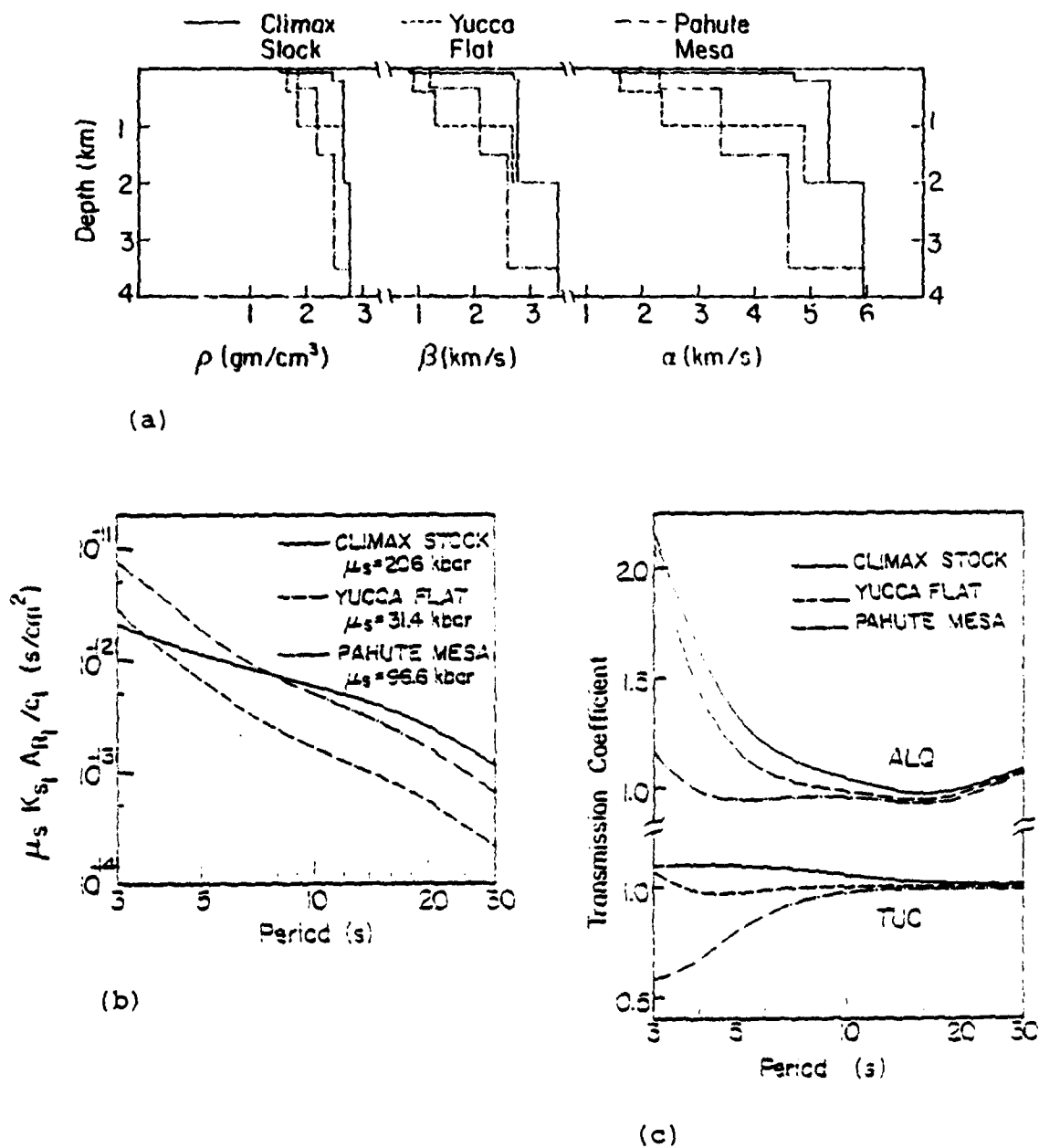


Figure 3.5. (a) The density, shear and compressional wave velocities are plotted versus depth for the three test area at NTS. (b) The source amplification factor is shown for the three source areas studied. (c) The transmission coefficient  $T(\omega)$  is plotted for the six source-path combinations studied.

that match the observations. Using this comparison, we inferred the  $\Psi_{\infty}$  required to match the observed amplitude. This work is described in an S<sup>3</sup> report by Bache, Rodi and Mason (1978)

The events considered were separated into the three populations and all were below the water table with yields between 40 and 200 KT. The inferred  $\Psi_{\infty}$  values are shown in Figure 3.6. We conclude that:

- For each station the  $\Psi_{\infty}$  (scaled to a common yield) was consistent within each population - the standard deviation was about 40 percent of the mean.
- The  $\Psi_{\infty}$  from one station (TUC) was consistently 50 percent larger than from the other.
- The  $\Psi_{\infty}$  values were consistent with those derived using other methods (close-in observations, teleseismic body and surface waves, finite difference source calculations).

These events do not span a wide yield or depth range. The only depth correction made was for the depth dependence of the eigenfunctions. This turns out to be:

Yucca Flat:	$\log A \approx 0.16 \log H,$
Pahute Mesa:	$\log A \approx 0.05 \log H.$

If  $H \approx W^{1/3}$ , and the source function scales with yield, this translates to an  $M_s - \log$  yield slope of 1.05 for Yucca Flat and 1.02 for Pahute Mesa.

We have not put forth an explanation for the relative amplitudes of explosions in the other classes listed in Figure 3.3. The events above the water table have generally lower  $\mu$  and  $\Psi_{\infty}$  than those below the water table, so the observed coupling of these

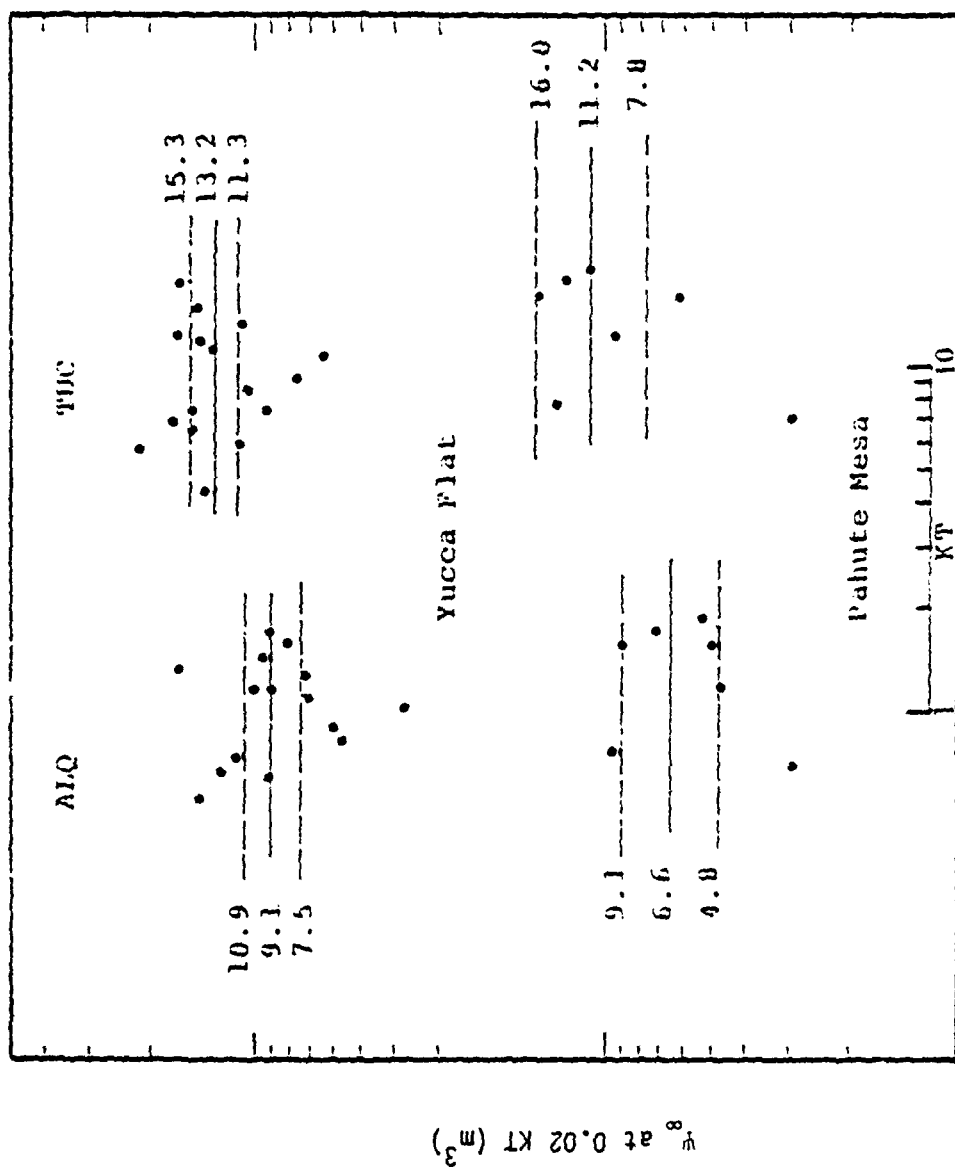


Figure 3.6. The  $\psi_{\infty}$  values (at 0.02 KT) are plotted versus explosion yield for the Yucca Flat and Pahute Mesa events. The plot is log-log and the mean and 95 percent confidence limits on the mean are shown. One decade of yield is shown for reference.

events is as expected. The Rainier Mesa events have  $\mu$  close to that for Yucca Flat saturated events, (Bache, et al., 1975), which explains their coupling.

### 3.4 HIGHER ORDER SOURCE EFFECTS

Many potentially important source effects are two- or three-dimensional and thus cannot be represented by an RDP source. These higher order effects include the depth-dependence of overburden pressure, nonuniform source region properties, nonlinear interaction with the free surface, and release of stored strain energy near the source. Some of these effects can be approximated with elastic models to estimate their influence. Results from these kinds of approximations are summarized in this section.

Bache, Rodi and Mason (1978) used elastic models to attempt to delineate the influence of higher order effects including: double-couple generation by tectonic release, spallation, attenuation of upgoing waves by spallation and/or scattering in the near surface materials. This leads to many questions about the physics of the source. These questions can probably only be resolved by resorting to multidimensional calculations like those we describe in Section IV.

Empirical estimates for spall closure (e.g., Viacelli, 1973; Sobel, 1978) suggest that the generated Rayleigh waves might be nearly the same size as those from the explosion itself. However, the spall induced Rayleigh wave is 90 degrees out of phase with that from the explosion and makes an unimportant contribution to the ALQ and TUC records for reasonable assumptions about its amplitude. It is not clear whether this result can be generalized to allow the spall effect to be ignored.

A potentially important spall related phenomenon is the attenuation of upgoing waves from the source during the spall process. This is explored by Bache, Rodi and Mason, but conclusions cannot be confidently drawn without better understanding the physics of the process. Again, two-dimensional calculations like those described in Section IV are needed to improve our understanding.

To explore the effects of a double-couple component, Bache, Rodi and Mason (1978) used the inferred double-couple solutions of Toksoz and Kehrner (1972). In this form the double-couple has almost no effect on the waveform, but simply scales the amplitude. If the events studied by Toksöz and Kehrner are typical, some 15 or 20 percent of the discrepancy between the ALQ and TUC inferred RDP amplitudes is due to the double-couple. For PILEDRIVER, their inferred double-couple dominates the solution. However, their orientation does not explain the ALQ-TUC amplitude discrepancy, but actually increases it. We will discuss the question of a superimposed double-couple in more detail in the next section.

### 3.5 SURFACE WAVE RADIATION PATTERNS

#### 3.5.1 Introduction

A serious problem always cited to discourage too much reliance on surface waves as a yield indicator is the observed fact that many events are characterized by strong surface wave radiation patterns. The conventional wisdom is that superimposed on the explosion source is a double-couple aligned with the local stress field. From a theoretical point-of-view, one should be able to deduce the orientation and moment of this double-couple from the radiated Love and Rayleigh waves and correct the data for this effect. This was the approach followed by Bache, Rodi and Mason (1978), described in the preceding section. They used the double-couple solutions obtained by Toksoz and Kehrner (1972) for a fairly large number of underground explosions.

Toksöz and Kehrner introduced the restrictive assumptions that the double-couple source had the same location and time function as the explosion and was oriented as a vertical strike-slip fault. If enough good data were available, these assumptions could be relaxed. For example, Rivers and von Seggern (1979) have inverted

for the best moment tensor fit to the PILEDRIVER data using the moment tensor inversion scheme of Mendiguren (1977). Of course, any inversion scheme is limited by the accuracy of the path corrections used.

How well does the explosion plus double-couple model fit the data? The strike-slip double-couple used in the inversions of Toksöz and Kehrner does not give a particularly good fit. Rivers and von Seggern (1979) seem to fit the PILEDRIVER data quite well, but with a model for which the physical interpretation is not entirely clear. The orientation is that of a reverse fault and both the explosion and double-couple are at a depth of 2.5 kilometers.

It does seem clear that the explosion plus double-couple model qualitatively explains the long period data. Perhaps it also gives a quantitative explanation that can be used to correct individual station amplitudes. But more detailed work is necessary to prove this concept. We have looked at two very similar events, MIGHTY EPIC and DIABLO HAWK, in some detail, and the results illustrate that the data are not easily explained, in more than a qualitative way, by superimposing a double-couple on the explosion.

### 3.5.2 Analysis of Regional Motions from MIGHTY EPIC and DIABLO HAWK

Bache, Farrell and Lambert (1979) describe an analysis of the regional ground motions of the Rainier Mesa explosions DIABLO HAWK and MIGHTY EPIC. These were very similar events of fairly low yield. The recording stations, seven for MIGHTY EPIC and ten for DIABLO HAWK, were broad-band, three-component digitally recorded stations operated by Lawrence Livermore Laboratory, Sandia Laboratories and Systems, Science and Software (S<sup>3</sup>). The distances were 131 to 368 kilometers.

The objective of the experiment was to infer the size and orientation of the double-couple component associated with these events. First, the data were processed to determine the following:

- The coherence between the same station recordings of the two events is very high. The sources were, therefore, nearly identical, the difference being a scale factor, which may be azimuthally dependent.
- The coherence between different components is low. This seems to indicate that the horizontal component waves emanate from the vicinity of the source.
- The data were filtered with a four to eight second band pass filter and with MARS to identify the fundamental mode Love and Rayleigh waves with a period near six seconds. All indications are that these modes were successfully isolated.

The best fitting explosion RDP plus double-couple was determined by fitting the LR, LQ and LQ/LR data. The double-couple was assumed to be a vertical strike-slip. The best fitting solutions for DIABLO HAWK are shown in Figures 3.7, 3.8 and 3.9. The analogous solutions for MIGHTY EPIC are shown in Figures 3.10 and 3.11.

The inferred RDP, ( $\Psi_{\infty}$ ) is within the range of expected values for such events. This indicates that the amplification effects of the path are about right at these regional distances. The fit to the Love waves is not very good. In fact, the data would be fit nearly as well with a circle!

There is another interesting aspect of these data. The DIABLO HAWK/MIGHTY EPIC ratio is about 0.9 at high frequencies and 0.6 at low frequencies. This is true for nearly all components at all stations. The frequency domain ratios can also be seen in time domain measurements of  $P_n$  (ratio of 0.9) and long period Love and Rayleigh waves (ratio of 0.6). It seems that the total (explosion plus double-couple), source level is larger at long periods for DIABLO HAWK. There is no easy way to explain this in the context of the simple theory used.

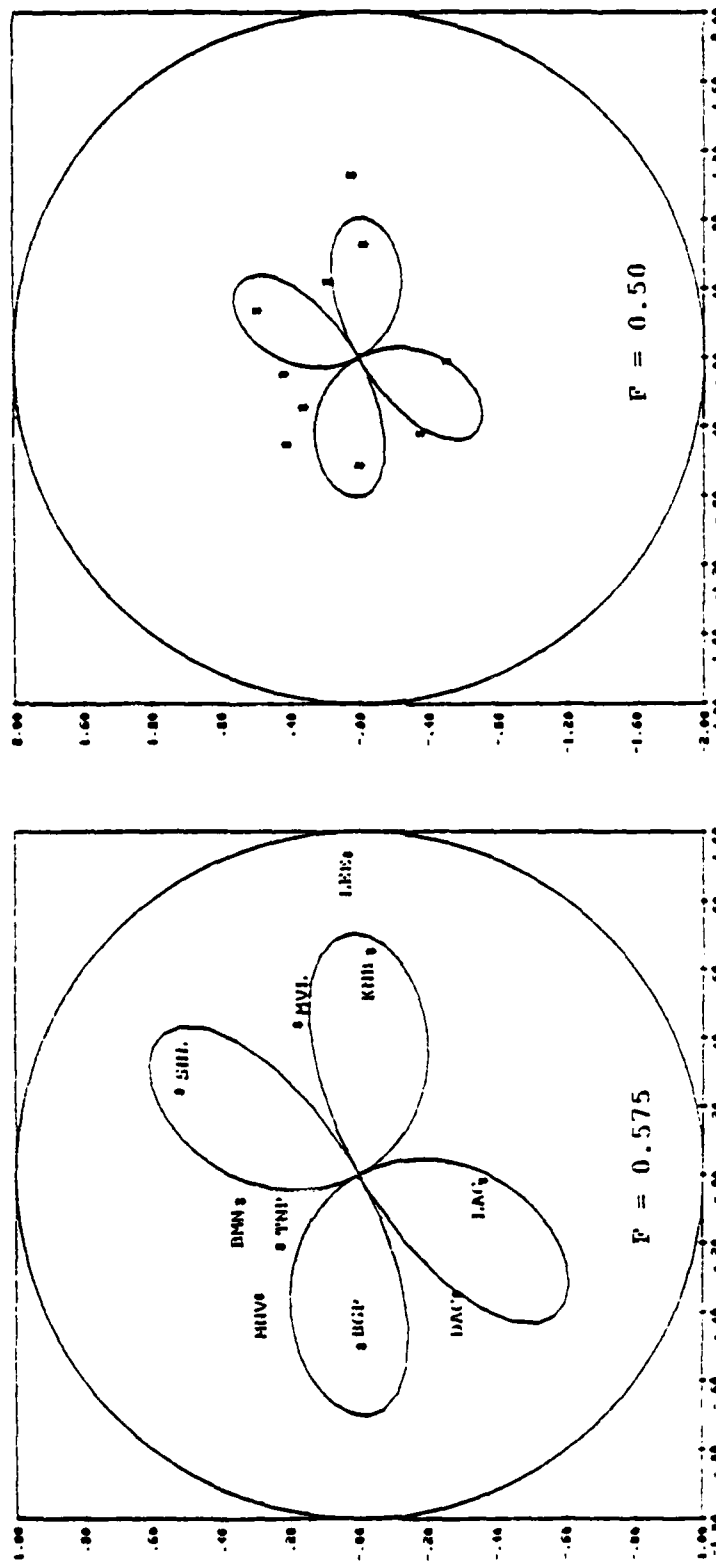


Figure 3.7. Comparison of theoretical LQ/LR radiation patterns ( $\delta = 90$ ,  $\lambda = 0$ , strike = N16 E) to the observed data with and without path corrections.

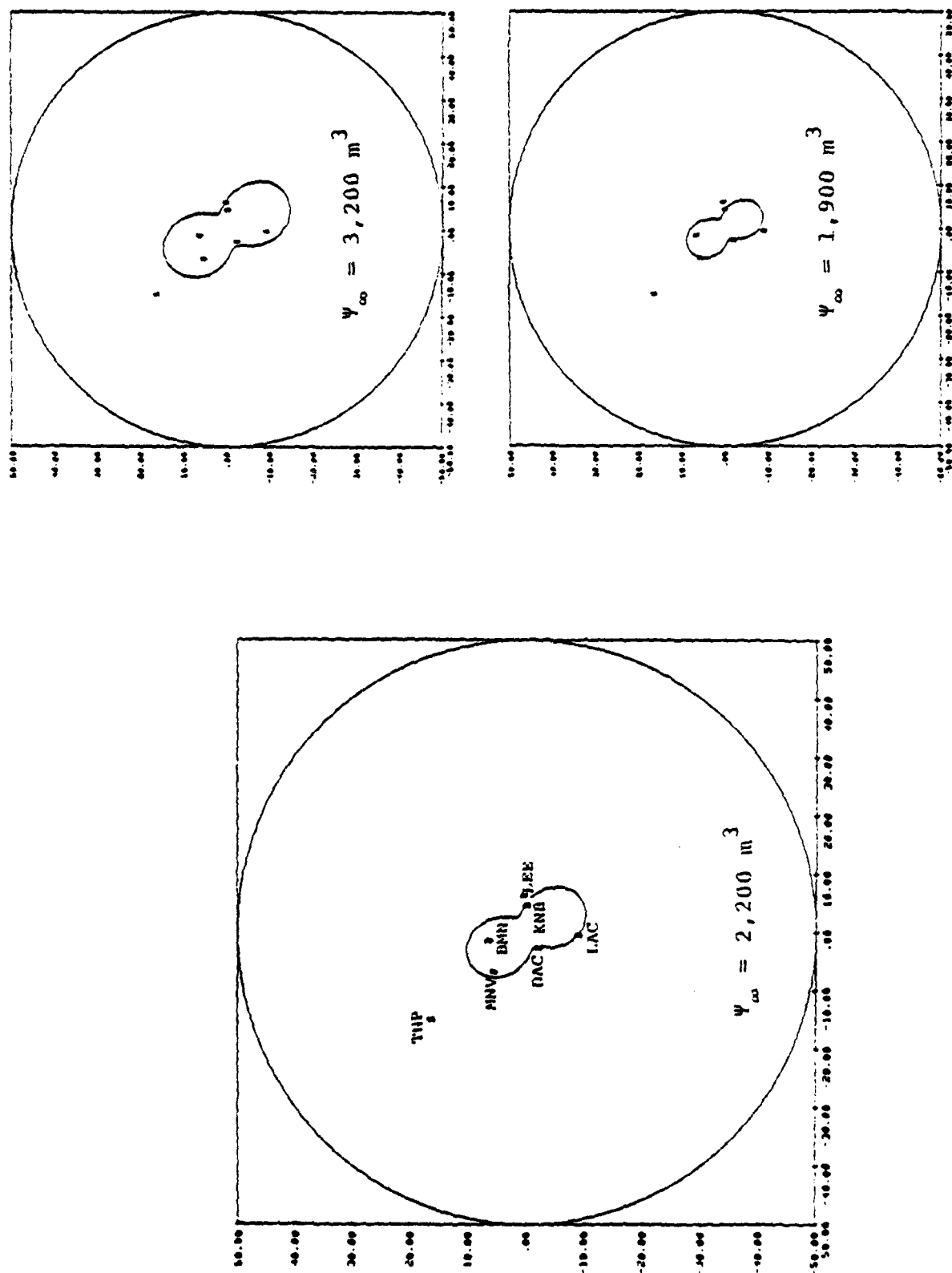


Figure 3.8. Theoretical Rayleigh wave radiation patterns are compared to the DIABLO HAWK observations normalized to a range of 250 km. The theoretical solution has  $\delta = 90^\circ$ ,  $\lambda = 0$ , strike = N16 E,  $F = 0.575$ ,  $\mu_s = 40 \text{ kbar}$  and three values of  $\psi_{\infty}$ .

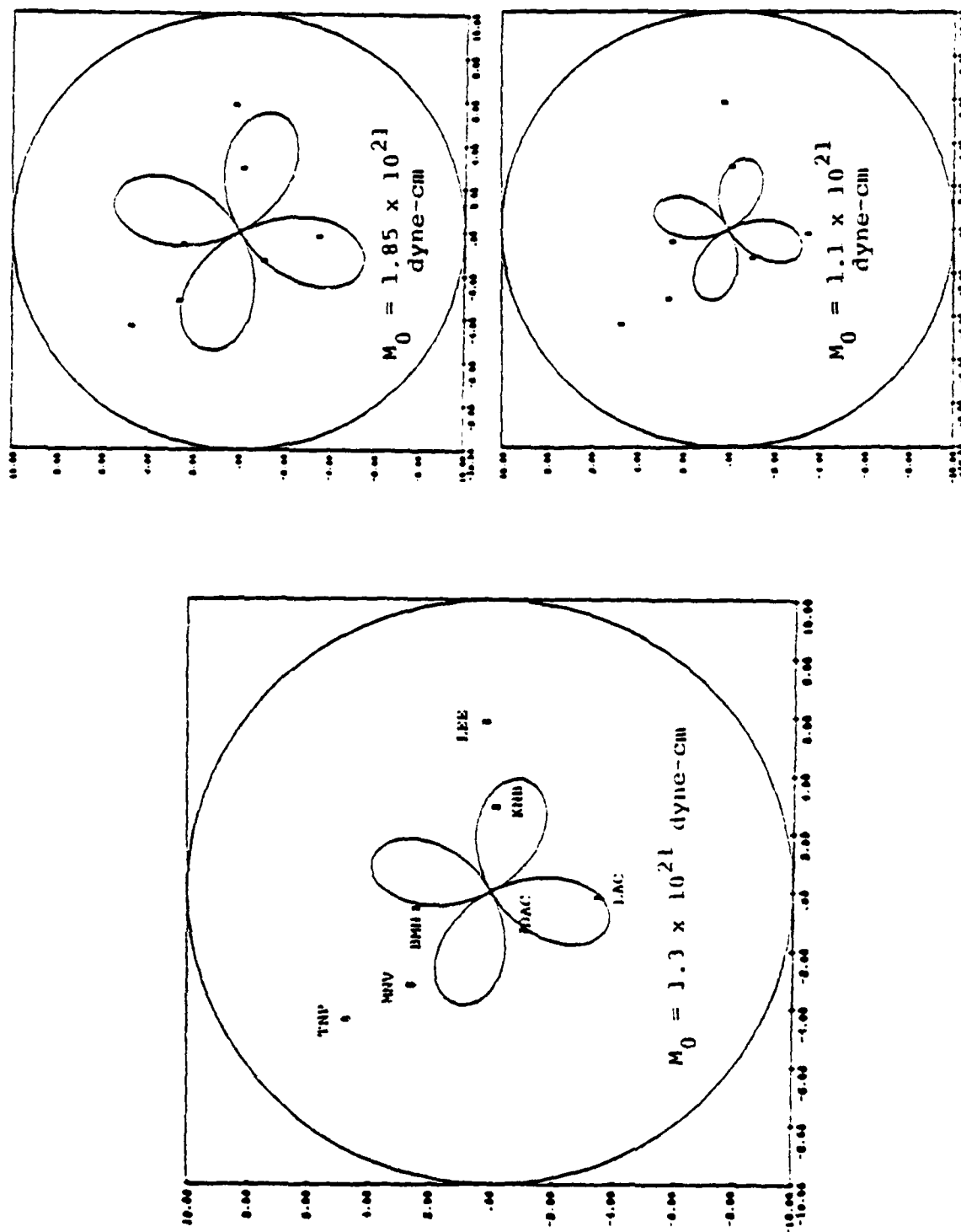


Figure 3.9. Theoretical Love wave radiation patterns are compared to DIABLO HAWK observations normalized to 250 km. The theoretical solutions have  $\delta = 90$ ,  $\lambda = 0$ , strike = N16 E,  $F = 0.575$ ,  $\mu_s \approx 40$  kbar and three values of the moment,  $M_0$ .

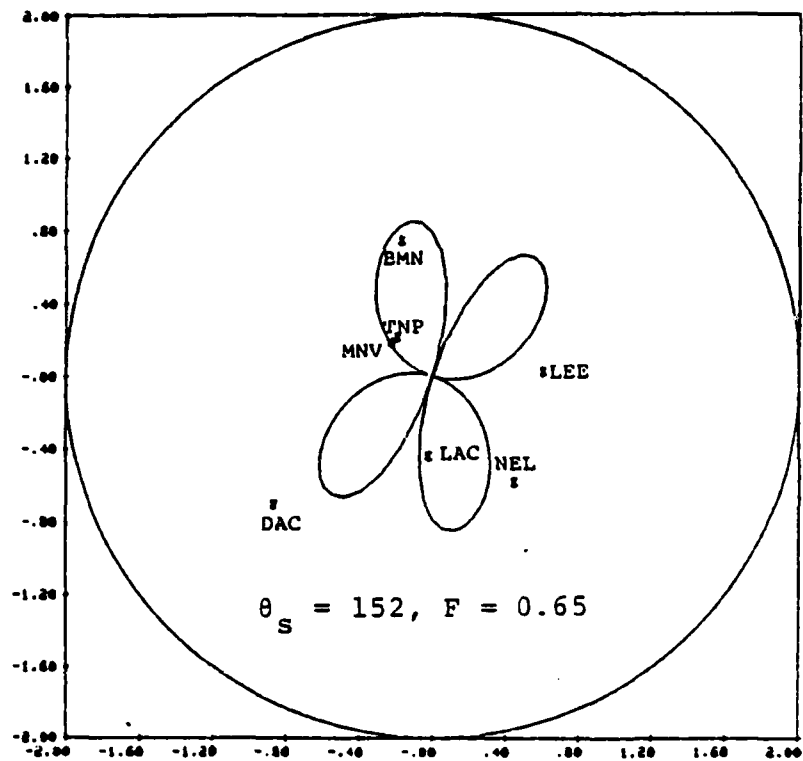


Figure 3.10. The fit to the MIGHTY EPIC LQ/LR data. We assume vertical strike-slip faulting.

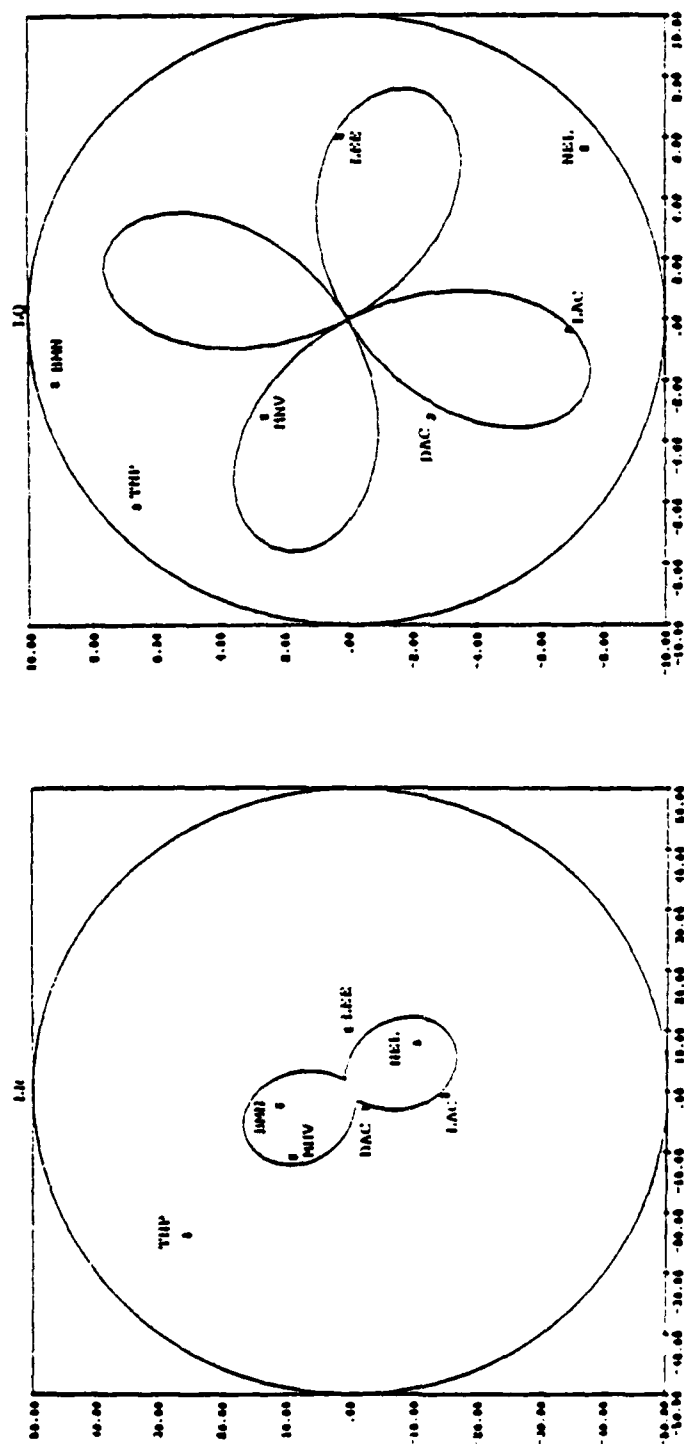


Figure 3.11. MIGHTY EPIC LR and LQ data compared to theoretical radiation patterns for  $\theta = 16$ ,  $\delta = 90$ ,  $\lambda = 0$ ,  $\psi_{\infty} = 3,200 \text{ m}^3$ ,  $F = 0.8$ ,  $M_0 = 2.6 \times 10^{21} \text{ dyne-cm}$ .

### 3.5.3 Discussion of the Radiation Pattern Data

We find that the long period radiation from MIGHTY EPIC is about twice as large as that from DIABLO HAWK on all three components at nearly every station, while the short period radiation is about the same. Also, no single double-couple source can provide a very good fit to the Love wave data (which are almost certainly true Love waves originating near the source, though the amplitudes may be contaminated by off-azimuth Rayleigh wave arrivals). The material properties for the two events are nearly identical, so spectral differences in the explosion source functions are unlikely. One hypothesis that will explain these data is that the MIGHTY EPIC event had much more block faulting which is not dominantly along one azimuth, but includes slip on faults at several azimuths. If the faulting is associated with tectonic strain release, the superimposed double-couple sources must have spectra that are substantially smaller at 1 Hz than at longer periods. Since the double-couple source dimensions must be quite small, this suggests that the block faulting must occur with extraordinarily slow (compared to earthquakes) rupture velocities, on the order of 100 m/sec.

An alternative model for the generation of shear waves that may help explain the observations is that there is a substantial amount of wave conversion near the source due to passive (i.e., releasing little or no stored strain energy) fault motions. In a recent paper Salvado and Minster (1980) have shown that this conversion can be large for faults that are weakly bonded and close to the source. However, this study was done for an idealized geometry, so quantitative estimations of the potential effect on the seismic radiation for actual events has not yet been done.

Part of the difficulty in explaining the radiation pattern with a model for tectonic strain release is that the models used are too simple. Stevens (1980) has shown that an unhomogeneous prestress field (including stress concentrations) leads to a radiation pattern that includes higher order terms than the double

couple. One consequence is the absence of nodes, which are also absent in the data. This is another more realistic effect which may help explain the observed complexity.

### 3.6 CONCLUSIONS

The capability exists to model surface waves from underground explosions in detail. The source may be of arbitrary complexity in plane layered earth models. In this section, we have only been discussing elastic point source models, but in the next section we will show that complex finite difference simulations of multidimensional explosion sources can also be used to model surface waves. An important question is how to account for changes in the local source material when the average path properties clearly remain the same. We have been using an approximate technique that seems to give reasonable results.

When we consider the source amplitudes inferred from ALQ and TUC data using these detailed modeling procedures, we conclude that:

- Even with the simplest source model (RDP), the inferred source amplitudes are reasonably consistent.
- For similar materials, Rayleigh wave amplitude is proportional to  $\mu\psi_{\infty}$ . For different materials (e.g., tuff and granite), the dependence on  $\mu$  is much weaker and varies with period.
- Empirical estimates for spall closure suggest that the generated Rayleigh waves might be nearly the same size as those from the explosion itself. However, spall closure appears to be unimportant for ALQ and TUC records.

Important questions that require further investigation include the following:

### Path Effects

- What are the effects of lateral heterogeneities and departure from plane horizontal layering? Are such effects responsible for the 50 percent amplitude difference from ALQ to TUC?
- Attenuation (Q) is not very well-known, though this is less important for surface waves than body waves.

### Source Effects

- How appropriate is the one-dimensional source representation? Known two- and three-dimensional effects include:
  1. Depth dependence of overburden pressure.
  2. Spallation and cracking to the surface.
  3. Block motion, induced fault motion, tectonic strain release.
- How are tangential (SH and Love) waves generated? Why are they generated at all azimuths? What parameters control their amplitude? How well does a single double-couple represent this perturbation on the source?
- How large is spill closure? How are the free surface reflected waves in the nonlinear environment different from those in the elastic approximation?
- The ALQ and TUC study raises the question, if stations at many azimuths were used, how much would the estimate vary? How much of the "source" radiation pattern is a path effect? How much of this path effect can be corrected by careful modeling?

Finally, we conclude that a great deal of progress has been made in understanding surface wave excitation by explosions. There are partial answers to all the questions listed above and the techniques are available to obtain more complete answers.

THIS PAGE LEFT BLANK

#### IV. THE CONTRIBUTION OF TWO-DIMENSIONAL SOURCE EFFECTS TO THE FAR-FIELD SEISMIC SIGNATURES OF UNDERGROUND NUCLEAR EXPLOSIONS

##### 4.1 INTRODUCTION

A recent report by Bache, Barker, Rimer and Cherry (1980), which has the same title as this section, includes an analysis of the seismic waves from a series of axisymmetric calculations of explosions in granite. The abstract of that report is reprinted below:

Two-dimensional calculations of underground explosions are able to model nonlinear interaction with the free surface (including spallation) and the depth dependence of overburden pressure and material properties, as well as the complex constitutive behavior of geologic materials which has been extensively studied with one-dimensional (spherically symmetric) calculations. In this study, eleven axisymmetric calculations of explosions in granite are analyzed to determine the two-dimensional effects on the far-field body and surface waves and on the magnitudes  $m_b$  and  $M_s$ . Seven of these are hypothetical 150 KT explosions at depths from 159 to 1000 meters calculated by Applied Theory, Inc. (ATI). These show depth effects that are different, though not strikingly so, from those calculated with one-dimensional source models. The other four calculations were done by Systems, Science and Software (S-Cubed). The first was for a specific event (PILEDRIVER), and the depth and yield were varied for the other three. The near- and far-field data for PILED RIVER were matched rather well, except that the spallation was too large in the calculation.

Synthetic body and surface waves from the S-Cubed two-dimensional sources are compared to those from analogous one-dimensional sources to isolate the two-dimensional effects. These are not important for the deep events or for the first arriving P wave from the shallow events. They do strongly enhance the surface wave amplitudes (by a factor of two or three) for the two shallow calculations, including that for PILED RIVER, and reduce the  $m_b$  by 0.1 - 0.2 units. The  $m_b$  effects can clearly be attributed to spallation and the accompanying reduction of the pP amplitude,

which are overpredicted by the calculations. The  $M_s$  enhancement must be due to the same causes, though they are not easily isolated.

The first section of the Bache, et al. (1980), report is the "Introduction and Summary," which includes the important conclusions. This material is reproduced in the following subsections.

#### 4.2 BACKGROUND

To successfully monitor a test ban treaty prohibiting or limiting underground nuclear explosions, it is necessary to understand the seismic signatures of these events. An important part of the research effort to improve this understanding has been the development and application of deterministic methods to compute the seismic wave signatures of nuclear explosions. In nearly all of this work the source is assumed to be spherically symmetric and the earth is assumed to be plane-layered. Theoretical seismograms can then be computed with widely available methods and compared to observations. This procedure has been quite successful and most of the important controlling parameters have been identified and their effects have been quantified to some degree. However, many important issues remain unresolved.

Most of the important questions that remain regarding the generation of seismic waves by underground explosions are associated with multi-dimensional effects. For example, there is not yet a clear understanding of the effect on the seismic radiation of nearby interfaces, the free surface (allowing spallation), the overburden pressure, nonhydrostatic prestress, and zones of weakness in the near source environment. The one-dimensional calculations now incorporate detailed constitutive models that include realistic models for pore collapse, effective stress, yielding, and cracking due to shear and tension failure. These constitutive models, have been generalized to two-dimensions for the axisymmetric finite difference source calculations analyzed in this report. While they do not include all the multi-dimensional effects we have listed,

they do include some of the most important, and so represent a significant step forward in the development of realistic theoretical simulations of the seismic waves from underground explosions.

#### 4.3 AXISYMMETRIC CALCULATIONS OF NUCLEAR EXPLOSIONS

In this report we present a detailed analysis of the seismic waves from eleven two-dimensional finite difference calculations of underground nuclear explosions in granite. Seven of these calculations were done by J. Trulio and N. Perl of Applied Theory, Inc. (ATI) and four by N. Rimer and J. T. Cherry of Systems, Science and Software (S-Cubed). They share the same axisymmetric geometry, though the details are different.

The two-dimensional, axisymmetric explosion calculations include the presence of a free surface, the dependence of overburden pressure on depth and, for the S-Cubed calculations, some dependence of material properties on depth. These are probably the most important higher order corrections to the one-dimensional models. The depth-dependence of overburden pressure is a property of all test sites. Further, our understanding of geologic structures is normally based on plane-layered models. Therefore, axisymmetry is a natural geometry, and specification of the geometry and material properties in two-dimensions is more straightforward than characterizing the entire near-source environment by a heterogeneous material.

The most important two-dimensional effects are associated with the nonlinear interaction of the stress waves with the free surface. Surface spallation is an obvious, even dominant, phenomenon observed in the near-field, yet it has never been included in seismic wave propagation studies in a very satisfactory way. Perhaps more important, there is ample evidence that the free surface phase pP is more complex than predicted by elastic theory with spherically symmetric sources, but, again, this remains mostly in the realm of speculation. With the axisymmetric calculations, we are able to study these important effects.

The objectives of the parameter variations in the ATI and S-Cubed suites of calculations are somewhat different. The ATI calculations were all done at the same yield, 150 kt, in a hypothetical granite halfspace. Only the depth was varied, from 159 to 1000 meters. The philosophy of the S-Cubed calculations was to begin by modeling a specific event, PILEDRIVER, at the Nevada Test Site. The constitutive model and source geology (three layers) were chosen for this event. The computed and observed ground motions were compared at some twenty-five near-field gauge locations. The comparison was quite good, except that the calculation overpredicted the amount of cracking (spallation) near the surface. This turns out to be important when comparing synthetic and observed short period data.

The other three S-Cubed source calculations were the same, except the depth and yield were varied from the values appropriate for PILEDRIVER. The four calculations were as follows:

<u>Depth (Meters)</u>	<u>Yield (Kt)</u>
463	60 (PILEDRIVER)
1000	150
1000	20
400	20

#### 4.4 OUTLINE OF THE ANALYSIS

The analyses of the seven ATI and four S-Cubed calculations are described separately, but follow parallel lines. First, we describe the near-field ground motions predicted by the calculations in some detail. Then we present theoretical seismograms for these calculations and analyze their implications. This outline is apparent in the section headings listed below:

- Section II: ATI Granite Calculations
- Section III:  $M_S$  and  $m_b$  Estimates for ATI Granite Calculations
- Section IV: S-Cubed Granite Calculations
- Section V:  $M_S$  and  $m_b$  Estimates for S-Cubed Granite Calculations
- Section VI: Comparison of Predicted and Observed Seismograms for PILEDRIVER
- Section VII: Comparative Analysis of ATI and S-Cubed Granite Calculations.

A key step in this study is the linkage between the near-field ground motions computed by the finite difference programs and the analytical techniques used to propagate seismic waves in realistic earth models. A rigorous method for accomplishing this linkage is described in Appendix A, "Synthetic Seismograms from Complex Source Calculations." The details and examples presented in this appendix are mostly for the calculation of the normal mode (Rayleigh waves) displacements in a plane-layered earth model, but ray theory methods for propagating body waves can be used within the same theoretical framework.

To compute synthetic seismograms at large distances for the finite difference source calculations, it is necessary to monitor the tractions and displacements on some (hypothetical) surface which entirely encloses the region of nonlinear material response. Our discussion of the source calculations in Sections II and IV is concerned with the characteristics of the monitored ground motions on this elastic surface.

An important constraint on the numerical results is the requirement, based on conservation of momentum, that the total downward force and impulse (on the surface enclosing the source region)

vanish at late time. It turns out (Appendix A) that the inevitable numerical errors that cause deviation from this requirement can dominate the solution at long periods. Therefore, a major theme in Sections II and IV is the application of a "correction" to adjust the computed vertical force and impulse to zero at the last time step.

The synthetic seismogram results are presented in Sections III and V. The vertical force "correction" is also an issue in these sections, because it would be unsatisfactory for an ad hoc correction, which is what we apply, to dominate the answer. Our conclusion is that the vertical force terms, after correction, do not play an important role. All of the solution checks we are able to make indicate that the body and surface wave synthetic seismograms accurately represent the seismic waves generated by these theoretical sources.

The synthetic seismogram analyses in Sections III and V are focussed on comparing the seismic waves from the two-dimensional sources with those from analogous one-dimensional, reduced displacement potential (RDP) sources. For the S-Cubed calculations, we are able to compare to the RDP source computed with the same constitutive model in spherical symmetry. No such one-dimensional calculation was available for the ATI granite, so we compare to the RDP predicted by the semi-empirical model of Mueller and Murphy (1971).

Most of the calculations are for hypothetical events, so direct comparison with observed seismograms is only possible for the PILEDRIVER calculation done by S-Cubed. This comparison is made in Section VI. Finally, in Section VII, the results of all eleven calculations are plotted together for direct comparison.

#### 4.5 CONCLUSIONS

This study is primarily an investigation of the influence of burial depth on the seismic signals from underground explosions. For the most part, the results are interesting, but not terribly

exciting, because they are pretty much in accord with our expectations. The key exception is the surface wave results for the S-Cubed calculations.

The most important result of this study is that the S-Cubed calculations show  $M_s$  to be a strong function of depth. The shallow S-Cubed calculations have surface wave amplitudes that are a factor of two or three larger than those from a comparable one-dimensional source calculation. This effect is probably exaggerated because the free surface interaction effects are too large in the S-Cubed calculations, but would remain important even if the near surface material were strengthened. On the other hand, the ATI calculations show no strong dependence of  $M_s$  on depth, even though the shallow ATI sources cratered. We do not know why the two sets of calculations give such different results.

The important conclusions are listed at the end of several sections of the report. Summaries for the ATI and S-Cubed calculations are given separately in Sections 3.7 and 5.10. Our conclusions about the comparison of synthetic and observed seismograms are listed in Section 6.4, and all of Section VII should be read as a summary.

The main results are listed below:

#### ATI Calculations

- Neither  $m_b$  nor  $M_s$  are strongly dependent on depth. The most effect was on  $M_s$  at shallow depths.
- Compared to the Mueller/Murphy RDP source, the depth dependence in both amplitude and corner frequency is less for the ATI sources.
- The pP phase appears to be smaller than expected from elastic theory.

### S-Cubed Calculations

- Two-dimensional effects are not very important for the two deep explosions (20 kt and 150 kt at 1000 meters). Both  $m_b$  and  $M_s$  are little different from the values estimated from an RDP source computed with the same constitutive model at the same depth.\* This is true even though considerable cracking and spallation occur in the two-dimensional calculations.
- For body waves the first arriving P wave is essentially the same for one- and two-dimensional sources.\*
- The two-dimensional effects enhance the surface wave amplitudes for the shallow events (60 kt at 463 meters and 20 kt at 400 meters) by a factor of two or three. We must qualify this by pointing out that these shallow calculations have very strong surface interaction effects. Comparison with PILEDRIVER data indicates that the free surface interaction is overpredicted, at least for that event. Less free surface interaction would presumably give less enhancement of the surface wave amplitudes.
- For the shallow events, the  $m_b$  is different than predicted with an RDP source, though by less than 0.2 units.
- Analysis of the spectra show that in no case is pP a spectral shadow of P, as it is for an RDP source and elastic propagation.

\* These results are essentially tests of the entire computational procedure. It is gratifying that these two very different and complex procedures arrive at the same results.

- Phases that seem to be associated with spall closure can be seen on the shallow source body wave records. However, they are not easily associated with identifiable crack closure patterns in the source calculation.

The comparison of observed and calculated body and surface waves for PILEDRIIVER in Section VI leads to the conclusion that the two are in rather good agreement. This conclusion is subject to the qualifications one often faces in this kind of comparison. For the surface waves, it is the need to account for the non-axisymmetric component, usually attributed to tectonic stress release. Adding a recent estimate for this component by Rivers and von Seggern (1979) to our solution, we get good agreement with the data.

For body waves the comparison is complicated by the apparent presence of strong azimuthal effects in the radiated short period energy (Hadley and Hart, 1979). However, our conclusion is that the computed PILEDRIIVER source (in one- or two-dimensions) has about the right direct P amplitude. However, the two-dimensional source calculation appears to include too much non-linear interaction with the free surface. The later portion of the P waveform does not match the data, apparently because  $pP$  is too greatly suppressed and because the seismic energy from spall closure is too large or is timed incorrectly. This "overprediction" of surface interaction effects is expected since comparison of theoretical and observed near-field motions and plots of the cracking near the source indicate that there was too much spallation in the calculation.

All the theoretical  $M_s$  and  $m_b$  values are plotted together in Section VII. They are shown versus source depth and versus yield, including the observed values for HARDHAT, SHOAL and PILEDRIIVER. The most dramatic difference between the ATI and S-Cubed calculations is the strong dependence of  $M_s$  on depth predicted by S-Cubed, but not by ATI sources. This must be a reflection of the different constitutive models used.

The constitutive models used by S-Cubed (in spherically symmetric source calculations) lead to RDP source functions that are strongly peaked, with the value near 1 Hz a factor of five or more larger than the value at long periods. The peaking is due to the incorporation of an effective stress law and the choice of unconfined compressive strength (0.75 kbar), based on laboratory data for fractured granite and results of comparison with near-field ground motion observations (Rimer, personal communication).

While we do not have RDP source functions for the ATI granite, comparison of  $M_s$  and  $m_b$  for the ATI two-dimensional calculations indicates that the RDP peaking is probably less than a factor of two. Due primarily to this difference, the  $m_b$  for the S-Cubed calculations is about 0.5 units higher than that for ATI calculations of the same yield. The ATI  $M_s$  values fall between those for the shallow and deep S-Cubed calculations.

## V. THREE-DIMENSIONAL EARTHQUAKE MODELING INCLUDING NONLINEAR RUPTURE DYNAMICS

We are using a three-dimensional finite difference method to model those aspects of earthquake dynamics believed to be important for predicting the teleseismic signal. The calculations have simulated inelastic response of the fault zone through nonlinear boundary conditions on the fault plane. The numerical method admits more general nonlinear material behavior, which is being incorporated as required.

Our initial numerical simulations were for a simple, constant rupture velocity, constant stress-drop earthquake model. These results show a significant influence of fault width on the slip function. For points on the fault which are more than a fault width away from the focus, the slip function is spatially quite uniform. The static slip is given by  $\Delta\sigma w / \rho\beta^2$ , in agreement with estimates based on elastostatic solutions. The numerical simulations predict a rise time of  $w/2\beta$  and peak slip velocity of  $\sqrt{2fw/\beta} \Delta\sigma / \rho\beta$ . In these expressions,  $w$  is the fault width,  $\Delta\sigma$  the stress-drop,  $f$  the maximum frequency,  $\beta$  the shear speed, and  $\rho$  the density.

Careful studies of the broad-band character of earthquake teleseismic signatures indicate that the relative excitation of long- and short-period waves is inconsistent with predictions from the simple model. In addition, a few isolated, severe stopping phases dominate near-field accelerograms synthesized from the simple model, in conflict with strong motion data. More complex rupture physics is required to explain the discrepancies between the model predictions and teleseismic and strong motion observations. In particular, a better physical description of the cessation of rupture growth appears necessary.

A displacement-weakening constitutive model, described in Figure 5.1, has been applied to simulate spontaneous rupture in the presence of both uniform and heterogeneous prestress. In this model of failure, the shear strength of the fault zone is assumed to be a

decreasing function of its deformation; energy is dissipated during rupture extension and shear stress is bounded on the fault edges. When rupture initiates in a limited region of high stress (Figure 5.2a), the model leads to spontaneous propagation, deceleration, and stopping of faulting. Figure 5.3 shows the evolution of the rupture front in this case, as well as the far-field P and S wave displacement spectra and the corresponding displacement, velocity, and acceleration pulses. In the presence of multiple high-stress regions (Figure 5.2b), each isolated stress concentration behaves roughly as an independent event. As shown in Figure 5.4, rupture velocity becomes quite irregular, and is strongly coupled to peak velocity of slip on the fault surface. Figure 5.5 shows the irregular rupture growth, as well as the far-field spectra and time-domain pulses which result. Predicted accelerograms are in better qualitative accord with strong motion data.

The model predicts significant consequences for the spectral and time-domain characteristics of the earthquake teleseismic signal due to the presence of stress irregularities. For example, Figure 5.6 compares the short-period teleseismic P-wave for the stress-concentration model with that for a uniform stress model (scaled to a source dimension equal to the dimension of the stress concentration). Both the period and amplitude of the b phase (first peak-to-trough) agree for the two models, while the stress-concentration model has twice the moment of the uniform stress model. The two events have been superimposed on an  $m_b$  versus  $M_s$  plot (from Filson and Bungum, 1972) to illustrate that the stress-concentration phenomenon enhances separation of earthquake and explosion populations.

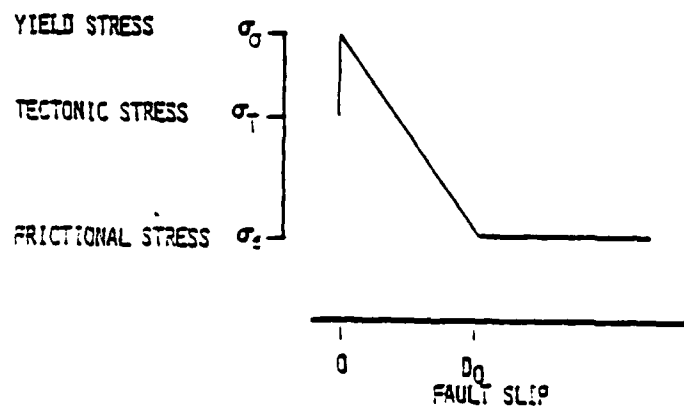


Figure 5.1 Displacement-weakening constitutive model for the fault zone.

a) Stress-concentration model.

b) Multiple stress-concentration model.

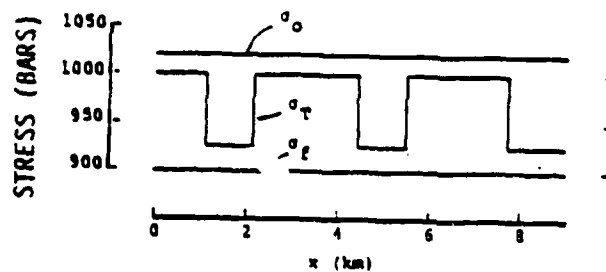
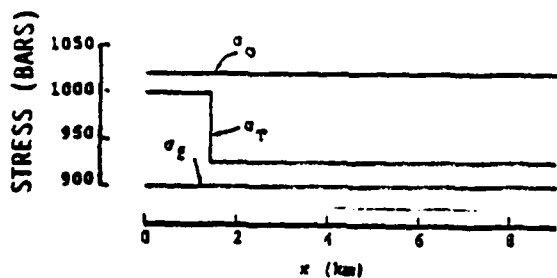
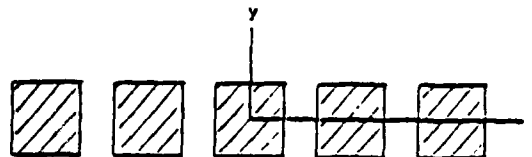
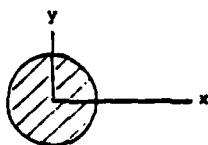


Figure 5.2 Stress-concentration fault models considered in this study.

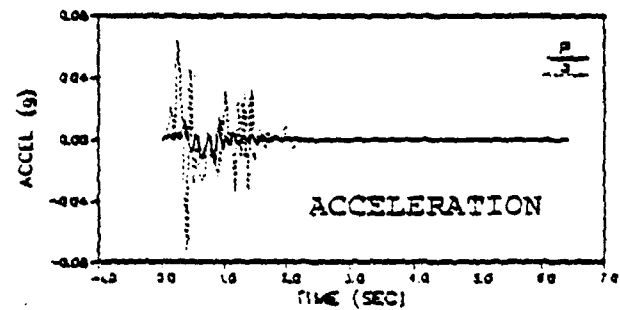
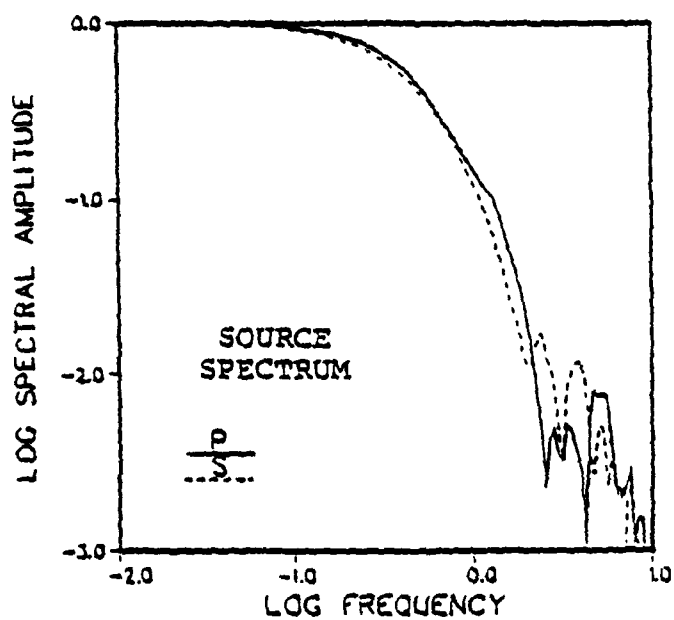
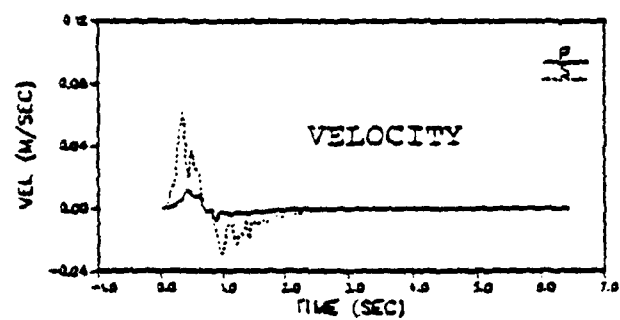
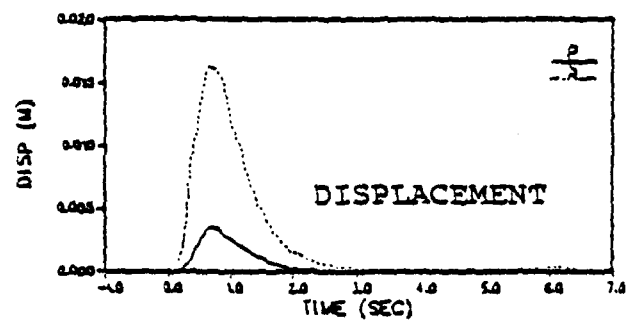
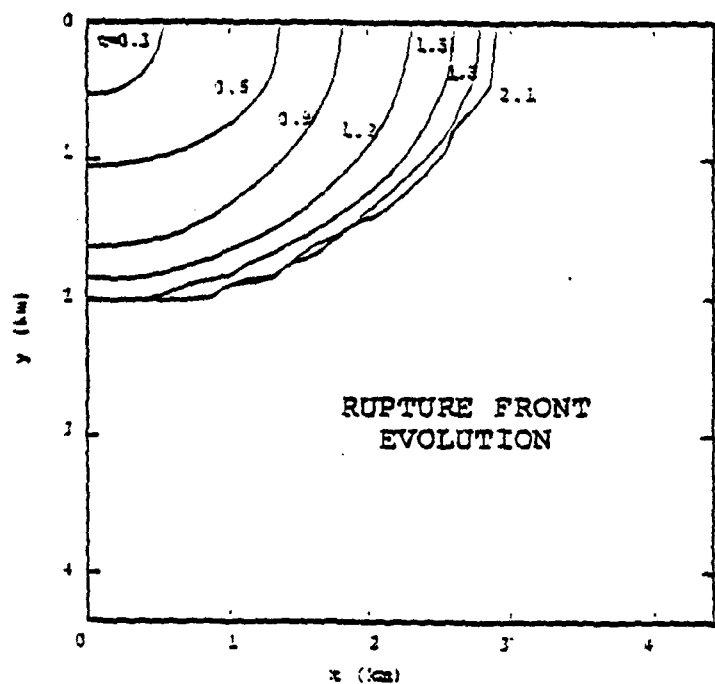


Figure 5.3 Rupture mechanism and far-field spectra and pulse shapes for stress concentration earthquake model (at spherical coordinates  $\theta = 45^\circ$ ,  $\phi = 45^\circ$  relative to fault normal).

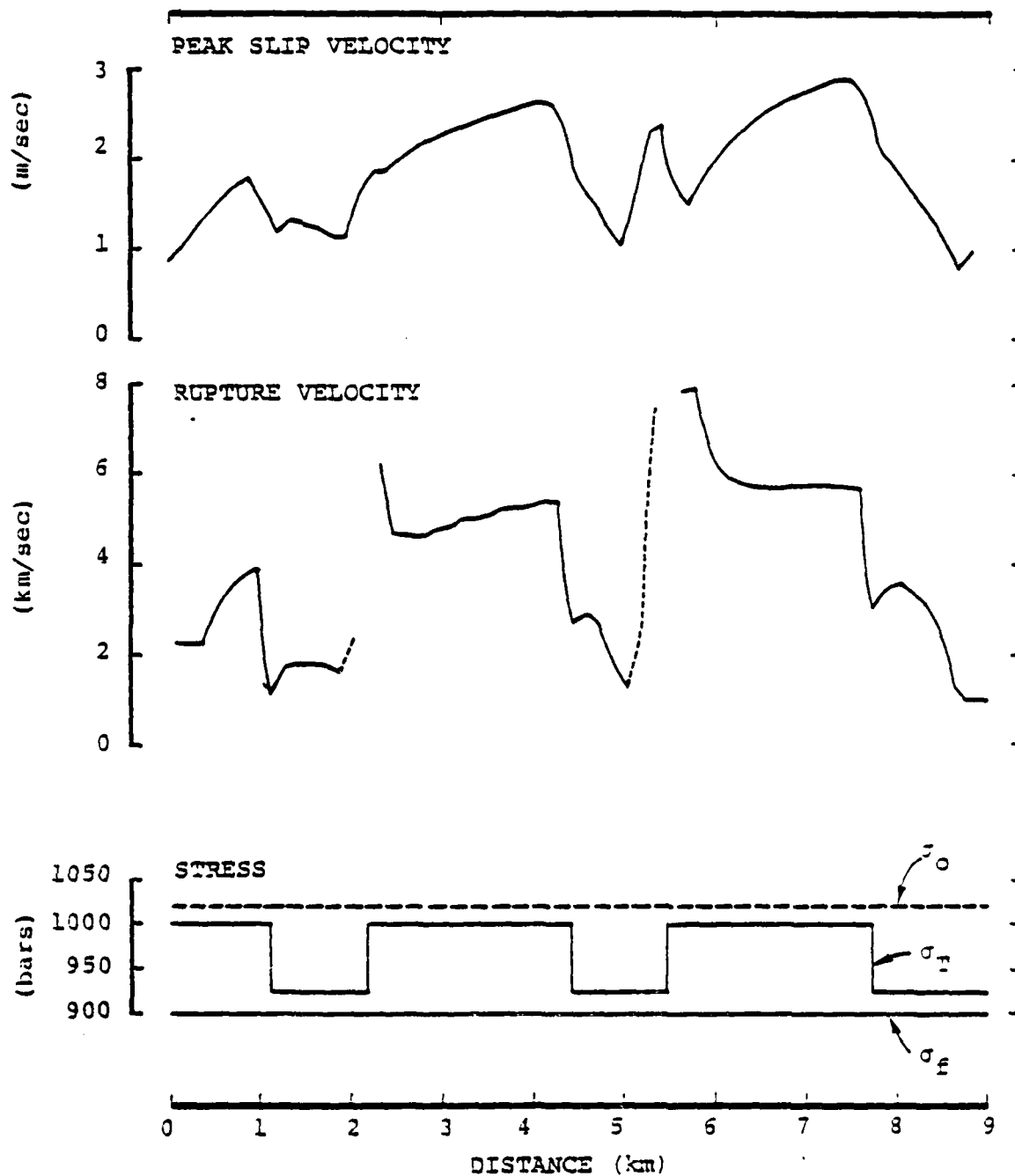


Figure 5.4 Peak slip velocity (low-passed, 5 Hz cutoff) and rupture velocity along the x axis, for multiple stress-concentration model. Dashed curves for rupture velocity indicate regions which ruptured out of sequence. For example, rupture occurred at  $x = 5.6$  km while the region between 5.0 and 5.6 km was still intact.

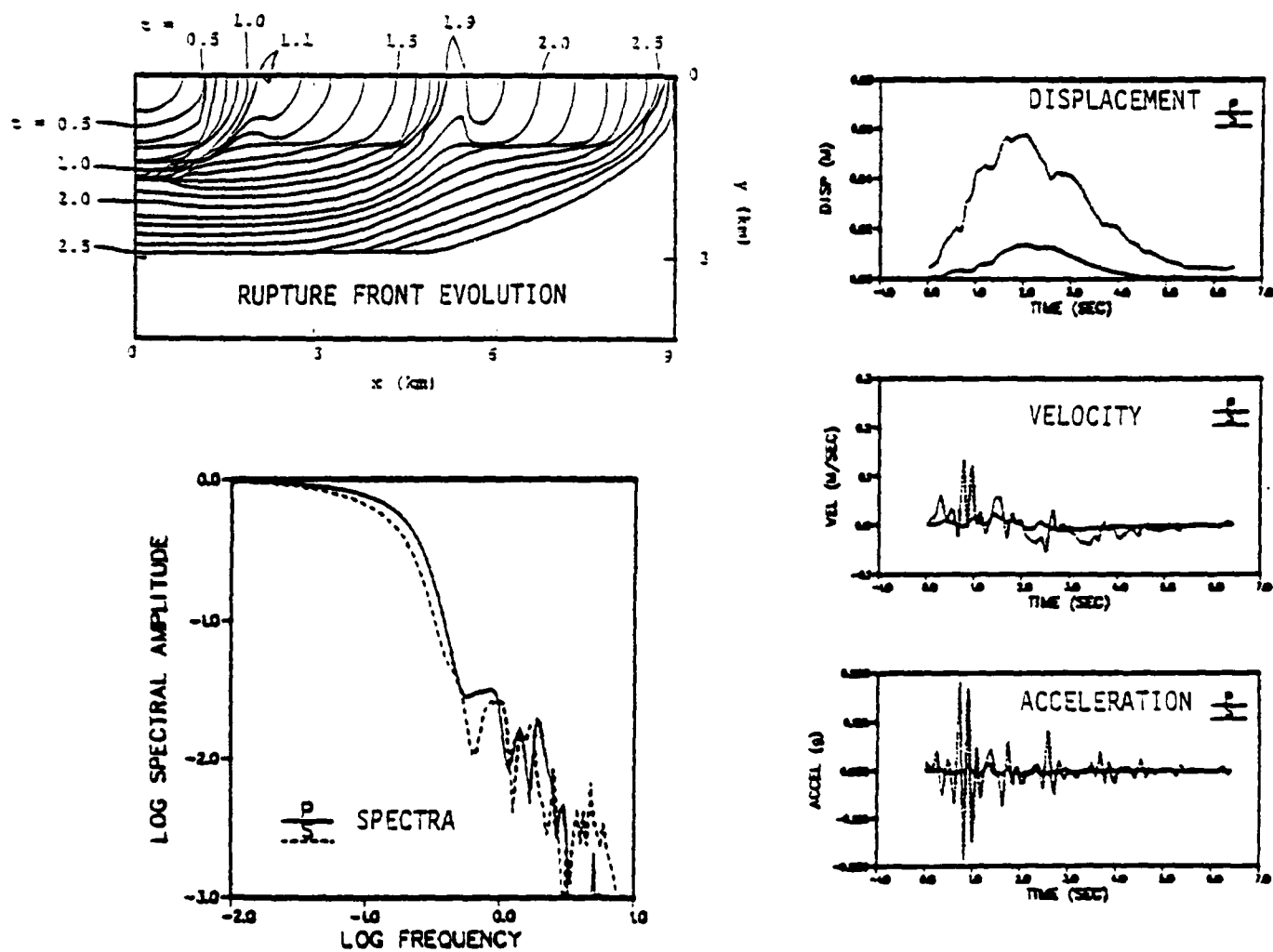


Figure 5.5 Rupture mechanism and far-field spectra and pulse shapes for multiple stress-concentration earthquake model (at spherical coordinates  $\theta = 45^\circ$ ,  $\phi = 45^\circ$  relative to fault normal).

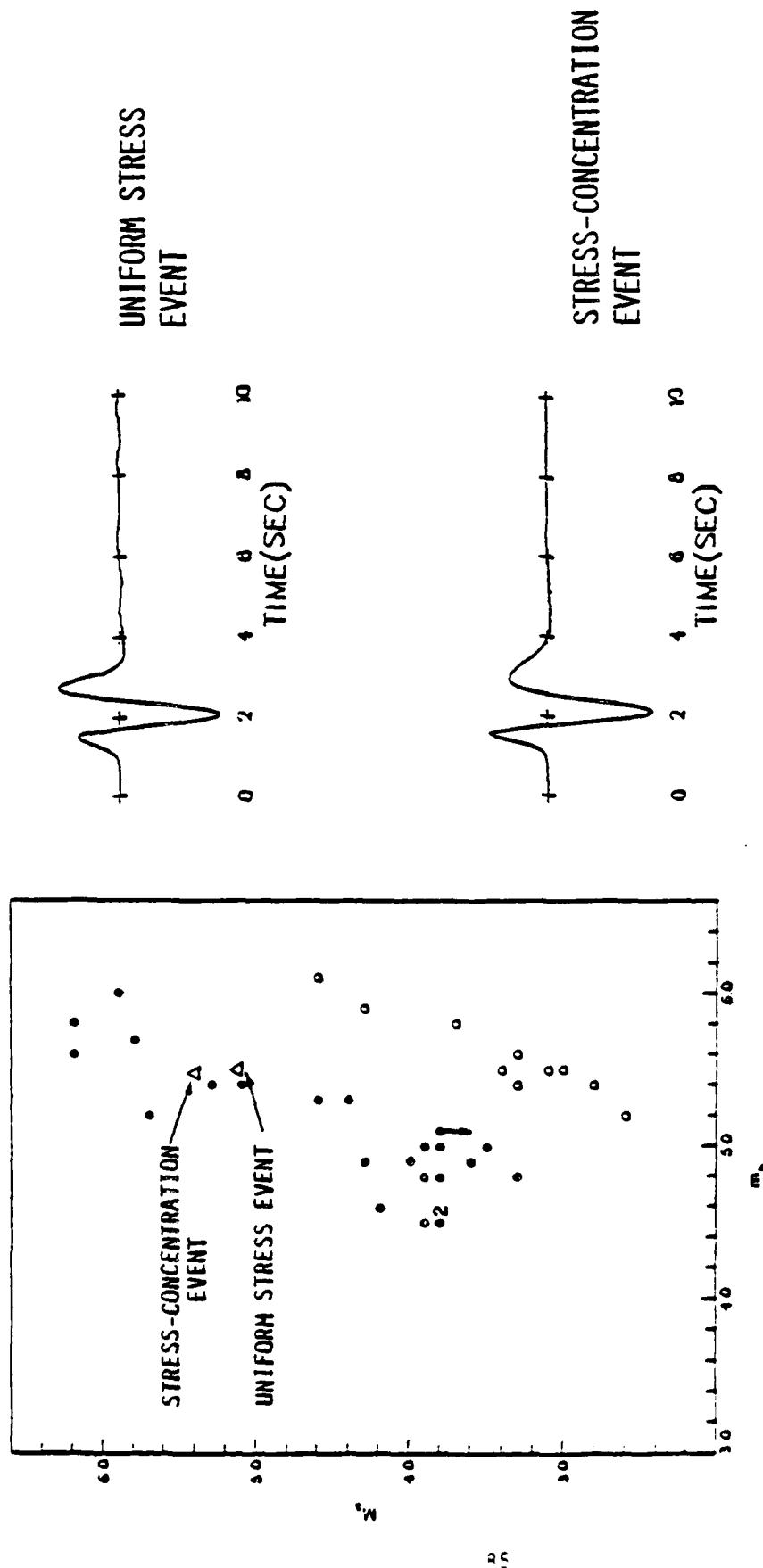


Figure 5.6 Short-period P-waves from uniform stress model and stress-concentration model. The two events are plotted as triangles on an  $m_b$ -versus  $M_s$  diagram (from Filson and Bungum), in which open circles and closed circles represent presumed explosions and earthquakes, respectively.

## VI. AUTOMATED MAGNITUDES, $\hat{m}_b$ AND $\hat{M}_s$

### 6.1 INTRODUCTION

In this section we describe algorithms for computing automated spectral body and surface wave magnitudes,  $\hat{m}_b$  and  $\hat{M}_s$ , that promise to give more consistent and convenient measures of signal energy than the currently used time domain magnitudes. The use of these magnitudes is illustrated by application to seismograms constructed by embedding synthetic signals in actual noise recordings.

The automatic magnitudes may be viewed as a byproduct of signal processing by the  $S^3$  MARS program. This program is based on the application of a series of Gaussian narrow-band filters to the data. Applications include the following:

1. Determination of phase and group velocity dispersion of surface waves. An example of the application of MARS for this purpose was mentioned in Section 3.3.
2. Detection. MARS was implemented as a P wave detector during the VSC conducted discrimination experiment in FY '78 and '79.
3. Discrimination. The MARS program computes high and low frequency spectral estimates called  $\bar{m}_b(f)$ . The discriminant used by  $S^3$  in the discrimination experiment is based on comparison of these  $\bar{m}_b(f)$  values with earthquakes and explosions falling in different portions of the plane.

A natural extension of this work is to use MARS to automatically provide the magnitude needed to estimate the size of the event. Ultimately, the program could automatically detect, discriminate and estimate yield.

Bache (1979) and Bache, Day and Savino (1979) proposed an algorithm for determining a MARS based body wave magnitude called  $\hat{m}_b$ . This algorithm was tested by processing recordings of eleven Pahute Mesa explosions from six teleseismic stations. The  $\hat{m}_b$  values were compared to a carefully determined time domain  $m_b$ . The statistics of a linear regression on log yield were also compared. We concluded that the  $\hat{m}_b$  was at least as good a magnitude measure and yield indicator as the most carefully determined time domain  $m_b$  for the high signal/noise data processed.

The  $\hat{m}_b$  algorithm used in the earlier reports worked very well, but was primitive because it failed to account for the presence of seismic noise. The discrimination experiment work led to the development of more sophisticated algorithms for using MARS output to determine spectral amplitude (Masso, et al., 1979; Savino, et al., 1980). These algorithms incorporate corrections for the presence of interfering phases and seismic noise.

In Section 6.2 we describe a more advanced algorithm for computing  $\hat{m}_b$ . The properties of this new  $\hat{m}_b$  should be nearly the same as the properties of the  $\hat{m}_b$  used in the earlier studies. The algorithm is tested by applying it to compute  $\hat{m}_b$  for a synthetic seismogram embedded in varying levels of seismic noise. Accurate results are obtained, even when the S/N ratio is so low that a time domain  $m_b$  measurement would probably not be attempted. We complete our discussion of  $\hat{m}_b$  by computing it for a number of observations of Soviet explosions recorded at RKON.

In Section 6.5 we describe the  $\hat{M}_s$  algorithm, which is much the same as the  $\hat{m}_b$  algorithm, except that the dispersion character of the surface wave signal of interest must be specified explicitly. The time series is first processed so a signal with the expected dispersion appears to be nearly undispersed, and the  $\hat{M}_s$  is then computed just like  $\hat{m}_b$ .

Tests of the  $\hat{M}_s$  algorithm are discussed in Section 6.6. As with  $\hat{m}_b$ , these involve computation of  $\hat{M}_s$  for a synthetic seismogram embedded in varying levels of seismic noise. We summarize our conclusions in Section 6.7.

## 6.2 THE $\hat{m}_b$ ALGORITHM

The basic algorithm for computing  $\hat{m}_b$  is the same as that used by Savino, et al., (1980) to compute the high and low frequency  $\bar{m}_b(f)$  used for discrimination. In fact, it is nearly correct to say that  $\hat{m}_b = \bar{m}_b$  (1 Hz). There are some details that are different, as we shall point out when outlining the algorithm. The steps are as follows:

1. The seismogram is processed by MARS, which applies a suite of narrow-band filters to the Fourier transformed seismograms. The peaks of the envelope functions are saved for further processing.
2. The MARS detection algorithm is applied to identify an undispersed P wave arrival. The exact form of the detection algorithm is a subject for current research, but we used the particular algorithm chosen by Savino, et al., (1980), which will be discussed in more detail below.
3. A particular frequency is chosen for computing a "variable frequency magnitude," or  $\bar{m}_b(f)$ . We chose 1 Hz, though this may not be the best choice. We will describe the details of the  $\bar{m}_b$  (1 Hz) calculation in more detail below.

### Detection

The detection algorithm used by Savino, et al., (1980) is illustrated in Figure 6.1. The envelope function peaks are plotted at the associated group arrival time ( $t_g$ ) for each filter center frequency ( $f_c$ ). The amplitudes ( $A_c$ ) are indicated by the symbol on the plot, with an asterisk denoting the largest peak for each center frequency. The other symbols are 0 to 9 with, for example, a 7 indicating a peak with amplitude between 70 and 80 percent of the largest peak for that center frequency.

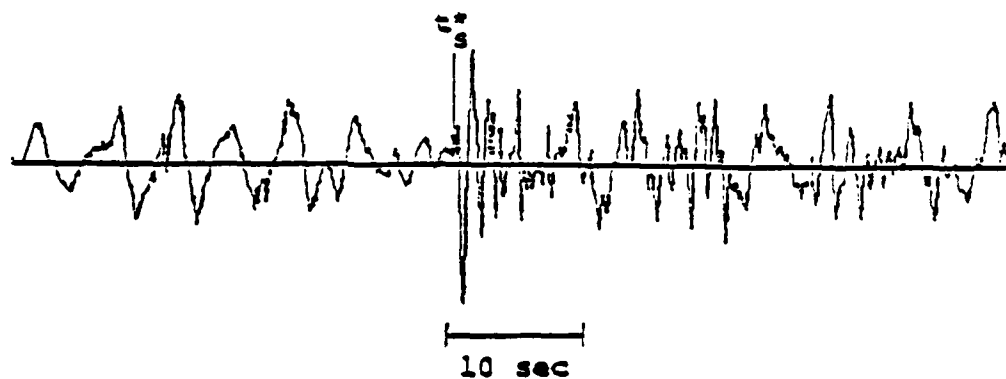
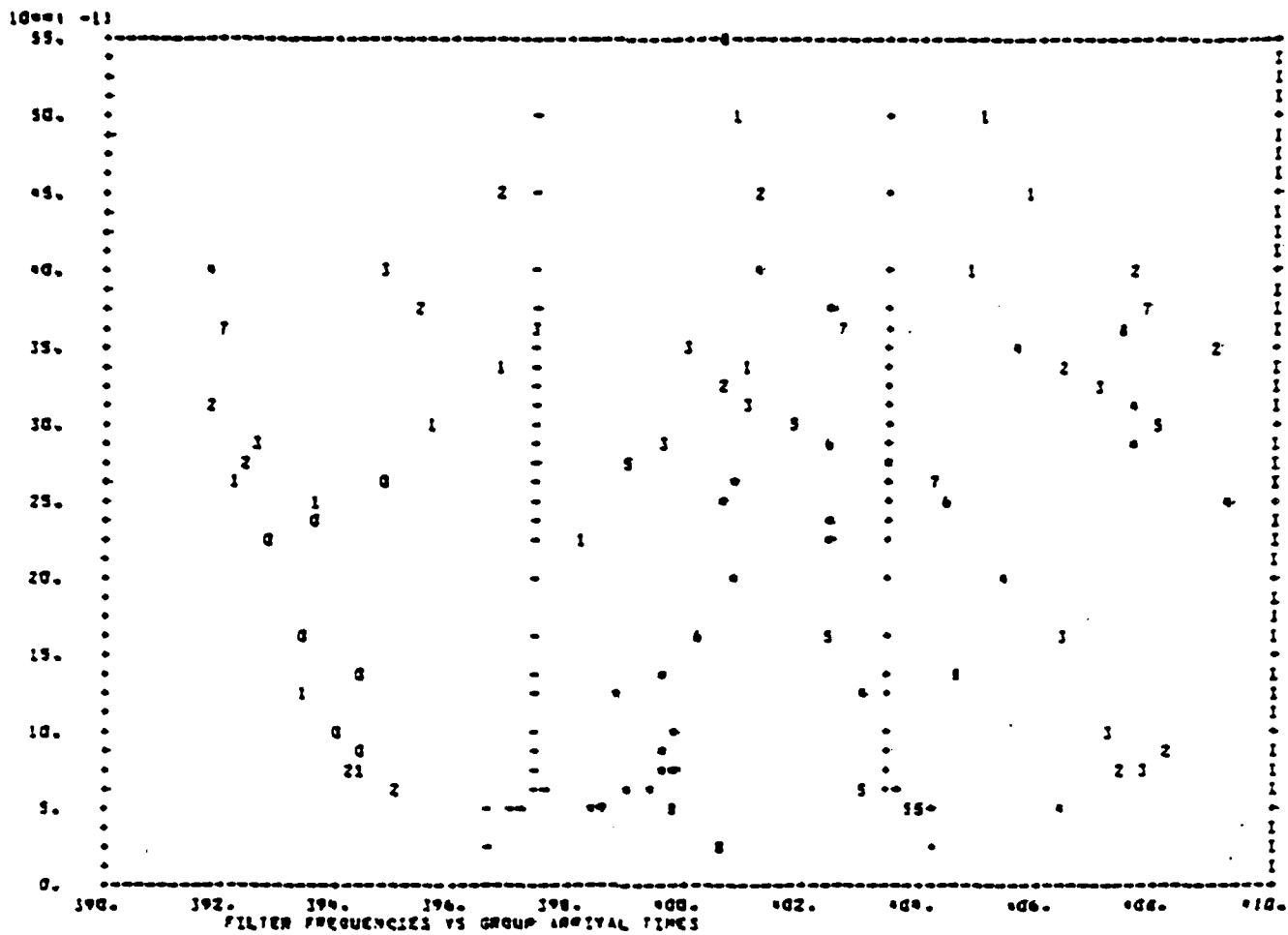


Figure 6.1. Bottom portion is a seismogram recorded at a station in Bluff, Alaska, from an event in the Kurils. The top half is a plot of filter center frequency versus group arrival time (sec). The  $t_s^*$  with arrow attached shows where the automated detection and first arrival algorithms picked the signal arrival time.

The detection algorithm starts with a "surface" of the kind shown in the figure and searches for a "ridge" which indicates an undispersed arrival. This pattern recognition is done iteratively, with the time window being progressively narrowed about regions that appear to include a signal with the desired characteristics. The  $t_g$ - $f_c$  section shown in Figure 6.1 is the final pattern used for defining the group arrival time,  $t_g$ , of the detected signal. This is the time of arrival of the maximum signal energy. The algorithm also identifies the first arrival time of the signal,  $t_s^*$ , which is noted on the seismogram.

### Spectral Resolution

To compute the variable frequency magnitude values, it is necessary to identify one spectral amplitude ( $A_c$ ) for each  $f_c$ . In figure 6.1 the '+' and '-' signs denote an "acceptance window" centered about the group arrival time  $t_g$ . The window is based on some statistical measures of the uncertainty in the  $t_g$  estimate. Any  $A_c$  within this window could be associated with the detected signal, and there are often several amplitudes for a particular  $f_c$ .

Savino, et al., (1980) select one  $A_c$  for each  $f_c$  in the following way. Each amplitude within the acceptance window is given a score based on its amplitude and time separation from  $t_g$ . The weighting factors were chosen so the largest  $A_c$  usually wins. The time separation plays a role in selecting between points of similar amplitude.

This spectral resolution algorithm is somewhat arbitrary and a better algorithm might occasionally choose a different  $A_c$  for a particular signal. One weakness that becomes apparent in the  $\hat{m}_0$  calculations we will be discussing is that the algorithm chooses an  $A_c$  for each  $f_c$  independent of the choice at nearby  $f_c$ . The algorithm used by Bache (1979) also used a score to choose the  $A_c$ , but the score was intended to select points that lead to the "smoothest" dependence of  $A_c$  and  $t_g$  on  $f_c$ . Of course, all reasonable algorithms give the same choice of  $A_c(f_c)$  when signal/noise is large.

### Variable Frequency Magnitude Calculation

Having identified one  $A_c$  for each  $f_c$ , we have an estimate for the spectrum of the detected signal. For discrimination, Savino, et al. (1980), compute  $\bar{m}_b(f)$  from these  $A_c$  at two frequencies, one high (e.g., 2.0 Hz) and one low (e.g., 0.5 Hz). The magnitude is computed from

$$\bar{m}_b(f_c) = \log (A_g^{**}(f_c) \cdot f_c) + B, \quad (1)$$

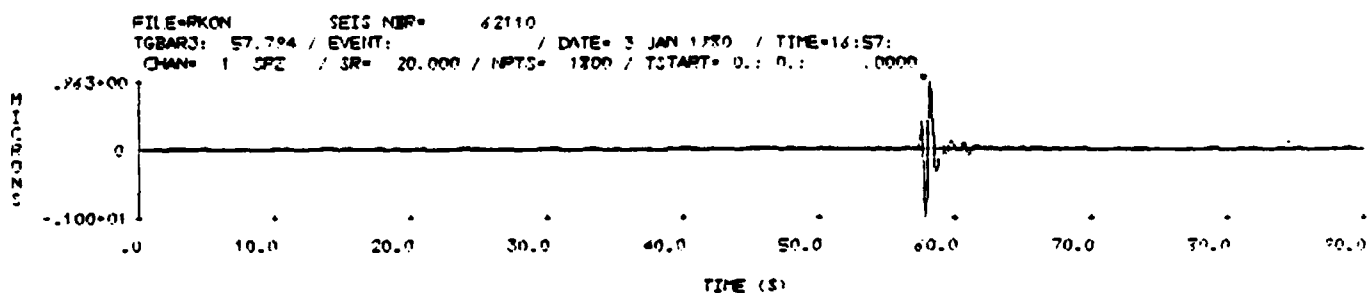
where  $B$  is the usual distance correction. The  $A_g^{**}$  is the envelope amplitude,  $A_c$ , corrected for noise (which can also be nearby "signals"). This is done by subtracting the contribution of nearby envelope peaks from the  $A_c$  for the selected peak. Also, rather than use the noise-corrected amplitudes at a single frequency, a band of frequencies is selected. A noise-weighted, least squares quartic fit to the amplitudes in that band is then made, and the  $A_g^{**}(f_c)$  is the value of the fitted quartic at  $f_c$ . Thus, a kind of "smoothing" is applied to the spectrum.

### Noise Uncertainty

We mentioned the "deterministic" noise correction that accounts for the influence of nearby envelope peaks on the amplitude of the selected envelope peak. This correction accounts for nearby "signal" as well as true seismic noise. Random noise is also important, so the noise spectrum is estimated from a noise window, usually 50 seconds or so, preceding the detected signal. The larger the ambient noise, the larger the uncertainty in the amplitude  $A_g^{**}(f_c)$ . A statistical estimate of this uncertainty is made as part of the  $\bar{m}_b(f)$  calculations.

### $\hat{m}_b$ Calculation

To compute the  $m_b$  of this report, we essentially calculated  $\bar{m}_b(1 \text{ Hz})$ . The calculation is illustrated in Figure 6.2. The seismogram is a synthetic for an explosion source. It is added to a



MBF PLOT  
 MB= 3.582 DM8= .001 DM8= -.001 MBNF= 1.247 S/N= .106 BDCL= 3.910  
 FLEFT= .800 FC= 1.000 FRIGHT= 1.200

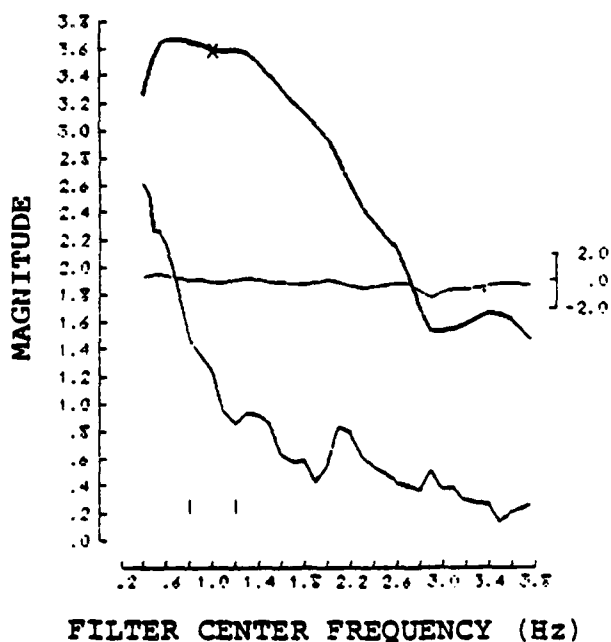


Figure 6.2. Calculation of  $m_b$  for a seismogram with peak synthetic/peak noise = 100. The seismogram is shown at the top with an asterisk denoting the signal arrival time  $t_g$ .

noise sample taken from an RKON recording in the AI data base (Savino, et al., 1980). For this case the ratio of the largest peak on the synthetic to the largest peak on the noise sample (peak synthetic/peak noise) is 100.

The  $\hat{m}_b$  calculation is shown graphically at the bottom. The heaviest line is a plot of  $\log(A_g^{**} \cdot f_c) + B$  versus  $f_c$ . The  $t_g$  associated with each  $A_g^{**}$  is plotted as the lightest line, with the scale at the right. Zero on the  $\bar{t}_g$  scale is  $t_g$ , which is also indicated by an asterisk on the seismogram. The lowest line of medium shade is  $\log(A_N \cdot f_c) + B$ , where  $A_N$  is the peak noise amplitude at  $f_c$ .

The main information about  $\hat{m}_b$  is printed with the graph. The  $\hat{m}_b$  is called MB and is marked with an X on the spectral plot. The noise uncertainty is  $\pm$  DMB. These values are not symmetric about  $\hat{m}_b$ , though they appear to be when they are small as in this example. The B correction used to convert to magnitude is listed as BDEL.

The  $\hat{m}_b$  in this and subsequent examples in this report is computed from the noise corrected amplitude at 1 Hertz. When describing the  $\hat{m}_b(f)$  algorithm, we mentioned that the amplitude at the selected frequency is taken from a least squares quartic fit to the amplitudes in a band about that frequency. Since we used only five points in the band, this part of the algorithm is inoperative for our  $\hat{m}_b$  examples. The intent was to smooth the spectrum over the band from 0.8 to 1.2 Hertz, marked by vertical bars in the graph and listed as FLEFT and FRIGHT. In the examples to be shown a smooth fit can be made by eye and we can see that it would make little difference in almost every case.

The remaining undefined quantities with the  $\hat{m}_b$  graph are MBNF and S/N. The MBNF is the noise magnitude at 1 Hertz. The S/N is the mean signal/noise power over the selected band (0.8 to 1.2 Hz).

The  $\hat{m}_b$  for the seismogram in Figure 6.2 is 3.589. This may be compared to the time domain  $m_b$  of 3.776, which is computed from  $\log(A/T) + B$ , with  $T = 0.72$  seconds. Systematic differences

between the time domain  $m_b$  and the spectral  $\hat{m}_b$  are expected. We believe the  $\hat{m}_b$  is a more convenient and consistent measure of the spectral energy in the P wave.

The  $A_g^{**}$  spectrum from which the  $\hat{m}_b$  is determined is simply a smoothed version of the Fourier spectrum of an isolated pulse. This is illustrated in Figure 6.3, where the Fourier spectrum of the original synthetic seismogram, which was embedded in noise to make the seismogram in Figure 6.2, is plotted with the MARS constructed spectrum from that figure.

We have described the  $\hat{m}_b$  algorithm, as currently implemented. There are several aspects that could be improved. In particular, the amplitude used in the magnitude calculations should be based on the fit to values in a band, rather than a single frequency value. Also, the algorithm for selecting the appropriate amplitudes for each  $f_c$  might be improved by including some information about the "smoothness" of the frequency dependence.

In the next section we demonstrate that this algorithm gives excellent results in its current form. Thus, we cannot expect large improvements from any changes.

### 6.3 $\hat{m}_b$ TEST CALCULATIONS

To test the  $\hat{m}_b$  algorithm we added a synthetic seismogram to seismic noise, scaled to different amplitude levels. In Figure 6.2 we showed a case with peak synthetic/peak noise = 100. Examples will be shown with the same synthetic and the ratio reduced to 3, 1 and 0.5. Two different noise sections were used, both from RKON recordings that were in the AI data set. The timing of the synthetic within the noise segment was also varied.

In Figure 6.4 we show 9 examples that are variations on the example in Figure 6.2. The synthetic seismogram is added at four different times, with the noise scaled to different levels. In Figure 6.5 we show five more examples which are constructed the same way with an RKON noise sample from another day.

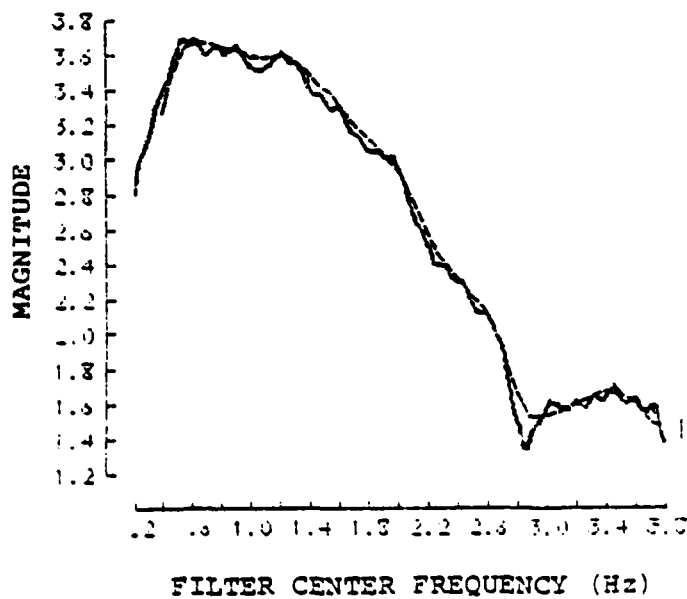


Figure 6.3. Comparison of the Fourier velocity (amplitude times frequency) spectrum to the MARS log ( $A \cdot f_c$ ) spectrum (dashed line). The amplitude is in  $m_b$  units.

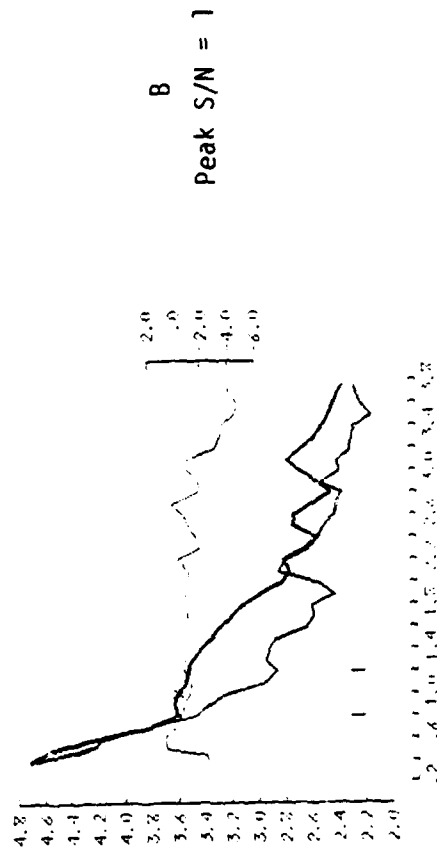
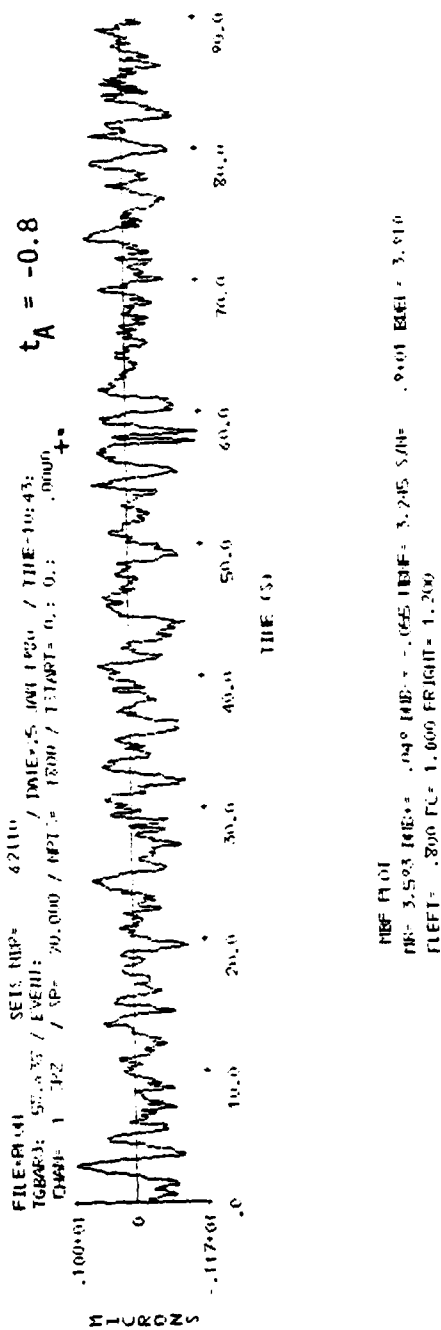
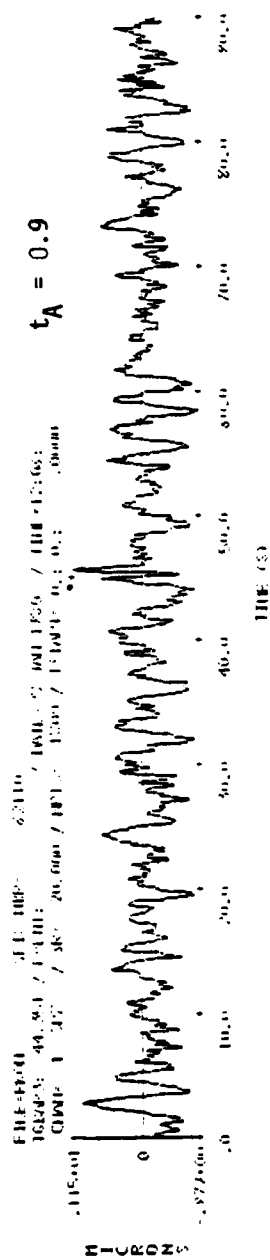


Figure 6.4. Test of the  $\hat{m}_b$  algorithm with a synthetic seismogram embedded in noise section 62110. The ratio of the peak amplitude of the synthetic to the peak noise amplitude is denoted by Peak S/N. The actual arrival time of the signal is the time of the asterisk plus  $t_A$ .



IRF (A.U)  
 IRF 3.66 / 1000 0.04 IRF 3.66 / 1000 0.04 IRF 3.66 / 1000 0.04  
 RUT 1.800 1.800 1.800 1.800 1.800 1.800 1.800 1.800 1.800 1.800

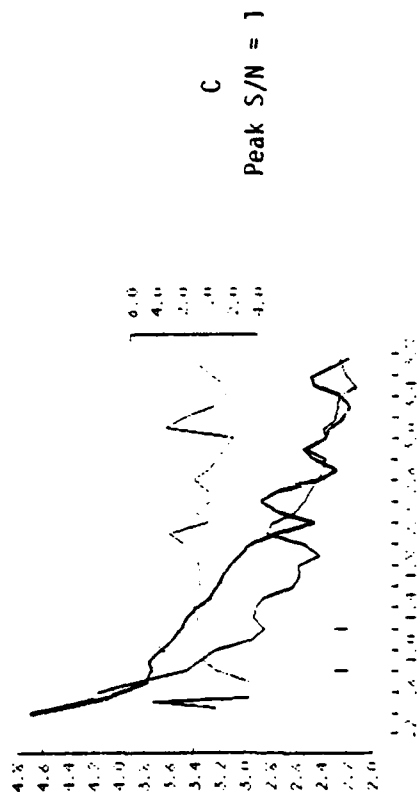
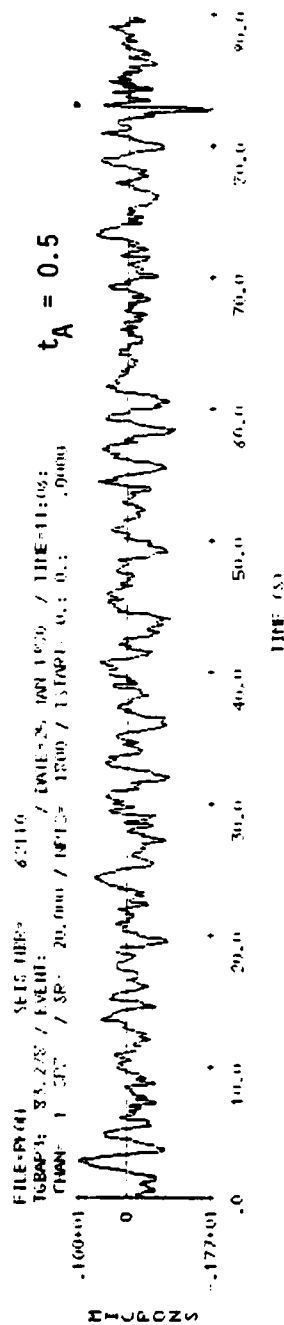


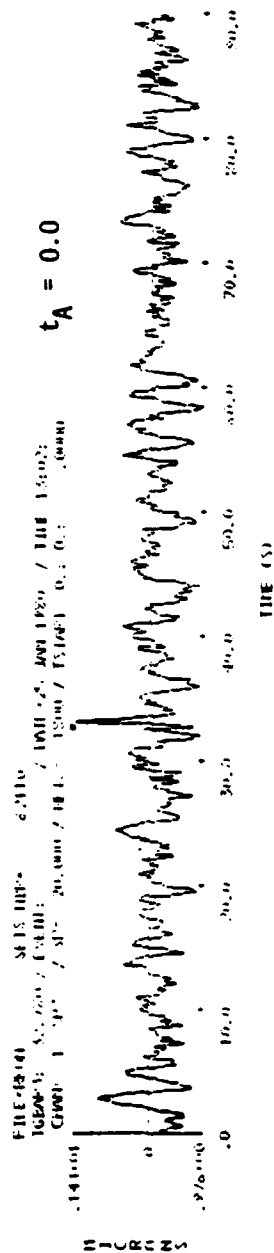
Figure 6.4. (continued).



MBF PLOT  
 MB= 3.586 MB= .066 MB= .066 MBF= 3.245 S/N= .1402 BEL= 3.916  
 FLEET= .800 FC= 1.000 FRIGHT= 1.200



Figure 6.4. (continued).



THE PLOT  
 TR: 3.581 1000.000 1000.000 1000.000 1000.000 1000.000  
 FILE: 19101 1000.000 1000.000 1000.000 1000.000 1000.000

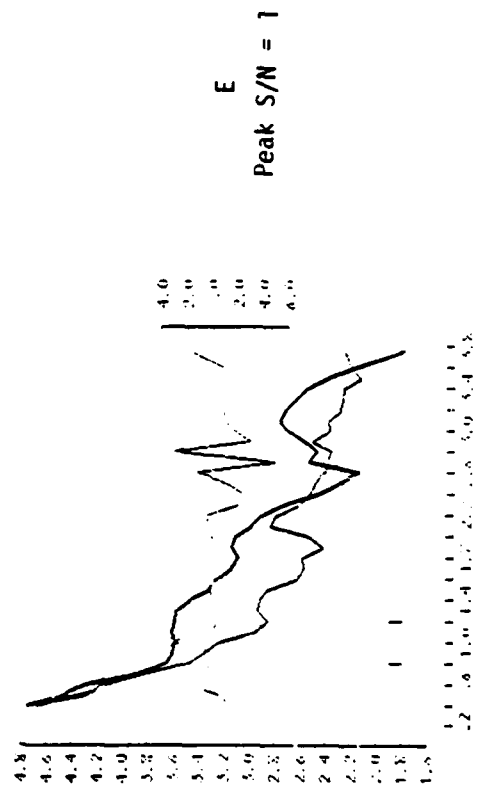
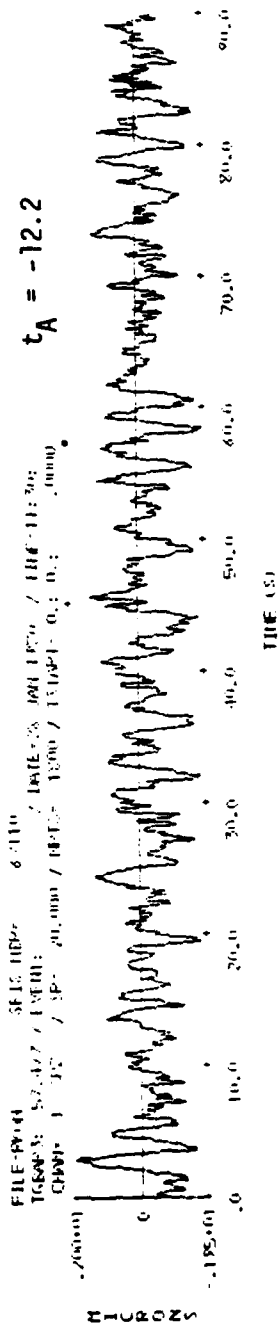


Figure 6.4. (continued).



REF: 5.247 HDS 8-110 3.546 (1.000) 3.546 (1.000)

REF: 5.247 HDS 8-110 3.546 (1.000) 3.546 (1.000)

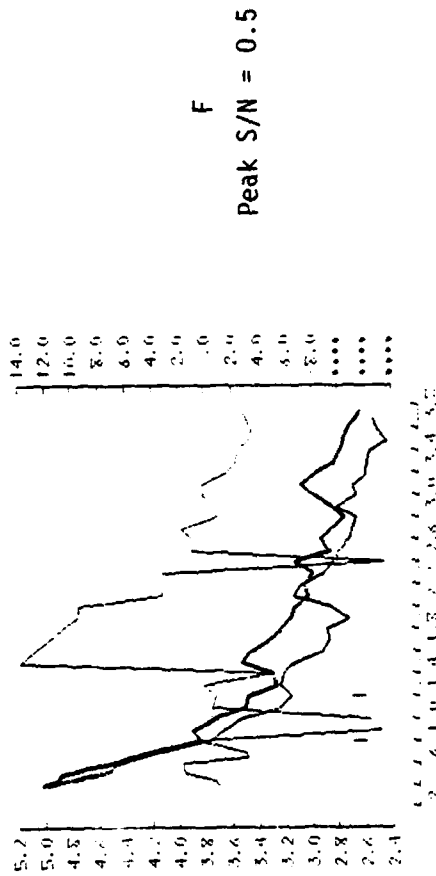
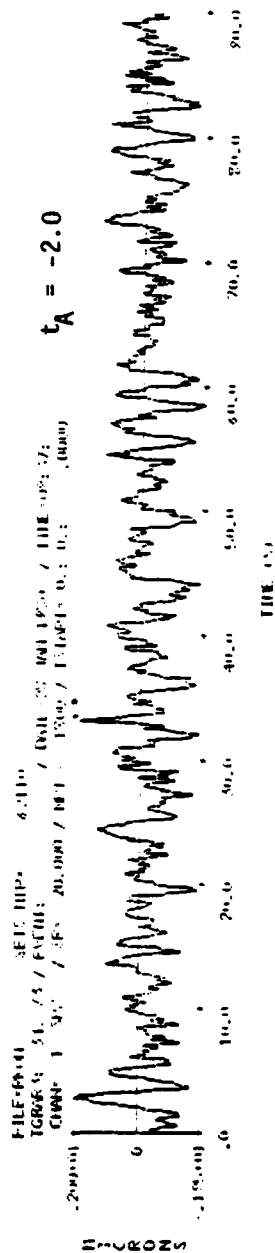


Figure 6.4. (continued).



PRF: F101  
 REF: 3.622 100.00 0.077 100.00 110.111 REF: 3.546 S/N: 3.001 FREQ: 3.910  
 F101 F101 3.000 F101 1.000 F101 1.200 F101 1.000 F101 1.000

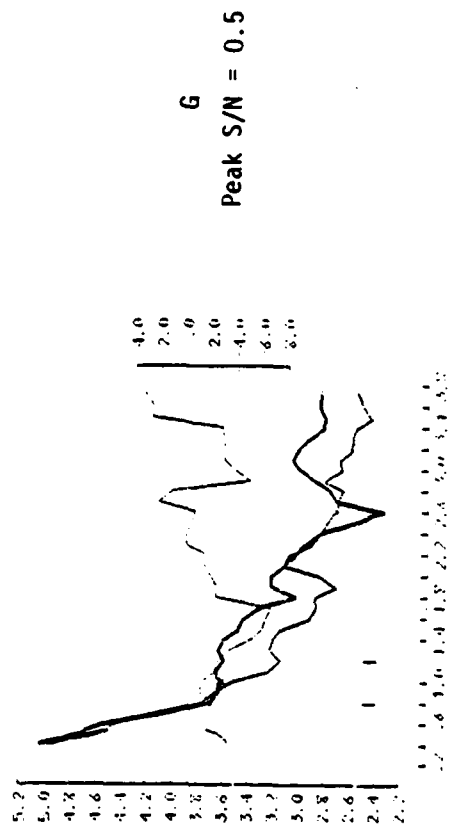
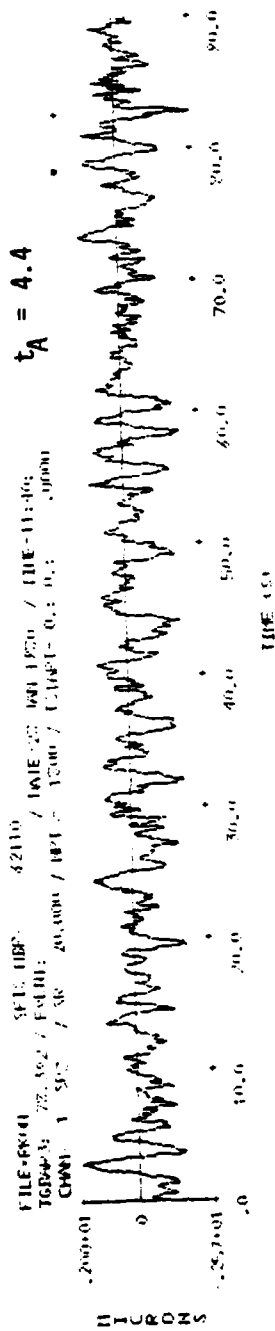


Figure 6.4. (continued).



NEF PLOT  
 IE= 3.700 DMS= .073 IIR= .065 IBSF= 3.546 S/H  
 FLEET= .800 FLS 1.000 FRIGHT= 1.200 I AT FC=22.650  
 .401 PEEL= 3.910

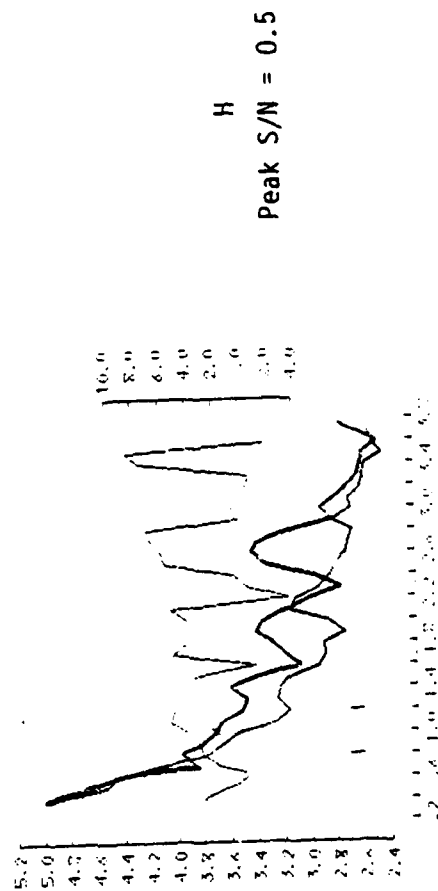
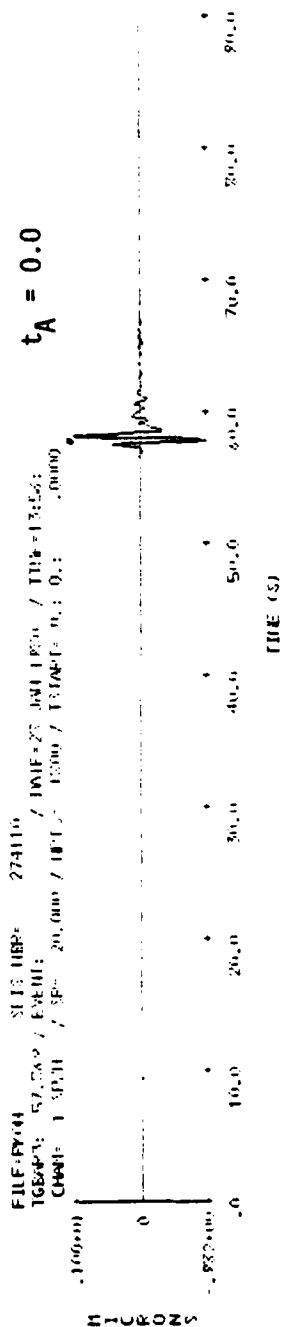


Figure 6.4. (continued).





NET PLOT

HR: 3.5% HBR: .001 HBR: .001 HBR: 1.200 G/H: .0005 REL: 3.010

FLEET: 200 FL: 1.000 FPL: 1.200 T AL: 60.57 750

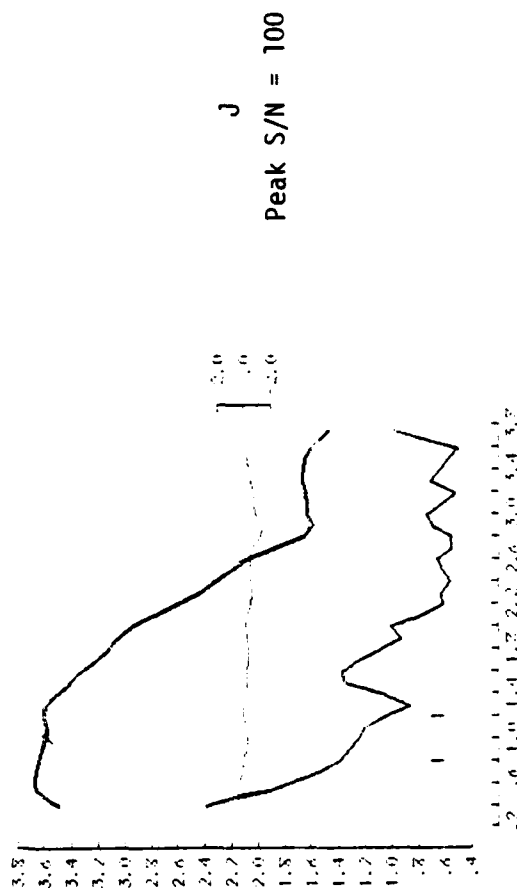
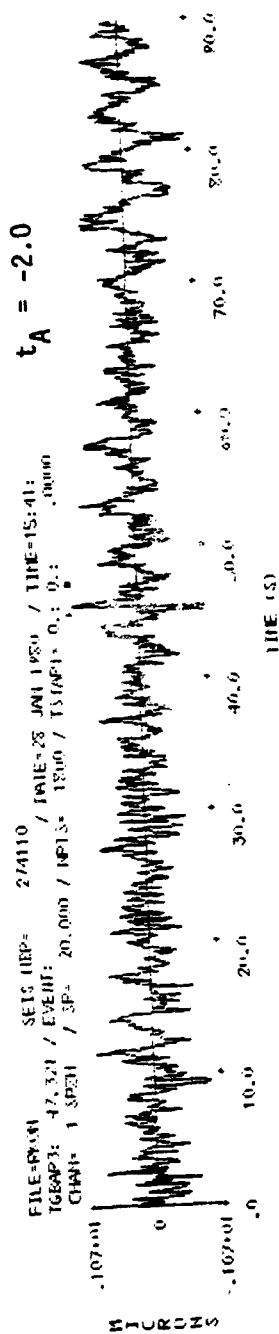


Figure 6.5. Test of the  $\hat{m}_b$  algorithm with noise section 274110.





HF PLOT  
 IB= 3.585 IEF= .073 IUB= -.095 IEF= 3.245 S/N= .501 BEEL= 3.910  
 FLEET= .300 FC= 1.000 FRIGHT= 1.200 T AT FC=45.100

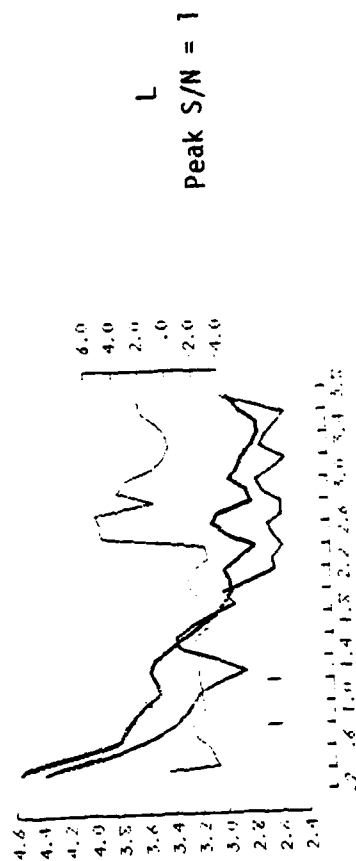
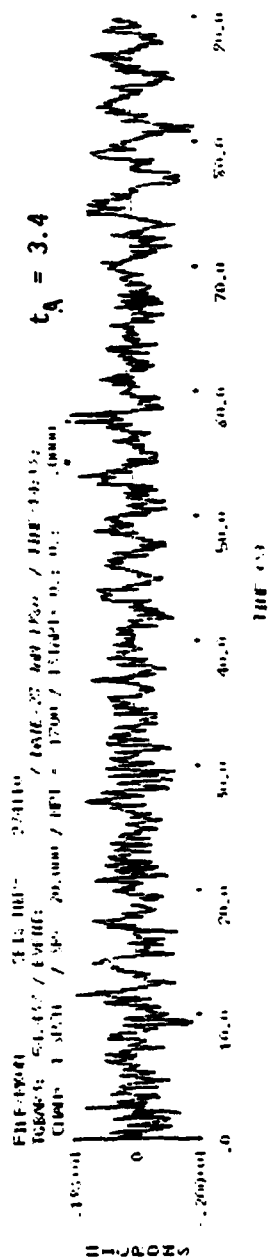


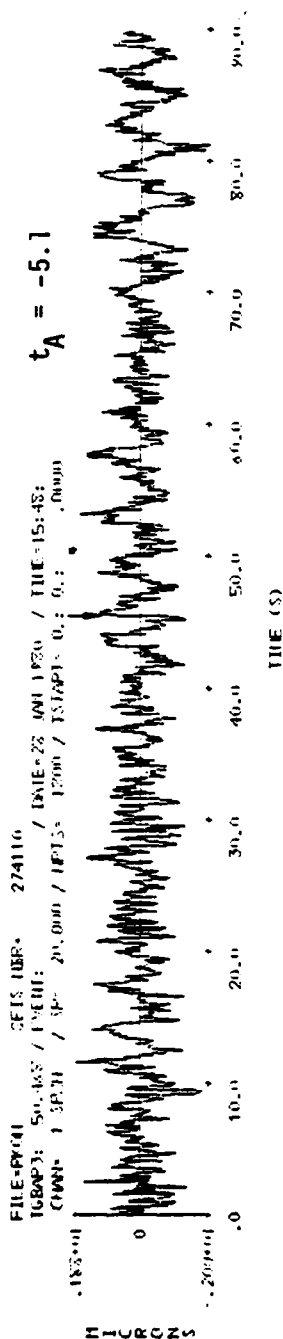
Figure 6.5. (continued).



THE FILE  
 FILE: 1000 3.15 MB 2/11/10  
 TO: 64.437 / 4/11/10 / 1000 3.15 MB 2/11/10  
 C:\1000 3.15 MB 2/11/10 / 1000 3.15 MB 2/11/10



Figure 6.5. (continued).



NSF PLOT  
 IR= 3.543 IIR= .158 IIR= -.252 IIR= 3.546 S/H  
 FIEFT= .500 FC= 1.000 FPIRIT= 1.200 I AT FC=50.556

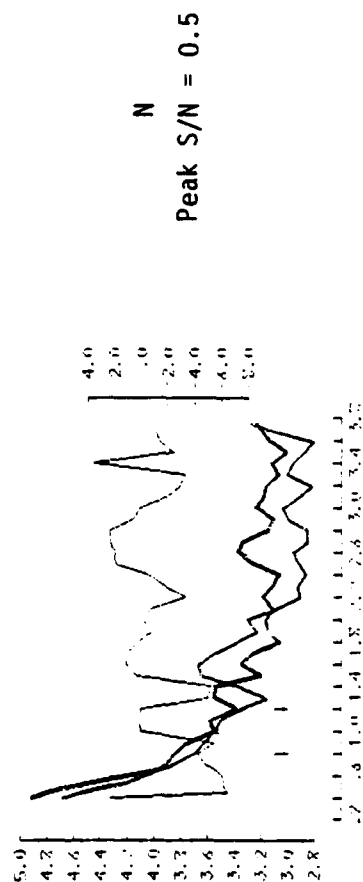


Figure 6.5. (continued).

The "correct" value for  $m_b$  is taken from the peak  $S/N = 100$  cases. For the 62110 noise sample this is 3.589 from Figure 6.2. For the 274110 noise sample it is 3.586 from the first plot in Figure 6.5. The small difference is due to differences in the way the synthetic was normalized (note the amplitude scale on the peak  $S/N = 100$  synthetics).

The "correct" arrival time is assumed to be the  $t_g$  for the Peak  $S/N = 100$  cases. It differs by only 0.08 seconds between the two noise samples.

The important data from these test calculations are summarized in Table 6.1. The seismograms are identified by the letter given beside the  $\hat{m}_b$  graph on each plot. We also list the  $S/N$  ratio at 1 Hertz and the  $\hat{m}_b$ . The  $\hat{m}_b$  uncertainty is the larger of the DM8 values, which is always the negative value. It depends directly on the  $S/N$  at 1 Hertz. The " $\hat{m}_b$  error" is simply the difference between the computed  $\hat{m}_b$  and the value for the peak  $S/N = 100$  case.

The magnitude is not meaningful if it is not computed for the right signal. Listed in the table is the "Arrival Time Error," which is the difference between the  $\bar{t}_g$  for the peak  $S/N = 100$  cases and the  $t_g$  at 1 Hz for the case being analyzed. This is also indicated on the plots. The  $\bar{t}_g$  is marked with an asterisk. When the  $t_g$  at 1 Hertz is much different from the  $\bar{t}_g$ , it is marked with a "+." The actual arrival time of the signal is denoted by  $t_A$ , as explained in the caption to Figure 6.4. In two of the low  $S/N$  cases, I and N, the signal was entirely missed. In those cases an arrow marks the actual arrival time.

There are six cases where the peak  $S/N = 1$ . These are B, C, D, E, K and L. The  $S/N$  at 1 Hertz is 2.0 to 2.6. The signal can be seen visually on the seismograms, but it is certainly below the threshold where one would be very comfortable with time domain  $m_b$  measurements.

For each of the peak  $S/N = 1$  cases, the detection algorithm accurately located the signal. The maximum arrival time error for

TABLE 6.1  
SUMMARY OF  $\hat{m}_b$  TEST CALCULATIONS

Identifier	$\frac{\text{Peak Signal}}{\text{Peak Noise}}$	S/N (1 Hz)	$\hat{m}_b$	$\hat{m}_b$ Uncertainty	$\hat{m}_b$ Error	Arrival Time Error
Noise Section 62110 (Figure 6.4)						
(Figure 6.2)	100	217	3.589	0.001	—	—
A	3	6.5	3.583	0.018	-0.006	+0.02
B	1	2.2	3.593	0.055	0.004	0.03
C	1	2.6	3.667	0.046	0.078	-0.09
D	1	2.2	3.586	0.056	-0.003	0.48
E	1	2.2	3.581	0.057	-0.008	-0.01
F	0.5	1.5	3.734	0.082	0.145	0.09
G	0.5	1.2	3.622	0.110	0.033	-0.76
H	0.5	1.5	3.708	0.088	0.119	0.14
I	0.5	1.4	3.689	Missed Signal		
Noise Section 274110 (Figure 6.5)						
J	100	219	3.586	0.001	--	--
K	1	2.0	3.536	0.111	-0.05	-0.05
L	1	2.2	3.595	0.095	0.09	-0.15
M	0.5	1.1	3.583	0.226	-0.03	-0.05
N	0.5	1.0	3.548	Missed Signal		

the 1 Hertz energy is 0.48 seconds for D. For the other seven the errors are 0.15 seconds or smaller. The mean  $\hat{m}_b$  error is 0.04 units, with three of the six having errors less than 0.01 units.

In the last section we mentioned some algorithm improvements that should be added. One was to improve the method for selecting amplitude peaks, but we doubt this would have any effect on the spectral values near 1 Hz in these examples. The second change was to fit a smooth polynomial to the spectral values between 0.8 and 1.2 Hertz. This addition would probably have an effect. For example, the  $\hat{m}_b$  for K would increase, reducing the error for that case.

There are also six cases with the peak  $S/N = 0.5$ . These are cases F, G, H, I, M, N, and the  $S/N$  at 1 Hertz is 1.0 to 1.5. For these the signal cannot be detected by eye. Even so, the 1 Hz arrival is located within 0.2 seconds in three of the six cases. In one case the error is 0.76 seconds and there are two cases (I and N) where the signal is missed altogether.

When the  $S/N$  ratio gets very low, the  $\hat{m}_b$  errors can become significant, as should be expected. For example, the error is 0.145 units for Case F. We must be careful when interpreting this error, however, since even when the signal is missed (Cases I and N) the computed  $\hat{m}_b$  is not much different from the correct value. Of course, it shouldn't be since the noise has been scaled to be about the same size as the signal.

For the low  $S/N$  cases the  $t_g$  plot is quite discontinuous. The spectral amplitudes are being selected from different portions of the signal. For example, in Case F the 1 Hertz amplitudes are associated with the correct arrival time. However, the 1.6 Hertz amplitude is associated with an arrival time 28 seconds later! The  $t_g-f_c$  section for this case is plotted in Figure 6.6. There are several apparent undispersed P wave arrivals, indicated by a series of filter peaks aligned at the same time. The  $\hat{t}_g$  is picking one such arrival, and there is another near 10530 on the  $t_g$  scale. The actual arrival is at  $t_a$  and the algorithm did choose the 1

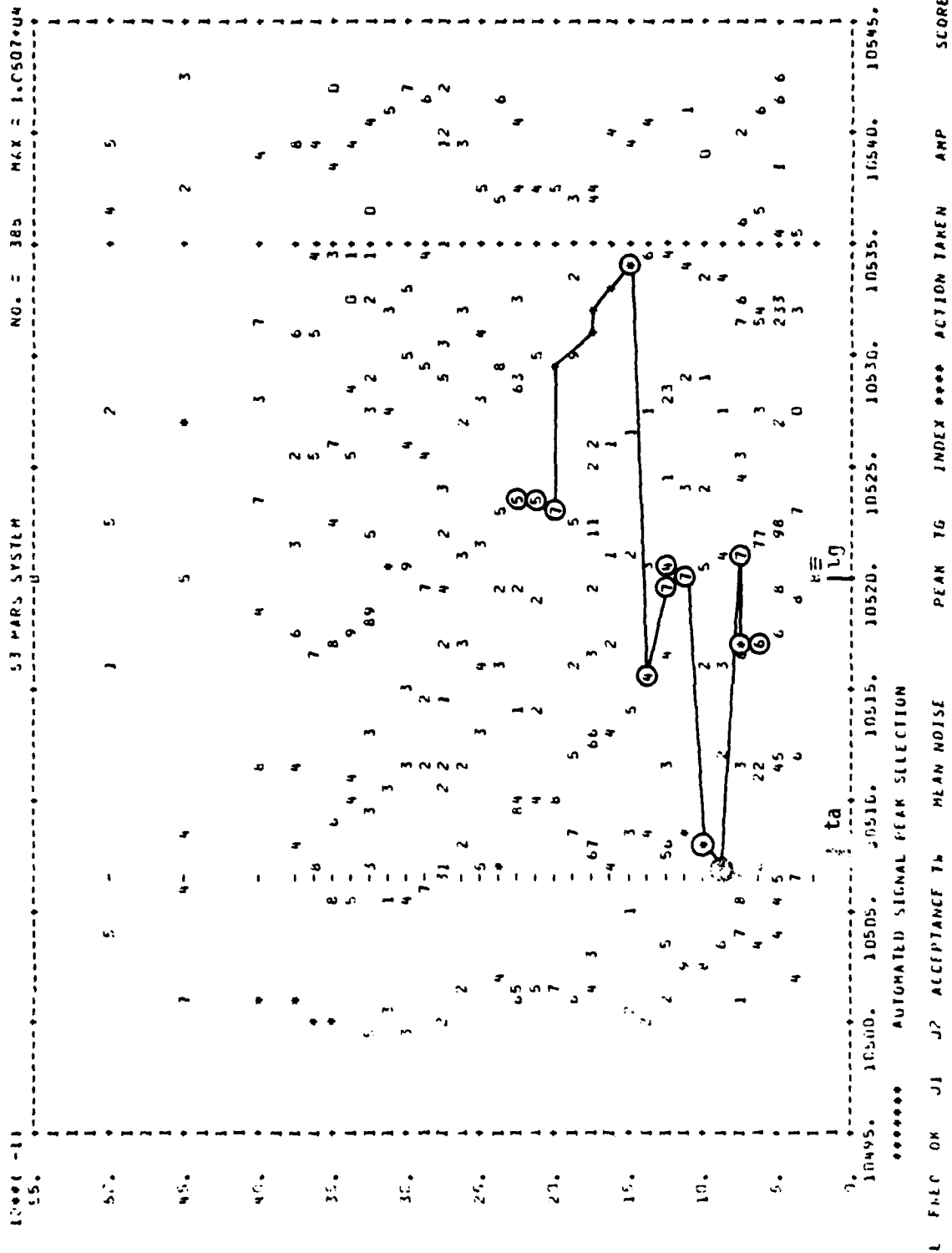


Figure 6.6. The tg-f<sub>c</sub> section for Case F of Figure 6.4.

Hertz amplitude at this time. However, at nearby  $f_c$  there are spectral amplitudes associated with this arrival that were not chosen.

The point of the discussion in the last paragraph is that the  $t_g-f_c$  plane does include estimates for the spectral amplitude of the actual signal over a significant band of frequencies, even in low S/N cases like F. Since we can identify the correct spectral peaks by eye, the automated algorithm to pick the peaks can probably be altered to duplicate the process. This would improve the results for very low S/N arrivals. But, we point out that the results in Table 6.1 indicate that the algorithm is already giving answers that are close to the inherent accuracy threshold imposed by the noise, so we cannot expect too much improvement.

#### 6.4 $\hat{m}_b$ FOR RKON RECORDINGS OF EURASIAN EVENTS

Using the algorithm described in the previous section, we computed  $\hat{m}_b$  for RKON recordings of eight presumed explosions in the Soviet Union. The locations of these events are shown in Figure 6.7. The data and the event designations are from the AI data set (Savino, et al., 1980).

The  $\hat{m}_b$  determination for each seismogram is shown in Figure 6.8. Note that the signal/noise at 1 Hertz is certainly adequate for accurately computing  $\hat{m}_b$ . However, there would be less noise contamination if the  $\hat{m}_b$  were computed at a higher frequency like 1.2 Hertz. There is no reason why the  $\hat{m}_b$  should not be computed at some frequency other than 1.0 Hertz, as long as it is done consistently. Since the process is automatic, a catalog of values could be maintained for future examination.

Similar  $\hat{m}_b$  calculations were done for two Tibetan earthquakes recorded at RKON. The results are shown in Figure 6.9 where we see that these are very low signal/noise recordings, in fact, the arrival time is very difficult to pick by eye. Finally, in Figure 6.10 we show the  $\hat{m}_b$  for a high signal/noise LASA recording of a Kurile arc earthquake.

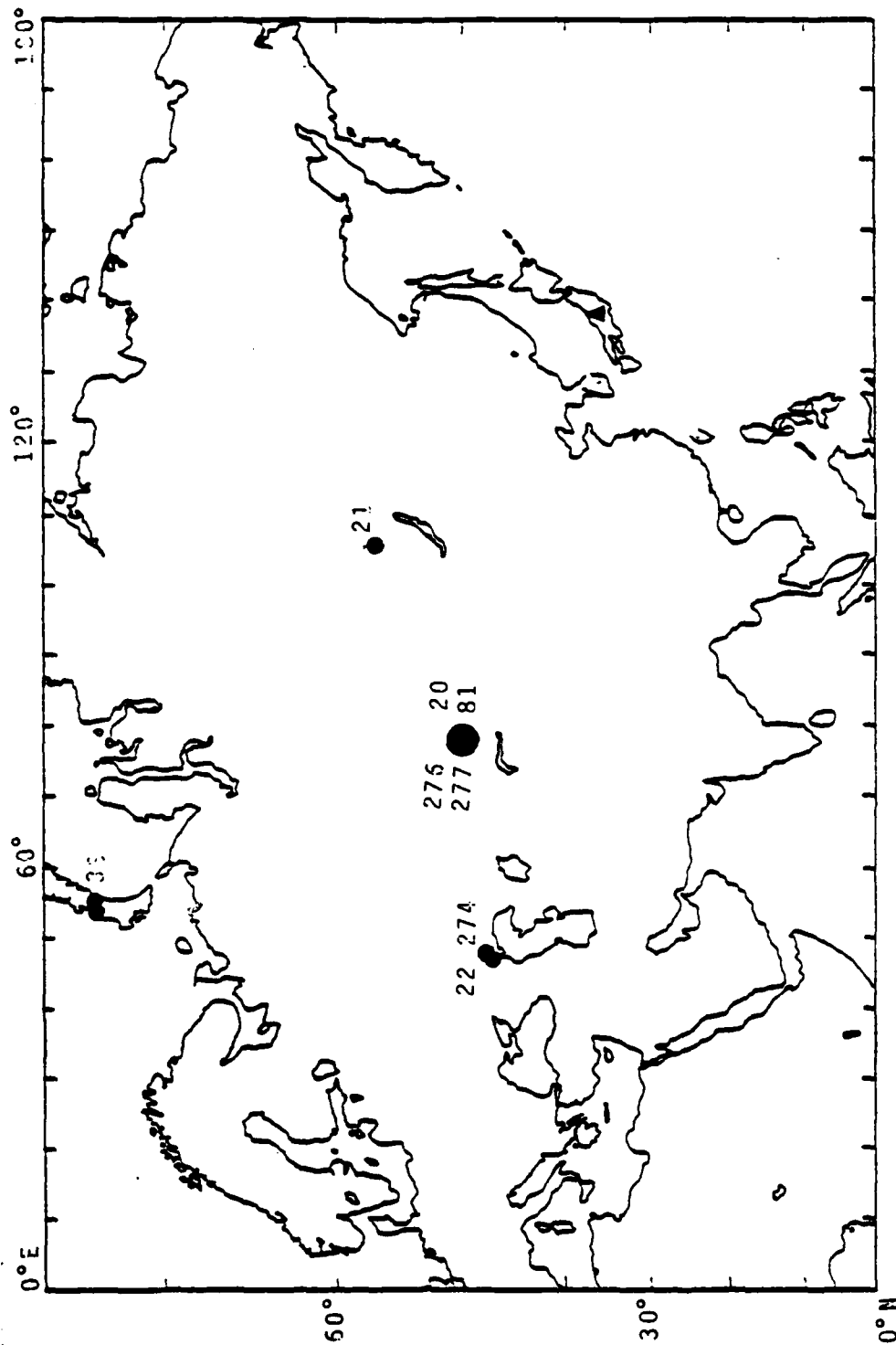
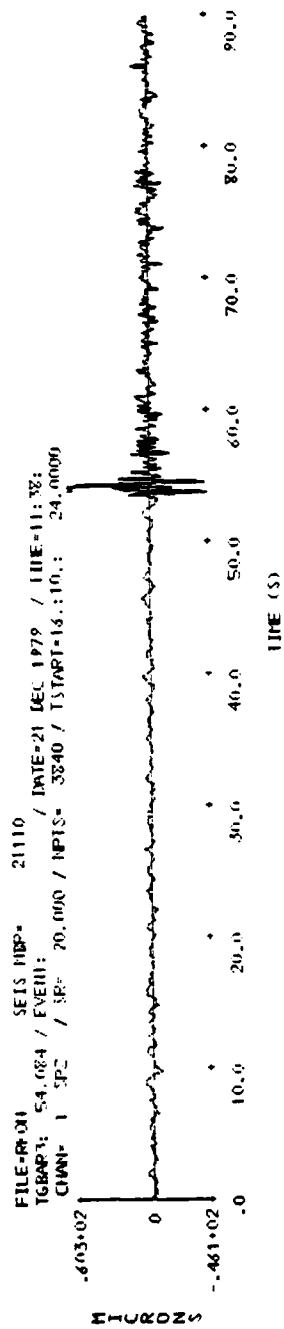


Figure 6.7. Map of Eurasia showing locations of 8 presumed explosions for which the  $\hat{m}_b$  is determined at RKON.





NRZ PLOT  
 NB- 5.114 MB- .016 MB- .016 MB- 4.251 S/N- .802 BEEL- 3.900  
 FLEET- .800 FC- 1.000 FRIGHT- 1.200

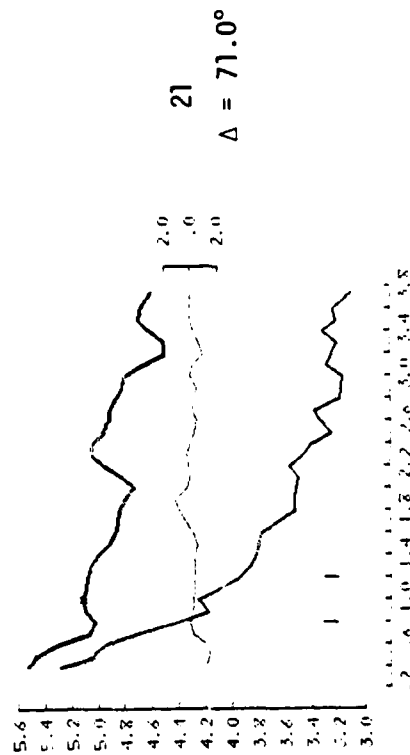
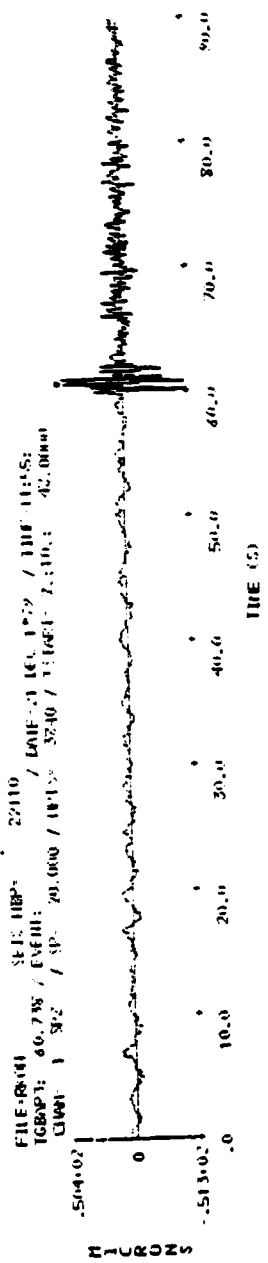


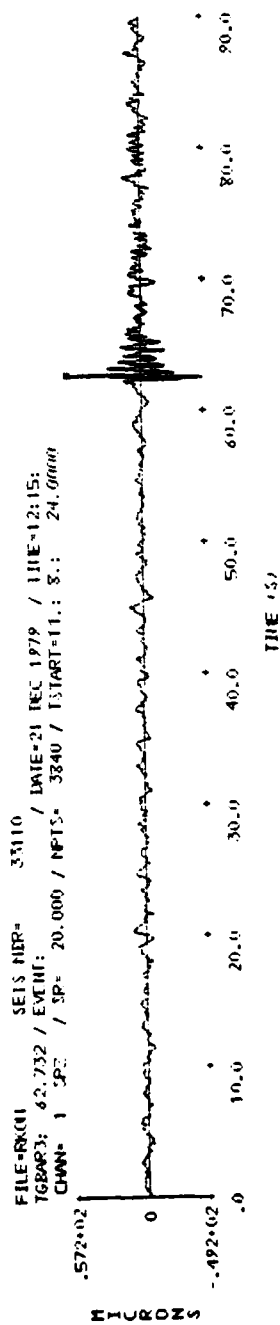
Figure 6.8. (continued).



HIF F101  
 18: 4.720 HIF: .024 HIF: .025 HIF: 4.027 S/N: .4002 REL: 3.500  
 FLEF: .300 FC: 1.000 FPHIT: 1.200



Figure 6.8. (continued).



HEF PLOT  
 IR= 4.622 DMB= .045 INB= -.051 IERF= 4.160 S/N= .7\*01 BEEL= 3.726  
 FLEFT= .800 FC= 1.000 FRIGHT= 1.200

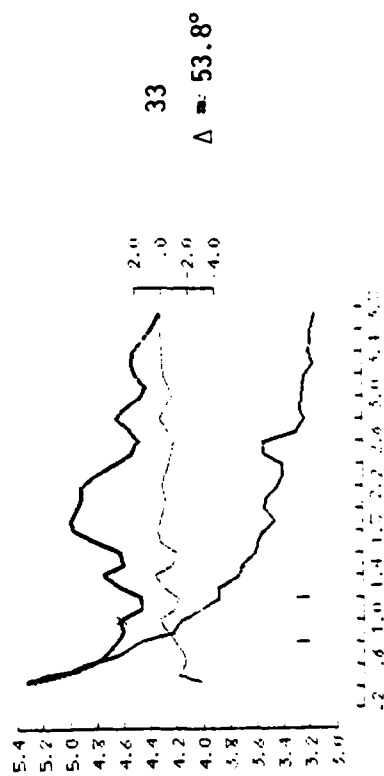
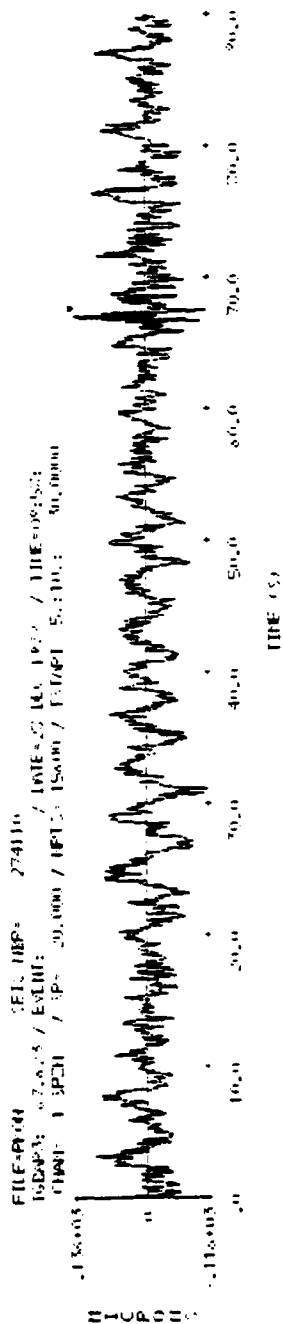


Figure 6.8. (continued).





REF FLOT  
 RE= 5.466 IRE= .029 IIR= -.112 IRI= 5.192 IRI= .300 IRI= 3.900  
 FLEET= .200 FC= 1.000 FPI= 1.200

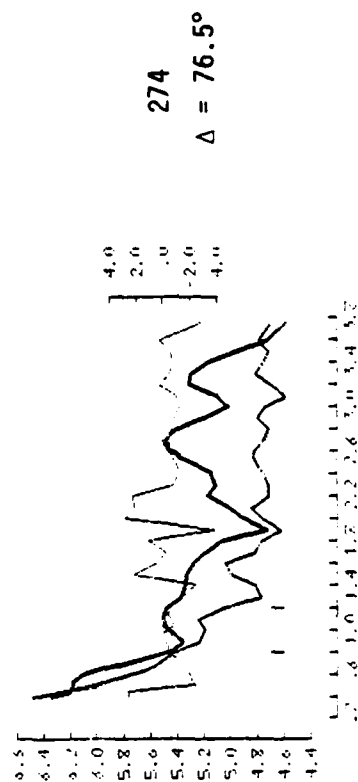
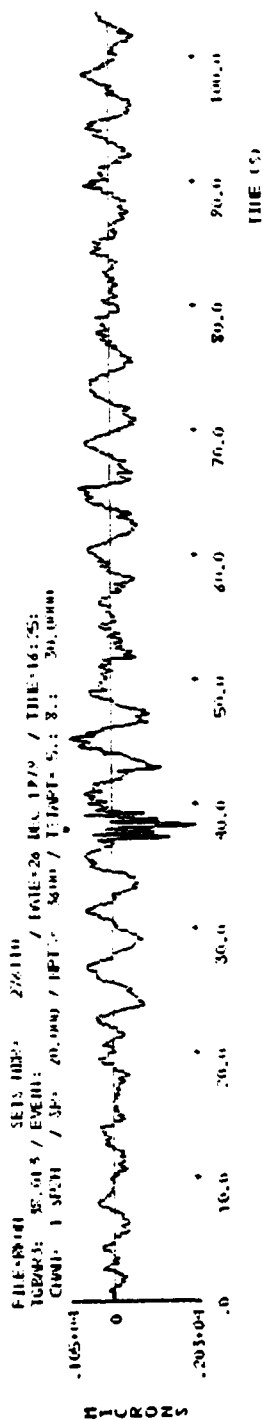


Figure 6.8. (continued).



REF: R040  
 180- 6.414 [REDACTED] 0.25 [REDACTED] 5.593 [REDACTED] 2.02 [REDACTED] 3.750  
 1100- 3000 [REDACTED] 1.000 [REDACTED] 1.200

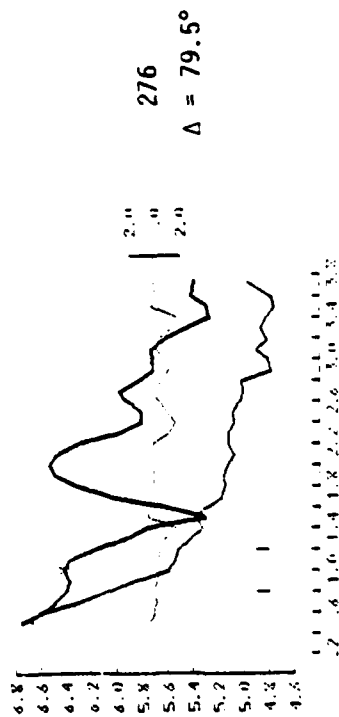
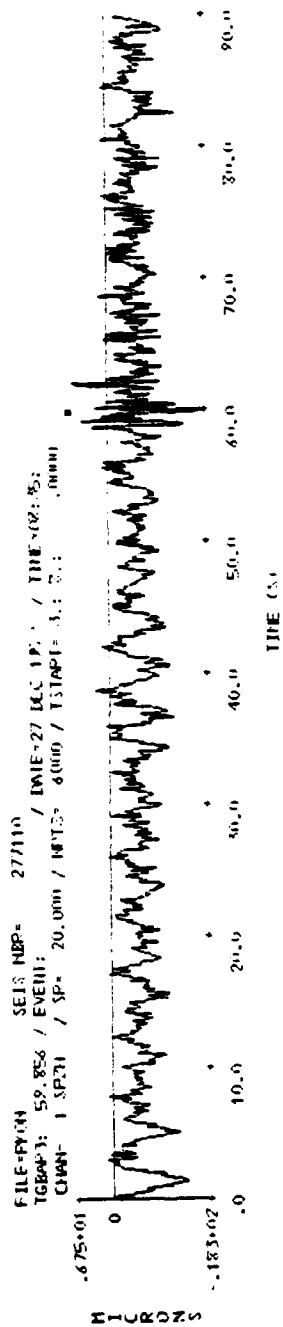


Figure 6.8. (continued).



NET FLOI  
 HB= 4.326 DB= .046 IIR= .065 IIRF= 3.323 SYN= .901 DEL= 3.740  
 FLEF= .800 LC= 1.000 FPIGH= 1.200

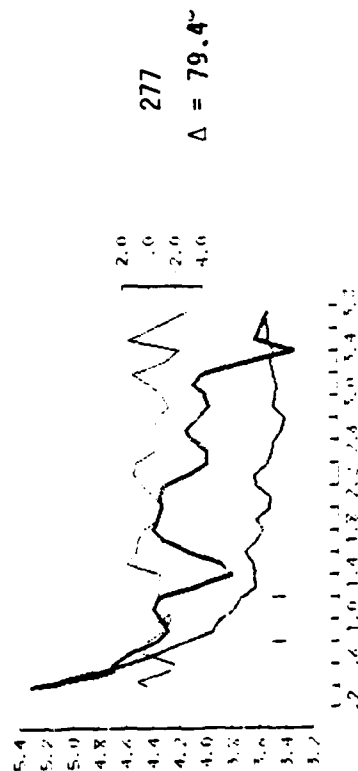
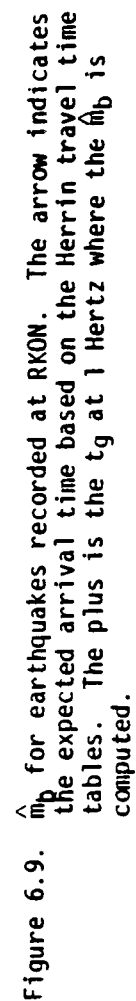
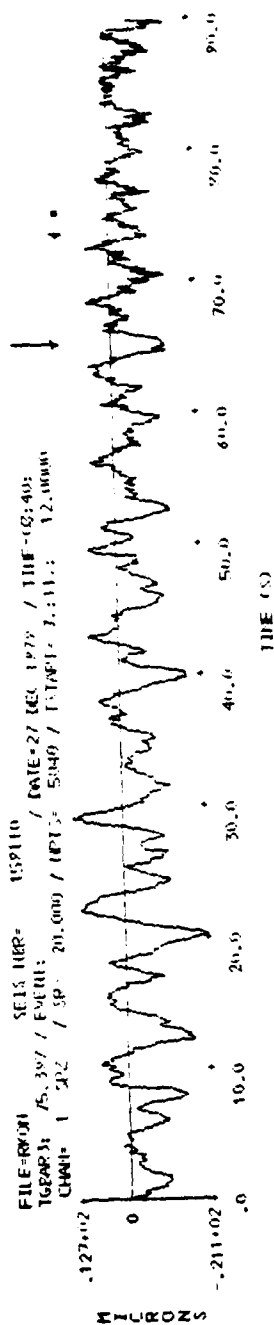


Figure 6.8. (continued).





IBF FLOT  
 MS= 4.312 MB= .074 MB= .105 MB= 4.100 5/10:    .3\*01 MB= 4.110  
 FLEET= .200 FC= 1.000 FPGAT= 1.200

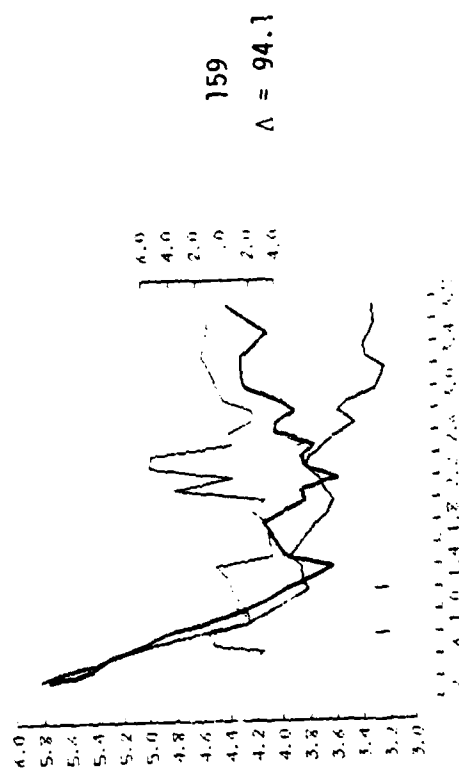


Figure 6.9. (continued).



In Table 6.2 we summarize the  $\hat{m}_b$  data. We also list the signal/noise at 1 Hertz and the statistical uncertainty in  $\hat{m}_b$ . The PDE  $m_b$  is listed, when available. Finally, we include the  $\hat{m}_b$  of the noise.

The noise  $\hat{m}_b$  is useful for flagging events for which the calibration appears to be incorrect. Events 274 and 276 are in this category. Note that the 1 Hertz noise level is more than an order of magnitude larger than it is for the other RKON recordings. Also, for 276 the  $\hat{m}_b$  is 1.3 units larger than the PDE  $m_b$ . For most of the other events the  $\hat{m}_b$  and PDE  $m_b$  are in fairly good agreement. The main exception is 277, and the calibration may also be in error for this one.

#### 6.5 THE $\hat{M}_s$ ALGORITHM

The  $\hat{m}_b$  algorithm is a natural extension of the MARS processing which leads to an estimate for the spectral amplitude of a particular signal in a window that is narrow in both time and frequency. As explained in Section 6.2, the "MARS spectrum" is constructed by selecting an envelope peak for each center frequency. The selection is done by finding the peaks that satisfy a pre-selected pattern. For  $\hat{m}_b$  the pattern includes the requirement that the peaks have (approximately) the same group arrival time ( $t_g$ ). To apply the same algorithm to dispersed surface waves, it is again necessary to specify the pattern of the signal of interest in a display like that in Figure 6.1. In effect, the program must be given some estimate for the group velocity dispersion of the signal of interest.

If the  $t_g$  for all envelope peaks are corrected to account for a specified dispersion, the MARS detection algorithm can be used just the same as it is for body waves. A corrected display of envelope peaks like that in Figure 6.1 can be searched for an "undispersed" arrival, which will be an arrival which has dispersion close to that specified. Once the arrival is detected,  $\hat{M}_s$  can be computed in an entirely analogous fashion to  $\hat{m}_b$ .

TABLE 6.2

SUMMARY OF  $\hat{m}_b$  FOR ACTUAL EVENT RECORDINGS

Event	Range	S/N (1 Hz)	$\hat{m}_b$	$\hat{m}_b$ Uncertainty	PDE $m_b$	Noise $\hat{m}_b$
Presumed Explosions at RKON						
20	79.3	92	5.827	0.002	5.9	3.86
21	71.0	7	5.114	0.016	4.8	4.25
22	76.4	6	4.780	0.025	5.1	4.03
33	53.8	3	4.622	0.051	5.0	4.16
81	79.4	58	5.831	0.003	6.0	4.07
274	76.5	2	5.466	0.112	not reported	5.18
276	79.5	7	6.414	0.027	5.1	5.59
277	79.4	3	4.326	0.051	5.0	3.88
Presumed Earthquakes at RKON						
151	93.6	3.4	4.922	0.061	5.0	4.39
159	94.1	1.6	4.312	0.105	not reported	4.10
Presumed Earthquake at LASA						
47	61.1	20	5.116	0.009	4.9	3.81

In essence, the  $\hat{M}_s$  algorithm is the same as the  $\hat{m}_b$  algorithm, except that we must first map the  $t_g$ - $f$  plane into a new plane in which signals with a prespecified dispersion will appear to be nearly undispersed. Masso, et al. (1979), Appendix C, discuss this mapping and suggest two ways to implement it. The first is to select some reference frequency ( $f_R$ ) and compute

$$\delta t_g(f) = t_g^*(f) - t_g^*(f_R) \quad , \quad (6.1)$$

where the  $t_g^*$  are the group arrival times for the prespecified dispersion. The  $t_g$ - $f$  plane is then mapped into a  $t_g'$ - $f$  plane with

$$t_g'(f) = t_g(f) - \delta t_g(f) \quad . \quad (6.2)$$

The second method suggested by Masso, et al. (1979) is to cross-correlate the signal with a reference signal and then to process the cross-correlation time series. Such a "matched filtering" operation to improve the ability to estimate surface wave spectra is a well-known technique which is incorporated in the COLLAPSE program at Teledyne Geotech (Alexander and Lambert, 1971).

In most cases only the phase of the reference signal can be specified with any confidence, so the cross-correlation reduces to a multiplication by,  $\exp[-i\phi]$ , where  $\phi$  is the phase of the reference signal.

In practice,

$$\phi = -2\pi f \delta t_g(f) \quad (6.3)$$

and the two methods only differ because the order of operations is interchanged. That is, in the first method the signal is first narrow-band filtered, then the "matched filter" provided by the dispersion of the reference signal is applied. In the cross-correlation method the "matched filtering" is applied before narrow-band filtering.

Once the  $t_g$ - $f$  plane has been mapped to a  $t_g'$ - $f$  plane, the detection algorithm described in Section 6.2 can be applied to define the "MARS spectrum" of a detected signal. The  $\hat{M}_S$  is then computed from the smoothed, noise-corrected spectral amplitude at a particular period. An initial choice which is consistent with current practices for obtaining a time domain  $M_S$  is 20 seconds, though other periods may turn out to be better when large amounts of data are processed.

While the procedure outlined appears to be a straightforward extension of the  $\hat{m}_b$  procedure, there are several important parameters that can only be firmly set after developing some experience with actual data. For example, the choice of  $Q$ , which controls the width of the narrow-band filter, involves a tradeoff between the desire for good time resolution (for detection) and good spectral amplitude resolution. The width of the "acceptance window" in the  $t_g$ - $f$  plane (Figure 6.1) is controlled to some degree by an arbitrary parameter called  $\alpha$  (Savino, et al., 1980). Small  $\alpha$  impose the requirement that the signal dispersion closely match that of the reference signal, while large  $\alpha$  increase the possibility that the wrong spectral amplitudes will be associated with the signal.

Finally, we point out that for  $\hat{M}_S$  we only need to detect the signal in a narrow period band, initially chosen to be 18 to 22 seconds. Thus, large differences between the signal dispersion and reference dispersion outside this band only matter to the extent that they make the signal hard to detect.

How do we propose to specify the reference signal dispersion? For large signal/noise surface wave arrivals, it doesn't make much difference, the correct spectral amplitudes are easily identified. The problem is with small signals. The reference dispersion must come from theoretical models or, empirically, from larger events in the same source region as the event of interest.

## 6.6 $\hat{M}_S$ TEST CALCULATIONS

To test the  $\hat{M}_S$  calculation and optimize the selection of  $Q$  and  $\alpha$ , we followed much the same procedure described in Section 6.3

for  $\hat{m}_b$ . That is, a synthetic seismogram was added to various levels of actual seismic noise. In this case the noise was taken from a long period LASA recording in the AI data set. Typical results are shown in Figure 6.11. For these examples, connection with equations (6.1 to 6.2) of the previous section was used to map the  $t_g$ -f plane to a  $t_g'$ -f plane. The reference signal dispersion was the dispersion used to compute the synthetic itself.

In Figure 6.11 we first show the  $\hat{M}_s$  calculation for a signal that is essentially just the synthetic. The noise section is included, but with the peak noise amplitude scaled to be 1 percent of the peak signal amplitude (peak S/N = 100). Since we are subtracting the right dispersion for this signal, the  $t_g$  is close to zero over the entire frequency band. The deviation from zero is due to the inability of MARS to precisely identify the group arrival time of a particular frequency component and some errors in the "exact" group arrival times due to interpolation.

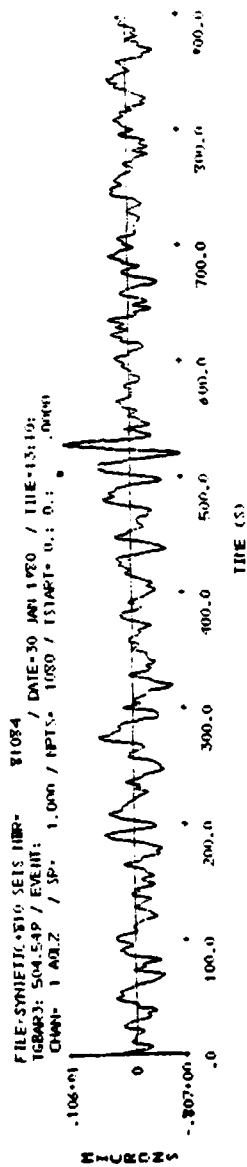
The other two examples in Figure 6.11 have Peak S/N = 1 and have been added at different times in the noise section. The data from these three examples are listed in Table 6.3. The arrival time error is based on the  $t_g$  at 20 seconds, which is listed with each example.

The examples in Figure 6.11 show that the signal is accurately detected and the  $\hat{M}_s$  values accurately represent the signal amplitude. Note that the  $\hat{M}_s$  values for cases B and C are nearly the same, while the peak time domain amplitudes are much different.

Many cases like those in Figure 6.11 were run with peak S/N = 1 and 2. The best results were obtained with  $Q = 250 f$ , as it is for the examples in Figure 6.11, and  $Q = 125f$ . More testing needs to be done to choose between these values.

Tests were run with the cross-correlation method, as in Equation 6.3, as well as with the direct mapping of the  $t_g$ -f plane. Similar results were obtained, as expected.





PBS PLOT  
 NS= 2.280 DMS= .658 DMS= .067 HREF= 1.757 S/N= .9+01 PREL= 2.370  
 LEFT=18.000 TC=20.000 RIGHT=22.000

tg (20 sec) = 501.9

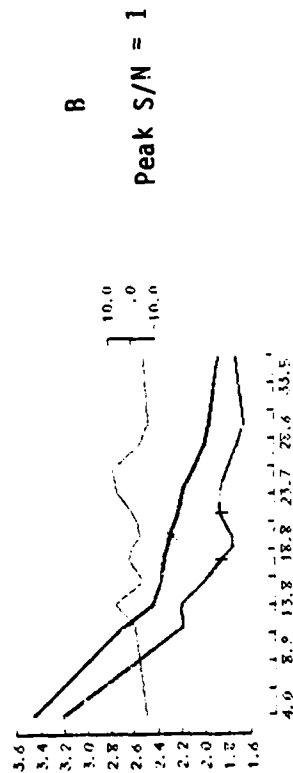
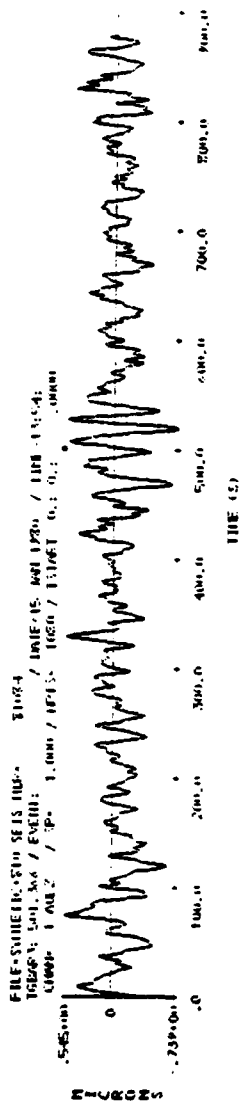


Figure 6.11. (continued)



RMS: 1.01  
 RMS: 2.224 RMS: 1.058 RMS: 1.058 RMS: 1.058 RMS: 1.058  
 REF: 12.000 1.0 20.000 10.000 22.000

tg (20 sec) = 507.6

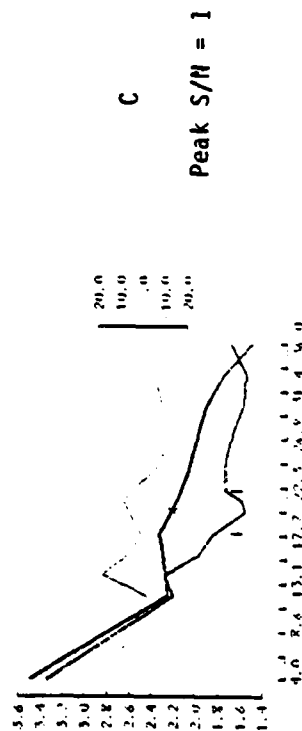


Figure 6.11 (continued)

TABLE 6.3  
SUMMARY OF  $\hat{M}_s$  TEST CALCULATIONS

<u>Identifier</u>	<u>Peak Signal</u> <u>Peak Noise</u>	<u>S/N</u> <u>(20 sec)</u>	<u><math>\hat{M}_s</math></u>	<u><math>\hat{M}_s</math></u> <u>Uncertainty</u>	<u><math>\hat{M}_s</math></u> <u>Error</u>	<u>Arrival</u> <u>Time</u> <u>Error</u> <u>(sec)</u>
A	100	168	2.169	0.001	--	--
B	1	3.3	2.280	.067	.111	-1.9
C	1	4.4	2.224	.068	.055	3.8

## 6.7 CONCLUSIONS

The  $\hat{m}_b$  algorithm is essentially ready for application to a large data base. Some minor tinkering with the algorithm, as mentioned at the end of Section 6.2, might improve the performance slightly.

The  $\hat{m}_b$  data will not be compatible with standard  $m_b$  data. For example, Bache (1979) showed that the  $\hat{m}_b$ -yield curves have different slope than  $m_b$ -yield curves. The advantage of using  $\hat{m}_b$  is that it is more consistent and convenient for digital data. However, the full advantage of the technique requires that an entire data base be processed.

The  $\hat{M}_s$  algorithm is at an earlier stage of development, in part because we do not have the large base of experience which the VSC discrimination experiment provided for short period body waves. However, our tests so far are promising and the  $\hat{M}_s$  algorithm is clearly ready for application to a real data set.

The  $\hat{M}_s$  will never be as automatic as  $\hat{m}_b$  because of the requirement to estimate the expected dispersion characteristics of the signal. Of course, most of this could be automated as part of a larger signal analysis system.

THIS PAGE LEFT BLANK

## REFERENCES

- Alexander, S. S. and J. W. Lambert (1971), "Single Station and Array Methods for Improved Surface Wave Spectral Estimates," Teledyne Geotech Seismic Data Laboratory Report NO. 264 submitted to ARPA/AFTAC, December.
- Bache, T. C. (1978), "A Detailed Listing of the Data and Results for the Unclassified Report: Source Amplitudes of NTS Explosions Inferred from Rayleigh Waves at Albuquerque and Tucson," Systems, Science and Software Topical Report SSS-CR-78-3745 submitted to AFTAC/VSC, August, 17 pages.
- Bache, T. C. (1979), " $m_b$ , a Spectral Body Wave Magnitude (U)," Systems, Science and Software Report SSS-CR-79-3901 submitted to AFTAC/VSC, January, 99 pages.
- Bache, T. C., J. T. Cherry, N. Rimer, J. M. Savino, T. R. Blake, T. G. Barker and D. G. Lambert (1975), "An Explanation of the Relative Amplitudes Generated by Explosions in Different Test Areas at NTS," Systems, Science and Software Final Report to the Defense Nuclear Agency, DNA 3958F, October.
- Bache, T. C., P. L. Goupillaud and B. F. Mason (1977), "Seismic Studies for Improved Yield Determination," Systems, Science and Software Quarterly Technical Report SSS-R-77-3345 submitted to AFTAC/VSC, July, 65 pages.
- Bache, T. C., W. L. Rodi and B. F. Mason (1978), "Source Amplitudes of NTS Explosions Inferred from Rayleigh Waves at Albuquerque and Tucson," Systems, Science and Software Report SSS-R-78-3690 submitted to ARPA/VSC, June, 91 pages.
- Bache, T. C., W. L. Rodi and D. G. Harkrider (1978), "Crustal Structures Inferred from Rayleigh-Wave Signatures of NTS Explosions," Bull. Seism. Soc. Amer., 68, pp. 1399-1413.
- Bache, T. C., S. M. Day and J. M. Savino (1979), "Automated Magnitude Measures, Earthquake Source Modeling, VFM Discriminant Testing and Summary of Current Research," Systems, Science and Software Quarterly Technical Report SSS-R-79-3933 submitted to AFTAC/VSC, February, 98 pages.
- Bache, T. C., W. E. Farrell and D. G. Lambert (1979), "Block Motion Estimates from Seismological Observations of MIGHTY EPIC and DIABLO HAWK," Defense Nuclear Agency report, DNA 5007F, July, 176 pages.

- Bache, T. C., T. G. Barker, N. Rimer and J. T. Cherry (1980), "The Contribution of Two-Dimensional Source Effects to the Far-Field Seismic Signatures of Underground Nuclear Explosions," Systems, Science and Software Technical Report SSS-R-80-4569 submitted to ARPA/VSC, 200 pages.
- Eisenhauer, T. D. (1976), " $M_s$  and  $m_b$  Estimates for USSR Underground Explosions," unpublished report.
- Hadley, D. M. and R. S. Hart (1979), "Seismic Studies of the Nevada Test Site," Sierra Geophysics Quarterly Technical Report SGI-R-79-003, submitted to VSC/ARPA, June, 44 pages.
- Jordan, J. N., W. V. Mickey, W. Helterbran and D. M. Clark (1966), "Travel Times and Amplitudes from the SALMON Explosion," Journal of Geophysical Research, 71, No. 14, p. 3469.
- Masso, J. F. C. B. Archambeau and J. M. Savino (1979), "Implementation, Testing and Specification of a Seismic Event Detection and Discrimination System," Systems, Science and Software Final Report SSS-R-79-3963 submitted to ACDA, March, 110 pages.
- McGarr, A (1969), "Amplitude Variations of Rayleigh Waves -- Propagation Across a Continental Margin," Bull. Seism. Soc. Amer., 59, pp. 1281-1305.
- Mendiguren, J. A. (1977), "Inversion of Surface Wave Data in Source Mechanism Studies," JGR, 82, pp. 889-894.
- Mitchell, B. J. (1975), "Regional Rayleigh Wave Attenuation in North America," JGR, 80, pp. 4904-4916.
- Mueller, R. A. and J. R. Murphy (1971), "Seismic Characteristics of Underground Nuclear Detonations," Bull. Seism. Soc. Amer., 61, pp. 1975.
- Murphy, J. R. (1969), "Discussion of Paper by D. Springer, M. Denny, J. Healy and W. Mickey, 'The Sterling Experiment: Decoupling of Seismic Waves by a Shot-Generated Cavity'," Journal of Geophysical Research, 74, No. 20, p. 6714.
- Murphy, J. R. (1977), "Seismic Source Functions and Magnitude Determinations for Underground Nuclear Detonations," Bull. Seism. Soc. Amer., 67, No. 1, p. 135.
- Rimer, N., J. T. Cherry, S. M. Day, T. C. Bache, J. R. Murphy and A. Maewal (1979), "Two-Dimensional Calculation of PILEDRIVER, Analytic Continuation of Finite Difference Source Calculations, Analysis of Free-Field Data from MERLIN and Summary of Current Research," Systems, Science and Software Report SSS-R-79-4121 submitted to AFTAC/VSC, August, 158 pages.

- Rivers, W. and D. H. von Seggern (1979), "Effect of Tectonic Strain Release on Surface-Wave Magnitudes," to be published as Teledyne Geotech Technical Report SDAC-TR-79-6.
- Salvado, C. and J. B. Minster (1979), "Slipping Interfaces: A Possible Source of S Radiation from Explosive Sources," submitted to Bull. Seism. Soc. Amer. for publication.
- Savino, J. M. C. B. Archambeau and J. F. Masso (1980), "Discrimination Results from the Priority 2 Stations," Systems, Science and Software Technical Report SSS-R-80-4566 submitted to AFTAC/VSC, July, 130 pages.
- Sobel, P. A. (1978), "The Effects of Spall on  $m_b$  and  $M_s$ ," Teledyne Geotech Report SDAC-TR-77-12 submitted to AFTAC/VSC, April, 54 pages.
- Stevens, J. L. (1980), "Seismic Radiation from the Sudden Creation of a Spherical Cavity in an Arbitrarily Prestressed Elastic Medium," Geophys. J., 61, pp. 303-328.
- Toksöz, M. N. and H. H. Kehrner (1972), "Tectonic Strain Release by Underground Nuclear Explosions and Its Effect on Seismic Discrimination," Geophys. J. R. Astr. Soc., 31, pp. 141-161.
- Viecelli, J. A. (1973), "Spallation and the Generation of Surface Waves by an Underground Explosion," J. Geophys. Res., 78, pp. 2475-2487.